FINITE ELEMENT METHOD (FEM) MODELING OF HOPPER FLOW

by

Kunal Sanjay Pardikar

A Dissertation

Submitted to the Faculty of Purdue University

In Partial Fulfillment of the Requirements for the degree of

Doctor of Philosophy

School of Mechanical Engineering

West Lafayette, Indiana

May 2020

THE PURDUE UNIVERSITY GRADUATE SCHOOL
STATEMENT OF COMMITTEE APPROVAL

Dr. Carl Wassgren, Chair
School of Mechanical Engineering

Dr. Marcial Gonzalez
School of Mechanical Engineering

Dr. Ivan Christov
School of Mechanical Engineering

Dr. Kingsly Ambrose
Agricultural and Biological Engineering

Approved by:
Dr. Nicole Key

Dedicated to my parents Sanjay and Maya Pardikar, and to my sister Kalyani Pardikar for their unwavering love and support throughout my life.

ACKNOWLEDGMENTS

I am extremely grateful to my adviser Prof. Carl Wassgren for his immense patience, guidance, and mentorship during this PhD. I have learnt a lot from you about research, technical writing, presenting, and general life skills. I appreciate the multiple opportunities you provided of participating in various conferences and competitions. I extend my gratitude to Prof. Gonzalez, Prof. Ambrose, and Prof. Christov for your guidance at different stages of this PhD and appreciate your service as the examining committee.

I would like to acknowledge Dr. Tyler Westover and other members at the Idaho National Laboratory (INL) for giving me the opportunity to spend two summer sessions at INL. I enjoyed working at INL on the interesting topic of modeling behavior of compressible biomass materials. I would also like to acknowledge the financial support received from INL and Genentech Inc. during different stages of my PhD.

I would like to thank the school of mechanical engineering for giving me the opportunity to gain teaching experience through TA assignments. The TA experience was vital in refining my teamwork and communication skills.

I would like to acknowledge Dr. Madhusudan Kodam of Corteva Agriscience for his constant encouragement and guidance. I am grateful to my senior and present labmates: Shrikant, Liza, Rohit, Yu, Harsh, Siddharth, Shayan, Zhengpu, Abhishek, and Nathan for your support and numerous productive discussions. I have learnt a lot of necessary technical skills from you. I especially appreciate the help provided by Shayan in completing the necessary experiments in time.

I owe my sincere gratitude to my apartment mates, Kumar and Prateek for motivating me and making the last few years memorable. This thesis would not have been possible without the help of my friends and family members.

TABLE OF CONTENTS

LIST OF TABLES

LIST OF FIGURES

LIST OF SYMBOLS

W	Width of the wedge-shaped hopper, m
C	Coefficient of Beverloo's correlation
T	Time, s
Q	Volumetric flow, m^3
$\boldsymbol{M}$	Nodal mass matrix in FEM, kg
$\boldsymbol{F}$	Force vector, N
$\boldsymbol{I}$	Internal force vector, N
D	Diffusion length in kinematic model, m
$\boldsymbol{D}$	Elasticity tangent matrix
E	Young's modulus of elasticity, Pa
H	Height from hopper outlet, m
G	Plastic potential surface
f_c	Unconfined yield strength (UYS), Pa
$\boldsymbol{\sigma}$	Stress tensor, Pa
m	Mass, kg
$\boldsymbol{u}$	Displacement vector, m
v	Vertical component of velocity, m/s
r	Radial distance from hopper apex point, m
R	Radial distance of material free surface from hopper apex point, m
δ	Effective angle of internal friction, Deg
$\boldsymbol{\varepsilon}$	Strain tensor
$\bar{\gamma}$	Equivalent shear strain
x	x coordinate, m
ν	Poisson's ratio
τ	Shear stress, Pa
ϕ	Internal friction angle, Deg
c	Cohesion, Pa
q	Mises equivalent stress, Pa
p	Hydrostatic pressure, Pa
ψ	Dilation angle, Deg
Θ	Third invariant of deviatoric stress tensor
λ	Plastic multiplier
β	Internal friction angle in $q-p$ plane
d	Cohesion in $q-p$ plane
$d_{particle}$	Mean particle diameter, m
η	Solid fraction

s	Penalty stiffness, kg/s^2
k	Flow function slope
ρ	Density, kg/m^3
θ	Hopper wall inclination from vertical line, Deg
b	Hopper outlet width, m

Superscripts

$\cdot$	First time derivative
$\cdot\cdot$	Second time derivative
$-$	Equivalent of that quantity
elastic	Elastic part
plastic	Plastic part

Subscripts

0	Value at zero consolidation stress
1	Major principal component
2	Intermediate principal component
3	Minor principal component
SS	Steady state
mod	Modified quantity
MC	Mohr-Coulomb model
DPC	Drucker-Prager Cap model
i	Initial state
cv	Constant Volume state
w	Wall
vol	Volumetric
b	Bulk
centerline	Value at hopper centerline

ABBREVIATIONS

FEM	Finite Element Method
PIV	Particle Image Velocimetry
DEM	Discrete Element Method
HPC	High Performance Computing
GPU	Graphical Processing Unit
FDM	Finite Difference Method
BEM	Boundary Element Method
MDR	Mass Discharge Rate
COW	Critical Outlet Width

ABSTRACT

Hopper systems of different shapes and sizes are widely used in bulk solids industries to store and further process the particulate material. Poor hopper design causes variety of problems and results in wastage of resources. This dissertation investigates the applicability of finite element method (FEM) based continuum modeling in predicting flow characteristics of particulate materials discharging through hopper system. Throughout the years, FEM has been implemented to simulate the shear failure of particulate materials such as sand, glass beads, and pharmaceutical powders. The FEM framework is based on the underlying constitutive model. Different constitutive models are available in the literature to govern the behavior of particulate materials. These models differ in their complexity, ease of implementation, and have specific strengths and limitations. This work thoroughly investigates the elasto-plastic constitutive models available in the commercial software Abaqus in the context of hopper flow of particulate materials.

The thesis consists of three major parts, first part deals with FEM modeling of cohesionless particulate materials and corresponding verification of the hopper flow characteristics through comparison to analytical theories and empirical correlations. The second part presents quantitative comparison of FEM predicted flow characteristics to experimental results for Ottawa sand discharging through concentric and eccentric bins. Particle image velocimetry (PIV) experiments are conducted on a laboratory-scale bin to quantify different flow characteristics. The last part deals with cohesive particulate materials and presents a novel FEM approach for predicting the critical hopper outlet opening to ensure uninterrupted discharge of the stored material.

This thesis concludes that the FEM modeling based on simple elasto-plastic constitutive model proves useful in predicting different hopper flow characteristics of particulate materials. The accuracy of FEM modeling depends on detailed material characterization and corresponding implementation in Abaqus. Some modifications need to be made in the elasto-plastic constitutive models to accurately represent the bulk material behavior. The ideas presented in this thesis can be applied to FEM modeling of other processing equipment such as the rotating drum, screw-feeder, rotating blender/mixer etc.

1. INTRODUCTION

1.1 Hoppers

Particulate material is one of the most common raw materials used in all industries. Almost 75% of all raw material feedstock used in processing industries such as pharmaceutical, agricultural, chemical, food, building material, biotechnology, metallurgy is in the form of particulate material [1]. These industries use hoppers of different shapes and sizes in processing cycles to store and gravitationally transfer the raw particulate material.

Hoppers are also known as silos or bins or bunkers. Hopper flow of particulate materials has been a topic of research for many years. Jenike's [2] seminal work in 1961 laid the foundation of this topic. In his work, Jenike developed some guidelines to avoid poor and inefficient design of hopper systems. The performance of hoppers can have a major impact on product quality and efficient use of resources. In most cases, uniform mass flow rate of the discharging particulate material is desired. But hoppers often experience common problems, such as plugging, arching, ratholing, and flooding, which can cause uneven flow of discharging particulate material [3]. Poorly designed hoppers often collapse due to excessive wall stresses. These problems ultimately results in prolonged plant start-up times [4], increased maintenance costs, and extra labor. Even after start-up, approximately 40% of the capacity of these plants is wasted [1]. Such unreliable behavior can be avoided through the use of predictive models, which can also help in designing a robust hopper, therefore, increasing efficiency and economic viability of the plant.

1.2 Types of Predictive Models

At a broad level, there are four types of predictive hopper flow models available in the literature. Discrete Element Method (DEM) modeling, continuum analytical theories, empirical correlations, and continuum computational models. This section provides an overview of the definitions, advantages, and disadvantages of these predictive methods. The continuum analytical theories and empirical correlations are available for conical as well as wedge-shaped hoppers. In this thesis, the focus is on wedge-shaped hopper with rectangular outlet.

1.2.1 Discrete Element Method (DEM) Modeling

In DEM, material is represented by an assembly of particles. According to the original definition by Cundall and Strack [5], DEM is a method that allows finite displacement and rotation of discrete bodies, particles can detach completely, and subsequent contacts are automatically recognized. As each particle is simulated separately, DEM is capable of observing particle-level phenomena. DEM has been applied by several researchers for different systems such as hopper discharge, rotating drums [6], tumbling mills [7], and rock failure [8], albeit on small scale.

There are various particle contact models which differ in terms of the logic used for detection and revision of contacts, methods used to solve the governing equations (explicit or implicit) [9]. Most commercially available DEM software use an explicit time integration scheme with a small time step.

This small time step imposes a limitation on the number of particles that can be simulated in a reasonable time. Additionally, it is difficult to model particles with complex shapes [7]. Most often, these complex particles are represented using simplified models such as the multisphere model [10], which gives a poor representation of real particles. Complex shapes also increase the computational costs by two to three times, and in some cases even by 10 times [6,7]. Parallelization using high performance clusters (HPCs) and graphical processing units (GPUs) is often used to make these simulations faster. It would take a long time for DEM to be able to simulate same number of particles as in a real industrial system.

Since DEM deals with individual particles, only micro-level properties can be specified; bulk material behavior depends on these micro-level properties. Particle contact models need accurate input parameters to be used as a reliable predictive tool. These input parameters include particle and contact properties such as density, Young's modulus, coefficients of static and rolling friction, coefficient of restitution. A major hurdle in implementing DEM is the time it takes to obtain these input parameters. Hitherto, there is no standardized procedure to obtain these parameters. Therefore, sometimes parameters are assumed without proper justification [11] and results are rarely validated against experiments [12], which means simulation results are typically used to predict qualitative behavior.

Clearly DEM has significant limitations for modeling particulate systems of industrial significance. Although these limitations might be overcome in near future with the development

of computational infrastructure, DEM is just not capable of accurately simulating large number of small-scale particles with complex shapes at this point in time.

Most of the time, industrial engineers are more interested in macroscopic behavior of bulk material rather than what is happening at the particle-level, since the bulk material behavior will have a major impact on final product quality and plant efficiency. Such bulk material behavior can be modeled through continuum analytical or computational models. Continuum models use bulk material properties as input parameters, which are easier to measure using standardized experiments as compared to measuring particle-level properties required for DEM analysis.

1.2.2 Continuum Analytical Theories

In early years, many researchers [13–16] focused on deriving approximate analytical expressions for hopper wall stresses, velocity profiles, and mass discharge rate. A number of steady state continuum theories based on the assumption of an incompressible bulk material (constant bulk density, ρ_b) are available for hopper flow [16]. These theories use bulk material properties, wall friction, and hopper geometry as input parameters. Analytical expressions are derived by starting from a force balance analysis on a differential element to form a governing equation that is integrated throughout the hopper based on certain boundary conditions. Some simplifying assumptions need to be made to facilitate integration of the governing equation.

The assumptions, shape of the differential element, boundary conditions, and consideration of dynamic equilibrium varies with each theory. For detailed information on the theories and derivation of final analytical equations please refer to Jenike [2], Nedderman [16], Schulze [3], and Enstad [15]. Table 1.1 compares different theories, underlying assumptions, and results that can be obtained.

Table 1.1. Comparison of steady state continuum theories

Continuum theory	**Assumptions**	**Results obtained**
Jenike [2]	– Mean principal stress is proportional to radial distance from hopper apex.	– Discharging stresses near outlet.
Walker [14]	– Principal stresses act in vertical and horizontal directions. – Uniform stresses along horizontal cross-section at a given height. – Material velocity is inversely proportional to height from hopper apex.	– Filling and discharging stresses and velocity distribution through hopper. – Mass discharge rate.
Hour-glass [16]	– Principal stresses act along radial (r) and circumferential directions (θ) with respect to cylindrical coordinate system placed at hopper apex. – Uniform stresses along radial cross-section at a given radius. – Material velocity is inversely proportional to radius from hopper apex.	
Enstad [15]	– Uniform principal stresses act on a radial surface with specified radius R ≠ r. – Velocity is inversely proportional to R.	

All of these analytical theories assume that the particulate material deforms plastically while flowing through the hopper. Under significant loading, the elasto-plastic particulate material yields and undergoes irreversible plastic deformation as shown in Figure 1.1.

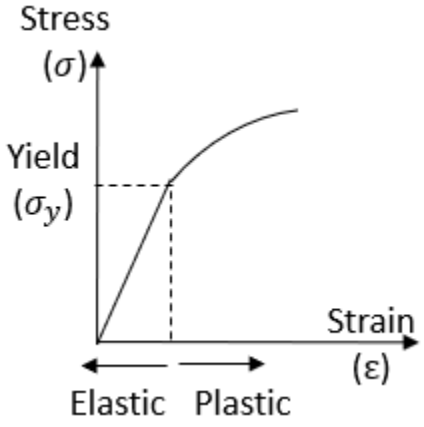

Figure 1.1. Elasto-plastic material under loading.

This plastic deformation occurs when the stresses inside the material meet a yielding criterion. This criterion is known as the yield surface. It is well known that the particulate material fails when shear stresses on any internal plane reach a critical value. The Mohr-Coulomb [17] yield surface is the simplest criterion to determine these critical stress states,

$$\sigma = \tau \tan \phi + c, \tag{1.1}$$

Where, τ is the shear stress, σ is the normal stress, ϕ is the internal friction angle of the bulk material, and c is the cohesion. The Mohr-Coulomb yield surface simply states that if the shear stress on a plane exceeds the normal stress multiplied by a friction coefficient plus some inherent cohesion, the material will yield. This criterion is based on the concept of frictional force acting on the contact surface between two bodies (Figure 1.2a). Whereas, cohesion may be viewed as a minimum shear stress required to move the surfaces relative to each other (Figure 1.2b). Particulate materials consisting dry particles without any interparticle attractive forces, have zero cohesion ($c = 0$), these materials are known as cohesionless particulate materials. Dry sand, collection of dry glass beads are examples of cohesionless materials. Due to interparticle attractive forces resulting from mechanisms like liquid bridging and electrostatic charge, particulate materials can have non-zero cohesion, these are known as the cohesive particulate materials.

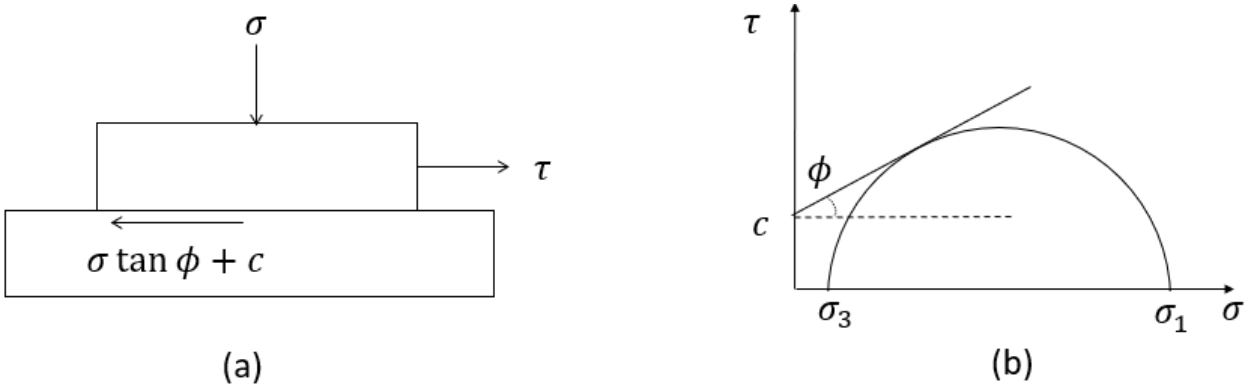

Figure 1.2. (a) Two bodies in frictional contact (b) Mohr-Coulomb yield surface.

Researchers have further modified the theories mentioned in Table 1.1 to make the assumptions more realistic. For example, Walker's theory has been modified by Walters to include a stress distribution factor [18]. While in some cases the velocity profiles and wall stresses predicted by such analytical expressions match well with experimental results, analytical mass discharge rate is significantly over-predicted [16].

Apart from theories based on the Mohr-Coulomb plasticity criterion, expression for velocity profiles can also be obtained from kinematic model. The kinematic model is based on a type of diffusion equation,

$$\frac{\partial \mathrm{v}}{\partial y} = -D\,\frac{\partial^2 \mathrm{v}}{\partial x^2}. \tag{1.2}$$

Here, v is the vertical velocity component, y is the vertical co-ordinate, x is the distance from hopper centerline, and D is the constant of proportionality known as the 'diffusion length'. For which a similarity solution exists [19] in terms of the centerline velocity $\mathrm{v}_{centerline}$ at that height $y = h$,

$$\mathrm{v}(x, y) = \mathrm{v}_{\mathrm{centerline}}(y = h)e^{-x^2/4Dy}. \tag{1.3}$$

The velocity profile given by the kinematic model has been shown to work well for qualitative representation of the experimental velocity profile [19,20].

1.2.3 Empirical Correlations

There are multiple empirical correlations available for predicting the mass discharge rate of cohesionless particulate materials. Beverloo [21] came up with fist such correlation to predict the mass discharge rate through flat bottomed hoppers,

$$\dot{m}_{Beverloo} = \frac{4C}{\pi}\rho_i A^* \sqrt{g D_H^*}, \tag{1.4}$$

Here, A^* is the modified hopper outlet area,

$$A^* = (b - kd_{particle})(l - kd_{particle}), \tag{1.5}$$

Where, b and l is the width and length of the rectangular outlet respectively. Constant k has value of 1.5 for spherical particles [16]. And the modified hydraulic diameter D_H^* is determined as,

$$D_H^* = \frac{2(b - k\,d_{particle})(l - kd_{particle})}{(b + l - 2k\,d_{particle})}, \tag{1.6}$$

This correlation was later modified by Rose and Tanaka [22] for converging hoppers and has a dependence on the hopper half angle (θ),

$$\dot{m}_{Rose\ Tanaka} = \dot{m}_{Beverloo}(\tan\theta)^{-0.35}. \tag{1.7}$$

These mass discharge rate correlations have been further modified based on new experiments or computational simulations. Although, these correlations accurately depict the

dependence of mass discharge rate on hopper outlet opening, some adjustments need to be made in the coefficients to obtain a quantitative agreement with experimental data.

Similarly, McLean's [23] empirical correlation is available for the minimum hopper outlet width required to ensure uninterrupted discharge of cohesive particulate materials,

$$B_{critical} = f_c(1 + 0.005\theta)/\rho g, \tag{1.8}$$

Where, θ is the hopper half angle in degrees. This correlation has been shown to be overconservative by multiple experiments [24]. It should be noted that above mentioned correlations are for wedge-shaped hoppers as the focus of this thesis is predominantly on wedge-shaped hoppers.

1.2.4 Continuum Computational Models

With the development of computational infrastructure, continuum computational modeling became popular, which employed computational methods such as non-linear FEM (finite element method), FDM (finite difference method) and BEM (boundary element method). The simplifying assumptions necessary for deriving analytical expressions are not needed in computational modeling. Although, choosing a good computational model for given material and system is a difficult task, what makes numerical continuum modeling attractive is the significantly lower computational cost compared to discrete element modeling (DEM).

Particulate flow can be categorized in three different regimes at a broad level [25]. Rapid flow is caused mainly by particles colliding with each other. For such gas-like flow, approach based on kinetic theory of gases is most suitable. On the other extreme is solid-like flow, where particles remain in contact because of the internal friction which causes them to flow together. This flow-regime can be modeled through finite element method (FEM) based on modifications of classic plasticity theories. Sometimes, flow is driven by both particle collisions and internal friction, this regime is identified as transitional or fluid-like flow. Plasticity models can't model this behavior reasonably well. Therefore, frictional viscosity models which make use of equations from fluid mechanics have been recently proposed to govern such flows [25]. In these models, the pressure term in the momentum equation is related to microscopic properties such as inter-particle friction.

Mostly, quasi-static solid-like flow prevails in industrial hoppers, especially mass flow hoppers. Although, in a region just above hopper outlet, particles may get detached and plasticity theories will not be valid, this region is usually small. Therefore, in this thesis the focus is on various plasticity models available in the literature and their applicability through FEM in the case of hopper discharge flow.

Finite Element Method (FEM) Modeling

In continuum finite element method (FEM), particulate material is assumed as a single continuous body representing a collection of particles. This continuous material is discretized into multiple mesh elements. The behavior of each mesh element is governed by an underlying constitutive model. There is a plethora of such constitutive models, differing in their complexity, ease of implementation, and applicability to different materials. These constitutive models require material properties as input parameters which can be obtained from well-established experiments such as a uniaxial compression test, triaxial test, and shear test.

Similar to the analytical theories, particulate material is modelled as an elasto-plastic material in FEM. If material stresses lie inside the yield surface, only elastic deformation occurs. Once stresses reach the yield surface, material deforms plastically. The amount and direction of plastic deformation is governed by a plastic potential surface and a flow rule. The flow rule indicates how the plastic deformation is related to the plastic potential surface [26].

Based on how the flow rule is formulated, plasticity models are further classified as deformation theory of plasticity, which relate plastic strains to the plastic potential, and incremental theory of plasticity, where plastic strain rates are related to the plastic potential. It was observed that deformation theory of plasticity is not physically appealing and does not lead to meaningful results [27]. Hence, further developments were made in incremental theory of plasticity, where strain rates need to be integrated accurately to obtain final plastic strains.

There are a variety of elasto-plastic constitutive models available in the FEM framework. This thesis focuses on the elasto-plastic models of commercial FEM software Abaqus. Applicability of simple elasto-plastic models like the Mohr-Coulomb model in modeling hopper flow of particulate materials is explored in depth.

1.3 Organization of Thesis

The goal of this thesis is to investigate applicability of simple elasto-plastic constitutive models in finite element framework to simulate flow of particulate materials through hoppers. Chapter 2 outlines the available literature related to FEM hopper studies of cohesionless as well as cohesive particulate materials and presents specific objectives of this thesis. Chapter 3 describes different elasto-plastic models and their implementation in Abaqus. Chapter 4 demonstrates effectiveness of FEM in simulating hopper flow of cohesionless particulate materials. This chapter presents comparison with different analytical theories and empirical correlations which serves as a verification tool for the FEM results.

Chapter 5 provides a thorough one-to-one quantitative comparison of different hopper flow characteristics between FEM simulations of cohesionless dry sand and particle image velocimetry (PIV) experiments conducted on laboratory-scale hopper. Flexibility of FEM is demonstrated by presenting quantitative comparison for concentric as well as eccentric hopper.

Chapter 6 shows the applicability of FEM in modeling hopper flow of cohesive particulate materials by predicting the critical hopper outlet width. Comparison with experimental results are presented which show that FEM provides the best prediction of critical outlet width compared to theoretical or empirical estimates.

Summary of results and contributions of this thesis are presented in conclusions chapter 7. Finally, chapter 8 outlines the limitations of presented FEM modeling and recommendations for future work based on these limitations.

2. LITERATURE ON FEM MODELING OF HOPPER FLOWS

2.1 Hopper Flow of Cohesionless Particulate Material

Some particulate materials like dry sand and glass beads do not have any attractive interparticle forces. The Mohr-Coulomb yield surface of these materials has the y-intercept of zero; therefore, they are known as the cohesionless particulate materials. The steady state continuum analytical theories mentioned in previous chapter are valid for cohesionless particulate materials. Single Mohr-Coulomb yield surface can represent cohesionless particulate materials as opposed to family of yield surfaces required for cohesive particulate materials.

Many finite element method (FEM) studies exploring hopper flow of particulate materials are available in the literature [28–48]. These studies differ in terms of the shape and size of the hopper under consideration, complexity of the underlying constitutive model, implemented FEM analysis techniques, and investigated hopper flow characteristics. While some studies are concerned with the cohesive arching phenomenon [30,40,48], the majority of these studies focus on the filling or discharging hopper wall stress profiles. The stress profiles are obtained for conical and wedge-shaped symmetric hoppers as well as eccentric hopper systems [28,29,33–36,42–45,47]. Verification of the FEM wall stress profiles is achieved via comparisons to the approximate analytical theories of Janssen, Walker, and Enstad.

Few FEM studies investigate other hopper flow characteristics such as the velocity profiles [38,46] and mass discharge rates (MDRs) [37–39]. Böhrnsen et al. [46] implemented a hypoplastic model for a wedge-shaped hopper using a plane-strain FEM model and made quantitative comparisons to experimental velocity profiles. Their experimental setup consisted of a large-scale hopper with an outlet velocity controlled by a conveyor belt. The velocity profile was obtained along three horizontal paths at different heights from the outlet and compared with FEM results. The FEM analysis overpredicted the velocity profile at smaller heights, but underpredicted the velocity profiles at larger heights. Zheng and Yu [38] implemented an Eulerian FEM analysis technique using Abaqus [49] and simulated the discharge of particulate material through a conical hopper. The material was represented using the in-built Mohr-Coulomb elasto-plastic constitutive model of Abaqus without additional modifications. The dimensionless average discharge velocity profile obtained for one hopper was qualitatively compared with experiments conducted by

Cleaver and Nedderman [50] on a different hopper. The internal friction angle in the model was adjusted within the range of experimentally measured values to give a better match with experimental velocity profiles.

Wang et al. [37] implemented an Arbitrary Lagrangian-Eulerian (ALE) analysis technique within Abaqus and simulated the discharge of a generic particulate material through a wedge-shaped hopper using a linear Drucker-Prager constitutive model. The FEM MDR was shown to match well with the extended Beverloo correlation, i.e., the Beverloo correlation with the modification made by Rose and Tanaka [22]. A similar verification of the hopper MDR was completed by Zheng and Yu [38] in their work. Zheng et al. [39] investigated the effects of different model parameters on the FEM predicted hopper MDR and proposed modifications to the Beverloo correlation.

There are many experimental studies [19,20,46,51–54] available in the literature for different hopper geometries, for different discharge conditions, and for different particulate materials; however, a major hurdle in using these experimental data for direct comparisons to FEM predictions is that the experimental studies rarely report the parameters needed for the FEM constitutive model.

Based on the literature review of FEM hopper studies of cohesionless particulate material, it is clear that there is a need for thorough one-to-one quantitative comparison of FEM predicted hopper flow characteristics to experimental ones.

2.2 Hopper Flow of Cohesive Particulate Material

Unlike cohesionless particulate materials, there are non-zero attractive forces acting between particles of cohesive particulate materials. These attractive forces occur due to the phenomenon of liquid bridging, electrostatic charge, or Van der Waals forces. At the bulk macroscopic level, these attractive forces result in the Mohr-Coulomb yield surface with non-zero y-intercept known as cohesion (c). This cohesion value is often a function of applied stress for most cohesive materials. Hence, cohesive particulate materials are represented through a family of Mohr-Coulomb yield surfaces depending on the stress level.

Major problem with cohesive particulate materials stored in a hopper is the phenomenon of cohesive arching which stops the material from discharging. If the hopper outlet is smaller than a

critical value, particles can form a bridge near the outlet due to the interparticle attractive forces. This cohesive bridge hinders the smooth discharge of stored material.

Multiple approaches have been proposed to predict this critical outlet opening to prevent formation of a cohesive arch. In 1961, Jenike [2] presented pioneering work for designing industrial-scale hopper systems. These design guidelines are widely used in various bulk solid industries today. One aspect of these guidelines is the hopper minimum outlet width to ensure reliable flow of cohesive bulk solids. Although the critical outlet width predicted by Jenike works well to avoid cohesive bridging at the outlet, multiple experiments reported in the literature suggest that the Jenike estimate of the critical outlet width is conservative [24,55,56]. Indeed, the experimentally-observed critical outlet width can be half of the Jenike prediction [24]. Enstad [15] presented an analytical theory aimed at reducing this overdesign. He demonstrated a significant reduction in the overdesign when the critical outlet width predicted using his approach was compared against the experiments of Eckhoff and Leversen [24]. Jenike's design guidelines are more commonly used compared to Enstad's analysis due to easy-to-use design charts and the availability of correlations resulting in a quick outlet width estimate.

Early FEM modeling studies concerned with predicting critical outlet width involved static analysis with controlled release of the stored material either by incremental reduction in opposing forces applied at the outlet [28] or by incremental deactivation of zero displacement boundary conditions at outlet nodes [40]. Kamath and Puri [40] demonstrated success in predicting the critical outlet width using FEM for wheat flour. However, in addition to being a static-controlled analysis, the elastic modulus of the material was obtained from one hopper experiment such that the FEM arch matched with the experimental arch. A second hopper experiment with the same material was then used to validate the model. Ooi et al. [48] provided a detailed FEM analysis for how the filling stresses vary near the hopper outlet using elastic, Mohr-Coulomb, and Cam Clay constitutive models. They also reported the stress variations with respect to the wall friction and angle made by the assumed circular arch with the hopper wall. The FEM wall pressures were shown to match well with the analytical theory of Walker [14]. Although, no experimental comparison of the critical outlet width was reported, Jenike's theory was concluded to give a conservative prediction. Keppler [30] presented a different approach using elastic FEM to visualize the arch formed by deleting elements under tension and elements where the elastically-determined major principal stress exceeds a critical value measured from a biaxial test. The shape of the

resulting arch was parabolic. Quantitative experimental validation of this work is not available in the literature.

Based on the literature survey on FEM modeling of cohesive particulate materials, there is a need to investigate applicability of FEM in predicting the critical hopper outlet opening by performing quantitative comparison to experimental data.

2.3 Thesis Goals and Objectives

The goal of this dissertation is to assess the applicability of continuum FEM modeling based on simple elasto-plastic constitutive models in predicting hopper flow characteristics of cohesionless and cohesive particulate materials.

The specific objectives of the thesis are enumerated here:

1. Develop FEM computational models to simulate hopper discharge of cohesionless material based on elasto-plastic models of Abaqus to obtain steady state flow characteristics.
2. Compare flow characteristics of wedge-shaped hopper obtained through the Mohr-Coulomb and the linear Drucker-Prager elasto-plastic models.
3. Verify flow characteristics predicted by FEM through comparison to analytical theories/empirical correlations for simplified hopper geometry.
4. Perform parametric study to investigate effect of model parameters on the flow characteristics and on agreement with analytical theories.
5. Design and build a laboratory-scale hopper for quantitative validation of FEM results.
6. Perform particle image velocimetry (PIV) experiments and image analysis on discharging cohesionless material to obtain different flow characteristics.
7. Obtain flow characteristics, such as the velocity profiles, mass discharge rate (MDR), duration of steady MDR (T_{SS}), and free surface profiles from the experiments.
8. Show quantitative comparison of flow characteristics for concentric and eccentric hoppers to assess flexibility of FEM.
9. Simulate behavior of cohesive particulate materials and predict the critical outlet width (COW) of wedge-shaped hopper to ensure uninterrupted discharge.
10. Compare FEM predicted COW with theoretical estimates of Jenike and Enstad, and with correlation of McLean.

11. Investigate effect of filled material height, hopper angle, and model parameters on the COW estimate.
12. Compare the FEM COW to experimental results available in literature to assess applicability of FEM based on simple elasto-plastic constitutive model in simulating cohesive particulate material.

It is expected that this thesis will further clarify the strengths and limitations of the FEM approach based on relatively simple elasto-plastic constitutive models and necessary modifications that need to be made to obtain reasonable hopper flow characteristics.

3. ELASTO-PLASTIC CONSTITUTIVE MODELS

As mentioned before, FEM is based on the assumption of continuum material. This continuum material is discretized into several small mesh elements. The behavior of these mesh elements in terms of stresses and strains is governed by the underlying constitutive model. For modeling particulate materials, elasto-plastic constitutive models prove useful. This chapter provides detailed information on the different elasto-plastic models and corresponding implementation in the context of commercial FEM software Abaqus.

3.1 Elasto-Plastic Models of Abaqus

3.1.1 The Mohr-Coulomb Model

As mentioned before, Mohr-Coulomb yield surface is often used as a first approximation to govern real material behavior. Many advanced plasticity models are modifications of the Mohr-Coulomb yield surface.

The Mohr-Coulomb yield surface presented in Figure 1.2b can be represented in terms of principal stresses $(\sigma_1, \sigma_2, \sigma_3)$ as,

$$\frac{\sigma_1 - \sigma_3}{2} + \frac{\sigma_1 + \sigma_3}{2} \sin\phi - c\cos\phi = 0, \tag{3.1}$$

For a three dimensional case, there will be six such equations [26] depending on relative magnitudes of σ_1, σ_2, and σ_3. When plotted in the principal stress-space, this results in a yield surface having a cross-section of an irregular hexagon (Figure 3.1a). If the material stresses lie inside this yield surface, material will undergo reversible elastic deformation. However, if the stresses lie on this yield surface, irreversible plastic deformation will occur. Stresses outside this yield surface are not allowed. The plane of cross-section (Figure 3.1b) is known as the deviatoric plane ($\sigma_1 = \sigma_2 = \sigma_3$). This cross-section reduces to Figure 3.1c under plane stress ($\sigma_3 = 0$) conditions.

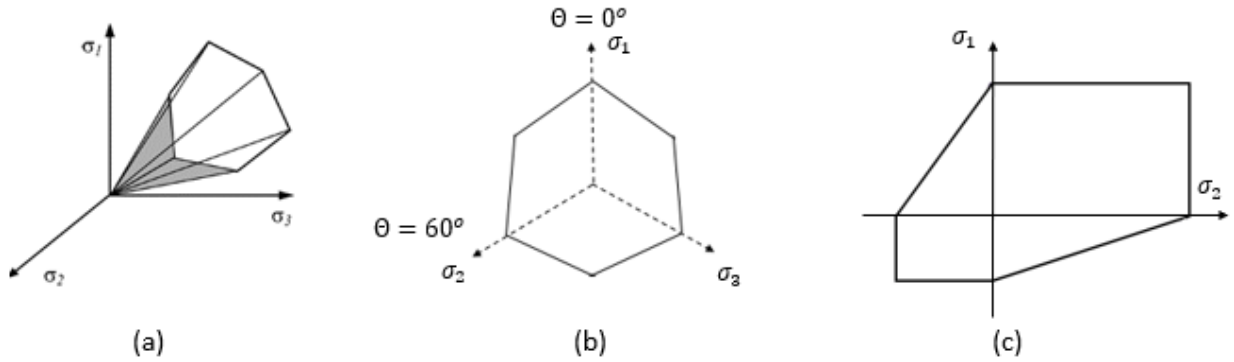

Figure 3.1. Mohr-Coulomb yield surface in (a) 3D space [57] (b) deviatoric plane [49] (c) plane stress condition ($\sigma_3 = 0$) [58].

Isotropic materials fail in the same way in all directions. For these materials, it is useful to represent the yield surface in terms of stress invariants, which do not depend on the rotation of coordinate system. Figure 3.2 shows the representation of the Mohr-coulomb yield surface in the q (Mises equivalent stress) $-$ p (pressure) plane. Here, Θ is another invariant known as the deviatoric polar angle and varies between 0^o to 60^o. Detailed expressions of these terms can be found in Abaqus theory guide [49].

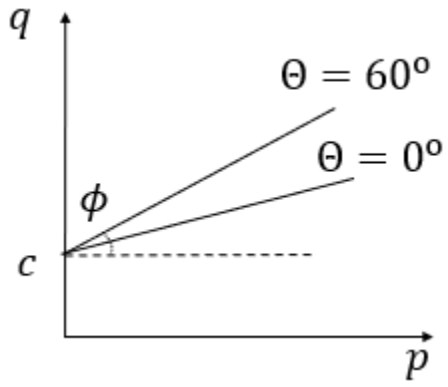

Figure 3.2. The Mohr-Coulomb criterion in $q - p$ plane [49].

The yield surface only provides stress states at which the material will start to yield plastically. Certain assumptions need to be made to determine the components of plastic deformation after yielding. Note that such a 'yield surface' can also be represented in strain rate space, but since plastic strains outside this 'yield surface' are allowed, this surface is known as a 'flow or plastic potential surface'. The resulting strain rates are indicated by an arrow normal to

this plastic potential surface. The length of such an arrow depends on the scalar plastic multiplier '$\dot{\lambda}$'. As explained later, 'λ' can be determined using the condition that stresses will remain on the yield surface as material continues to deform plastically. This condition is known as the consistency condition. Similarly, the plastic potential surface can be represented in terms of invariants (volumetric strain rate ($\dot{\varepsilon}_{vol}$) in place of p and equivalent shear strain rate ($\dot{\bar{\gamma}}$) in place of q) (Figure 3.3). This surface depends on parameter ψ, known as the dilation angle. The dilation angle controls volumetric deformation of the material. It is a measure of plastic volume strain compared to shear strain [59].

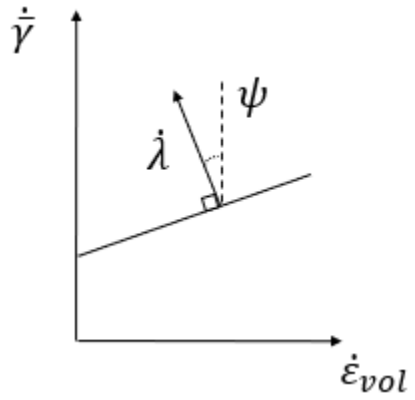

Figure 3.3. The plastic potential surface in the $\dot{\bar{\gamma}} - \dot{\varepsilon}_{vol}$ plane.

3.1.2 The Drucker-Prager Model

It can be observed that a difficulty arises when stress states lie on the corners of the Mohr-Coulomb yield surface, as a normal direction is not clearly defined at such corners. Although this issue is handled by commercial FEM software like Abaqus, it proves computationally expensive. Therefore, Drucker and Prager [60], suggested a smooth yield surface approximating the original Mohr-Coulomb yield surface. This linear yield surface in $q - p$ plane now depends on different internal friction angle 'β' and cohesion 'd' (Figure 3.4a) which are related to the corresponding Mohr-Coulomb parameters. In 3D space, this yield surface can be represented by a smooth cone (Figure 3.4b).

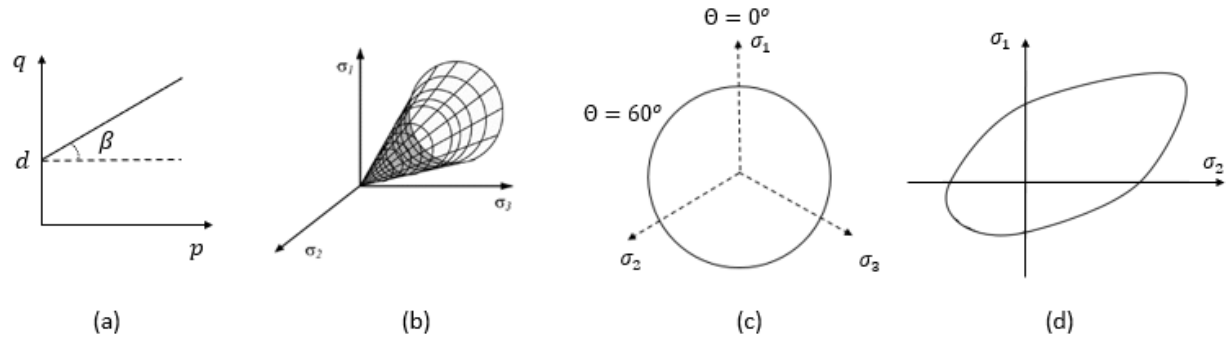

Figure 3.4. The Drucker-Prager yield surface in (a) $q - p$ plane (b) 3D space [57] (c) deviatoric plane [49] (d) plane stress condition ($\sigma_3 = 0$) [58].

3.1.3 Conversion of Model Parameters

Parameters of the Mohr-Coulomb model can be obtained directly through bulk material tests such as the Schulze ring shear cell test. Hence, when applying the Drucker-Prager model, it is important to convert the Mohr-Coulomb parameters. This can be done by as many as four ways as shown in Figure 3.5. In chapter 4, wedge-shaped hopper is modeled as a plane strain system. Parameters obtained through the matching plane strain response [49] (Figure 3.5c) are most appropriate and as shown in next chapter, leads to equivalent results as that of the Mohr-Coulomb model. The corresponding conversion equations are,

$$\tan \beta = \sqrt{3} \sin \phi \;\; \& \;\; d = c \cos \phi, \tag{3.2}$$

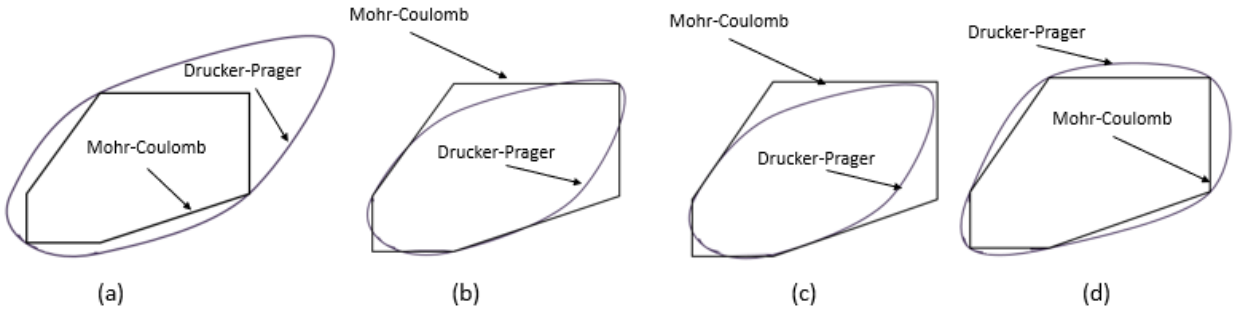

Figure 3.5. Conversion of parameters by matching, (a) outer vertices [58] (b) inner vertices [58] (c) plane strain response [49] and (d) triaxial test response [49].

It should be noted that the Drucker-Prager model parameters can also be obtained directly from uniaxial and diametrical compression tests [61,62].

3.1.4 Non-Associative Flow Rule

Early attempts were made using associated plasticity models, where the plastic potential surface is the same as the yield surface ($\psi = \phi$). Associated plasticity is based on Drucker's postulate for stable materials [26]. It was observed that this model produced unrealistically large volume increase (dilation) in the particulate material as compared to experimental results. Many real materials do not follow Drucker's postulate of associated plasticity. Hence, to control this excessive dilation, further modifications were suggested, such as use of non-associated plasticity and addition of a cap at the end of the yield surface [63].

In non-associative plasticity, the plastic potential surface is different than the yield surface implying $\psi \neq \phi$ (Figure 3.6). A dilation angle of zero degrees results in isochoric plastic deformation. For many particulate materials such as sands, the dilation angle is non-zero during initial shear deformation and is much smaller than the corresponding internal friction angle ($\psi < \phi$).

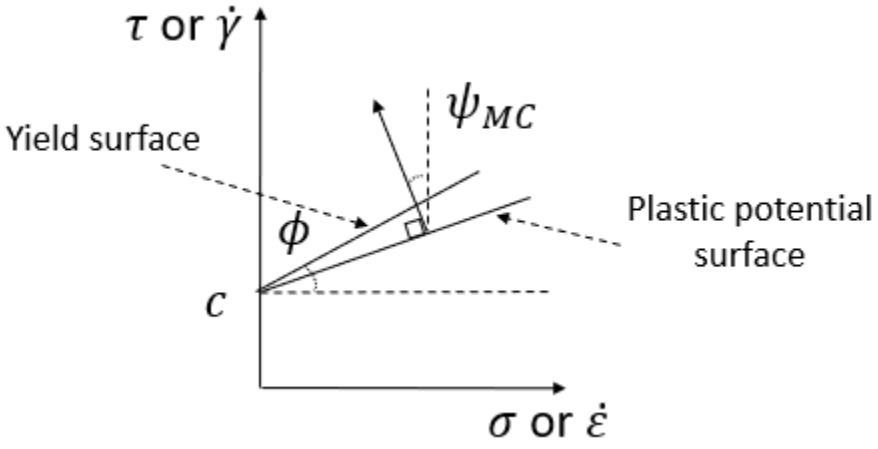

Figure 3.6. Non-associative plastic potential.

3.1.5 The Drucker-Prager Cap Model

Drucker [63], introduced another way to control this excessive dilation, which is to add an elliptical cap at the end of the linear plastic potential surface. Material yielding on the cap will undergo contraction and material yielding on the linear failure surface will dilate (Figure 3.7).

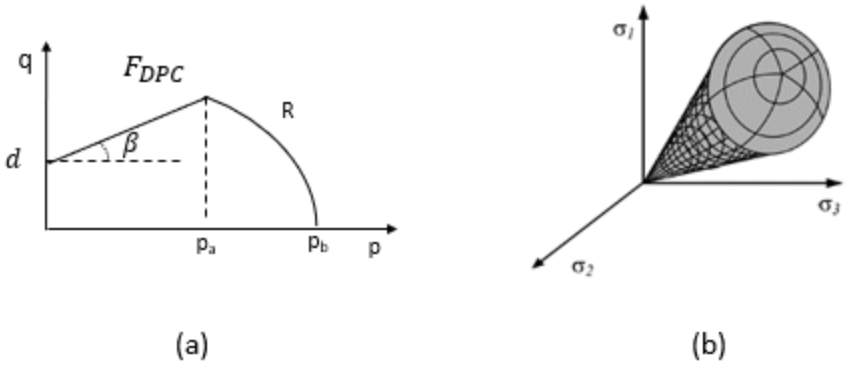

Figure 3.7. The Drucker-Prager Cap yield surface in (a) the $q - p$ plane and (b) 3D space [57].

Drucker also introduced the concept of work/strain hardening where the position of the cap changes with the amount of plastic deformation. Similar type of hardening can also be applied to the Mohr-Coulomb and the linear Drucker-Prager models by changing model parameters with plastic deformation. As opposed to an elastic-perfectly plastic material, this type of elastic-hardening plastic material has different yield surfaces based on the plastic deformation.

The plastic potential surface of the DPC model in Abaqus is elliptic even in the linear failure region (Figure 3.8). Although this DPC model has been proven to be quite useful for particulate material under high stress situations such as powder compaction [61,64], this model gives unrealistic results for hopper flow of cohesionless particulate materials. Material near the free surfaces undergoes significant dilation due to the large dilation angle at low stresses caused by the elliptic plastic potential surface.

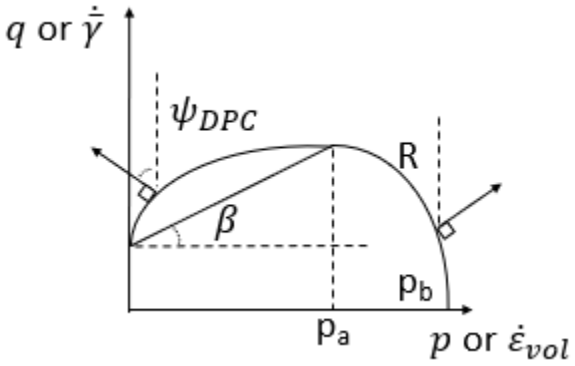

Figure 3.8. Drucker-Prager Cap model of Abaqus.

3.2 FEM Implementation

Continuum modeling of a particulate material in a FEM framework is based on three sets of governing equations [27]. All material points inside the mesh need to satisfy the equilibrium equation, i.e., Newton's first law of motion is satisfied by each material point of the mesh. Abaqus uses the following dynamic equilibrium equation,

$$\boldsymbol{M}\ddot{\boldsymbol{u}} = (\boldsymbol{F} - \boldsymbol{I}). \tag{3.3}$$

Here, $\boldsymbol{M}$ is the nodal mass matrix and $\ddot{\boldsymbol{u}}$ is the acceleration vector caused by the external forces ($\boldsymbol{F}$) resulting from body forces and load boundary conditions, and the internal forces ($\boldsymbol{I}$) resulting from stresses developed inside the mesh element and contact forces.

Contact forces are generated due to interaction between the nodes of the material and faces of the hopper wall. In this thesis, coulomb type frictional interaction is used and Abaqus implements this frictional interaction through the use of a penalty contact algorithm, which determines the magnitude of the contact force based on node-to-face penetrations at the previous time step (x) and a penalty stiffness (s),

$$F_{contact} = s * x. \tag{3.4}$$

The second set of equations come from the requirement of geometric compatibility between displacements and strains. In Abaqus, strains $\boldsymbol{\varepsilon}$ can be determined as the spatial gradient of the displacement vector, $\boldsymbol{u}$,

$$\boldsymbol{\varepsilon} = \frac{1}{2}\left(\frac{\partial \boldsymbol{u}}{\partial \boldsymbol{x}} + \left[\frac{\partial \boldsymbol{u}}{\partial \boldsymbol{x}}\right]^T\right). \tag{3.5}$$

The third set of equations bridges the gap between stresses and strains with a specified stress-strain relationship. This relationship is the underlying constitutive model. As mentioned earlier, the elasto-plastic constitutive models are considered in this work.

Elasto-plastic modeling starts from the assumption of additive strain rates,

$$\dot{\boldsymbol{\varepsilon}} = \dot{\boldsymbol{\varepsilon}}^{elastic} + \dot{\boldsymbol{\varepsilon}}^{plastic} \tag{3.6}$$

The total strains or strain rates can be divided into elastic and plastic components that are independent of each other. Rice [65], showed that such a division of strains/strain rates is applicable if corresponding elastic strains are relatively small. The elastic part is governed by the Hooke's theory of linear elasticity,

$$\boldsymbol{\sigma} = \boldsymbol{D} * \boldsymbol{\varepsilon} \tag{3.7}$$

Here, $\boldsymbol{D}$ is the fourth order elasticity tensor expressed in terms of the modulus of elasticity E and Poisson's ratio ν. There exists a one-to-one relationship between elastic stresses and strains.

In Abaqus/Explicit, plastic strains are determined iteratively. Total strains are known from a kinematic estimate of the previous time step, plastic strains are guessed, and then elastic strains are obtained through the additive strain rate formula (Eq. (3.6)). After obtaining elastic strains, Hooke's law of elasticity is used to get stresses. This process is repeated iteratively until the yield surface and plastic potential surface conditions are satisfied. The final set of equations contain the plastic multiplier λ. For the overall structure of calculating plastic deformation, the reader may refer to [26,66], and for detailed derivation of these equations, refer to [49].

Abaqus uses another scalar known as the equivalent plastic strain, ($\overline{\varepsilon^{plastic}} = \sqrt{\frac{2}{3}\varepsilon_{ij}^{plastic}\varepsilon_{ij}^{plastic}}$) in place of λ to determine the magnitude of plastic deformation. The relationship between $\overline{\varepsilon^{plastic}}$ and λ varies depending upon the plasticity model under consideration.

For the Mohr-Coulomb model in Abaqus, it is observed that an exact 0^{o} dilation angle cannot be specified and the minimum value allowed is 0.1^{o}. This restriction is due to the definition of plastic potential,

$$\varepsilon_{ij}^{plastic} = \frac{\overline{\varepsilon^{plastic}}}{g}\frac{\partial G}{\partial \sigma_{ij}}, \tag{3.8}$$

where,

$$g = \sigma_{ij}:\frac{\partial G}{\partial \sigma_{ij}} = f(\tan\psi) \Rightarrow \lambda = \frac{\overline{\varepsilon^{plastic}}}{f(\tan\psi)}, \tag{3.9}$$

It can be observed that for the Mohr-Coulomb model, the dilation angle (ψ) is in the denominator of the plastic multiplier λ. Therefore, ($\psi = 0^{o}$) is not allowed as it will give an indeterminate value of λ. A non-zero ψ implies that the bulk material will keep dilating forever with time as ($\varepsilon_{vol}^{plastic} = \lambda \tan\psi$) [66] and the corresponding density will keep reducing. Although this effect is insignificant in short term hopper simulations, it is observed that the bulk density reduces to unrealistic values if simulations are run for a very long time.

3.3 Strengths and Limitations

Finite element modeling based on the simple elasto-plastic constitutive models has the advantages of easy implementation, being computationally inexpensive, use of standardized tests to obtain input parameters, and can produce quick results. The phenomenon of material hardening/softening with respect to shear deformation can be implemented through minor modifications. Behavior of particulate materials in different large-scale systems can be simulated based on the same elasto-plastic model.

The accuracy of such FEM modeling depends on the extent of the experimentally measured bulk material properties. Bulk material properties for a range of stress levels including near-zero stresses are required to obtain accurate hopper flow characteristics. This aspect can be perceived as a limitation, because material property measurement at near-zero stresses is difficult if not impossible.

For the Mohr-Coulomb and the linear Drucker-Prager models, material can dilate but it cannot contract. Implying that the density of material is the same throughout the hopper after filling. In reality, some variation in the bulk density can be expected with respect to the height from the hopper outlet. These models are not appropriate for simulating highly compressible particulate materials.

As mentioned before, the Drucker-Prager Cap model can simulate material compression, but the elliptical plastic potential surface makes it difficult to control the material dilation at near-zero stresses. The DPC model was found to produce unrealistic dilation near the free surface of the cohesionless particulate material discharging through hopper.

Another limitation of FEM analysis presented in this thesis is related to the phenomenon of localization of shear zones. Shear zones are the thin flow regions which develop between two material layers as one layer moves relative to another. It is observed that such shear zones localize, i.e., reduce in thickness with increasing shear deformation [3]. These shear zones are also observed in hopper flow experiments [67]. Formation of shear zones is important as they cause regions of material to start moving suddenly which results in quasi-static oscillations in hopper pressure and material bulk density [3]. Furthermore, these shear zones vary in thickness depending upon the hopper wall roughness, particle size, density, shape, and microscopic properties. It is reported that shear zones are formed in internal bulk material and along the hopper walls. Resulting pulsations in wall pressure can cause silo problems commonly known as silo honking/music/quaking. As

these shear zones are directly dependent on microscopic properties of the particles, the FEM modeling presented in this work is unable to capture this phenomenon.

There are regularization techniques available in literature that control the thickness of shear zones formed in FEM. Regularization techniques modify the constitutive model to include a characteristic length related to microscopic particle level properties. Two such techniques: micro-polar continuum [68] and non-local methods [69] are discussed next.

A micro-polar elasto-plastic model includes another degree of freedom known as Cosserat rotation, which is independent of displacement of the given mesh element. This rotation is now defined in terms of mean particle diameter and corresponding stress definitions are also modified to include couple stresses and dependence on mean particle diameter. Due to the presence of the mean particle diameter, this model can capture variations in hopper flow characteristics as particle size changes, but this model is complex and not straightforward to implement.

Non-local technique makes use of averaging over a region so that stress state of a given mesh element is now dependent on stresses of neighboring mesh elements. The averaging length is obtained through experimental measurement of the shear zone thickness, which defeats the predictive ability of non-local methods. This technique is particularly useful is eliminating the mesh dependency observed in the thickness of shear zones formed in FEM based on simple elasto-plastic models.

In present work, without any regularization technique, the thickness of shear zones or region of yielding mesh elements does depend on the mesh density. Hence, the hopper flow characteristics also exhibit slight dependence on the mesh density. The effect of mesh density is shown in multiple sections of this thesis to demonstrate convergence of obtained results. But it is acknowledged that the phenomenon related to shear zones cannot be captured by present analysis. While, complex models such as the micro-polar elasto-plastic and non-local elasto-plastic models may be able to predict the dependence of particle properties on bulk behavior and capture real thickness of the localized shear zones, these models are not easy to implement and require additional input parameters.

3.4 Other Elasto-Plastic Models

Apart from conventional plasticity models defined by a yield surface, plastic potential surface, and flow rule some researchers have also introduced models which do not have a direct

specification of the yield surface [70]. These models assume a non-linear relationship between the current state of stresses and plastic strain rates. Moreover, a yield surface and a plastic potential surface are often implied inherently in such models. Hypoplastic models are alternatives to the traditional elasto-plastic models, but they are much more complex to implement and not directly available in standard commercialized numerical software.

Some materials show increased strength with time due to a time consolidation effect. The class of plasticity models dealing with time effect on material strength are known as viscoplastic constitutive models. More complex models, which aim to incorporate anisotropic behavior of real materials can also be found in literature [12]. These models make use of fabric tensors, which store different material properties depending upon the direction and material microstructure. Again, these complex models are difficult to implement in standard software as they require building a user-defined material with desired properties.

4. HOPPER FLOW OF COHESIONLESS PARTICULATE MATERIALS

A generic cohesionless particulate material discharging from a wedge-shaped hopper system is simulated in this chapter. Arbitrary values are chosen for the Mohr-Coulomb yield surface and the wedge-shaped hopper is assumed to be a plane-strain system. Corresponding FEM results are compared with analytical theories for verification purposes and effect of model parameters on this comparison is explored.

4.1 Simulation Domain

Figure 4.1a shows the simulation domain for a representative 2D converging hopper geometry. Half of the hopper is simulated, assuming symmetry along the hopper centerline. Similar symmetry boundary conditions are used on the front and back surfaces so as to represent the middle section of the original hopper which is assumed to have a long length along the z direction (Figure 4.1b). Because of these boundary conditions, this hopper system essentially reduces to a plane strain ($\varepsilon_{zz} = 0$) system. According to Jenike [71], a plane strain assumption can be made for hoppers with outlet length greater than three times the outlet width.

The hopper side walls are rigid bodies whose motion is governed by the assigned reference point. Coulomb type frictional interaction exists between the inner surface of the rigid wall and outer surface of the hopper material. Although the simulation procedure is explained for a converging hopper in this section, bin-hopper or flat-bottomed silo systems can also be setup in a similar way.

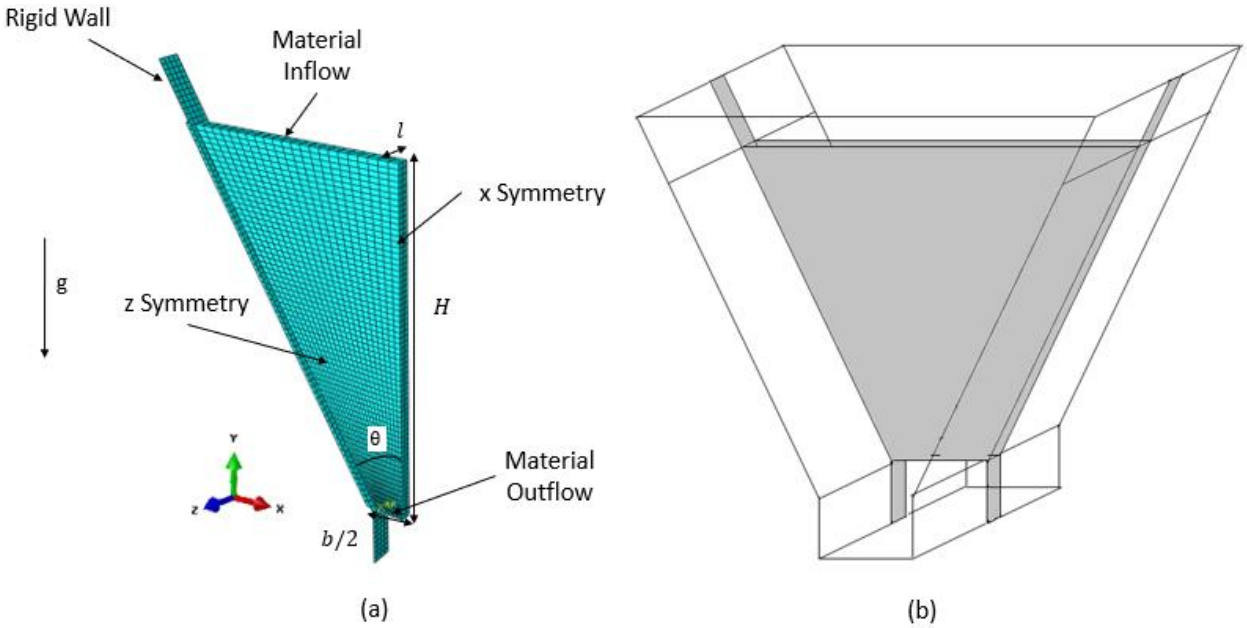

Figure 4.1. Converging hopper (a) Simulation domain. (b) Physical system.

Overall simulation consists of two dynamic steps with explicit time integration scheme. During the first step, the outlet is closed, and material settles as gravity body force is applied smoothly. Such smooth application of the gravity force gets rid of transients associated with instantaneous force application. During the second step, the outlet is opened by deactivating the zero normal velocity boundary condition, and material is allowed to reach a steady state. The duration of the first step is such that the kinetic energy of the static material reaches zero near the end, whereas the duration of second step is large enough to observe a steady state velocity profile during discharge. The actual simulation duration depends on the material properties.

4.2 Analysis Technique

Hopper simulations can be performed with three different analysis techniques within Abaqus. Lagrangian analysis is suitable for situations where material remains static. Since mesh nodes are fixed to the material, significant deformation causes mesh elements to distort, thus reducing the quality of the mesh and reliability of the results [38]. Eulerian analysis is suitable for hopper discharge simulations as in this technique the mesh elements are fixed in space and do not deform even as the material flows through the mesh. Abaqus uses 'Lagrangian-plus-remap' first order advection technique to momentarily deform the mesh and remap corresponding state

variables to the original undeformed mesh. With the aid of the Eulerian Void Fraction (EVF) variable, it is also possible to visualize the material free surface in Abaqus. In an Arbitrary Lagrangian-Eulerian (ALE) analysis, nodes at the hopper outlet remain fixed in space and the material can flow out of the outlet. Mesh nodes above the outlet move independently of the discharging material and the domain is re-meshed to minimize element distortion. The number of elements remain the same even as the volume of the material above the outlet keeps reducing. Although ALE can model the initial stage of the hopper discharge process [37], it is observed that this method fails in later stage as elements get too distorted. These techniques are summarized in Table 4.1 and corresponding mesh element distortions are compared in Figure 4.2 for plane strain hopper.

Table 4.1. Comparison of Abaqus analysis techniques

Analysis technique	**Definition**	**Pros**	**Cons**
Lagrangian	– Mesh nodes are fixed to the material. – Elements deform with flowing material	– Fast speed – Robust kinematic contact – 2D or 3D domain – Explicit or Implicit time integration	– Large element distortions – New material cannot enter the domain
Eulerian	– Mesh nodes are fixed in space – Elements do not deform with flowing material	– No element distortions – New material can enter the domain	– Slow speed – Penalty contact algorithm prone to excessive penetration – 3D domain with Explicit time integration only
ALE	– Domain re-meshing as material moves to minimize distortions	– Robust kinematic contact – Parallelization not possible – Very slow speed	– Fails for extreme distortions

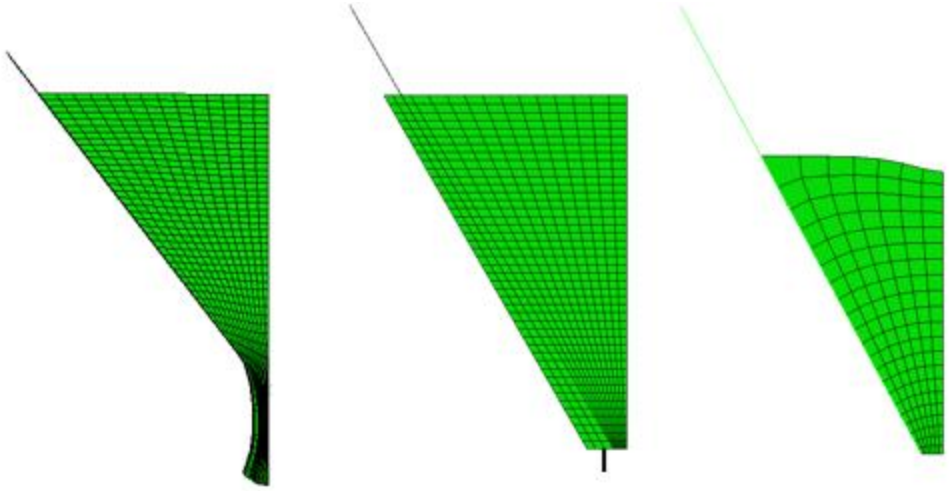

Figure 4.2. Mesh distortion using (a) Lagrangian, (b) Eulerian, and (c) ALE analysis technique for plane strain hopper.

The Eulerian analysis technique is implemented in this chapter. Caution must be used as it has been observed that the penalty contact algorithm, for contact between the material and wall, is not robust for this analysis technique. The penalty contact algorithm is based on penetration of material nodes into the rigid wall surface. If the wall is placed such that it cuts through Eulerian mesh elements, tracking the material interface becomes difficult resulting in dubious contact forces and, therefore, a questionable flow profile. It is observed that for better implementation of contact forces, wall should be placed along element edges.

A material inflow boundary condition is used on the top material surface (Figure 4.1a) to prolong the steady state discharge duration. It is observed that in absence of a material inflow boundary condition, the outlet center-node velocity remains steady for some period before gradually reducing to zero as the material approaches the end of the discharge process. Figure 4.3 shows a comparison of the hopper outlet center-node velocity for a free top surface and for a continuous material inflow boundary condition. Hence, to obtain steady state results, a material inflow boundary condition is implemented.

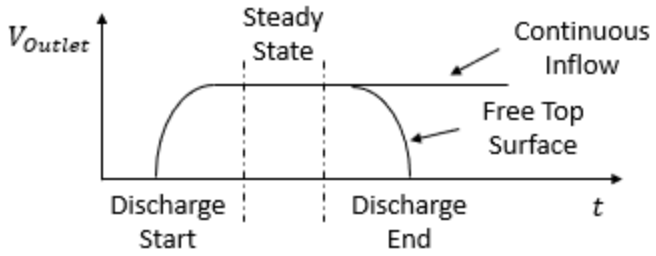

Figure 4.3. Top surface boundary condition comparison.

4.3 Material Properties and Hopper Dimensions

Generic cohesionless particulate material with properties similar to soda-lime glass beads is used in this chapter. Corresponding material parameters and dimensions of the plane strain converging hopper system are listed in Table 4.2.

Table 4.2. Material properties and dimensions of the hopper

Property	Value
Bulk density, ρ_b	1600 kg/m^3
Elasticity modulus, E	10 MPa
Poisson's ratio, ν	0.2
Internal friction angle, ϕ	20^o
Wall friction angle, ϕ_w	5^o
Dilation angle, ψ	15^o to 0^o
Hopper half angle, θ	30^o
Hopper outlet width, b	25 cm
Hopper height, H	3 m

The material is represented through the Mohr-Coulomb elasto-plastic constitutive model so that one-to-one comparison to continuum theories can be made. The dilation angle is reduced linearly to capture the phenomenon of shear deformation at constant volume. After significant shearing, particulate materials stop dilating and further deformation occurs at constant volume [16,66]. This behavior is observed in tri-axial tests as well as experiments performed on flat-bottom bins [31]. Therefore, the dilation angle needs to be set to zero after a certain amount of deformation at which the bulk material reaches a constant volume. This effect is implemented by linearly decreasing the dilation angle from an initial value, ψ_i to 0^o as the solid fraction of bulk

material decreases from an initial value of η_i to constant-volume value of η_{cv}, as shown in Figure 4.4.

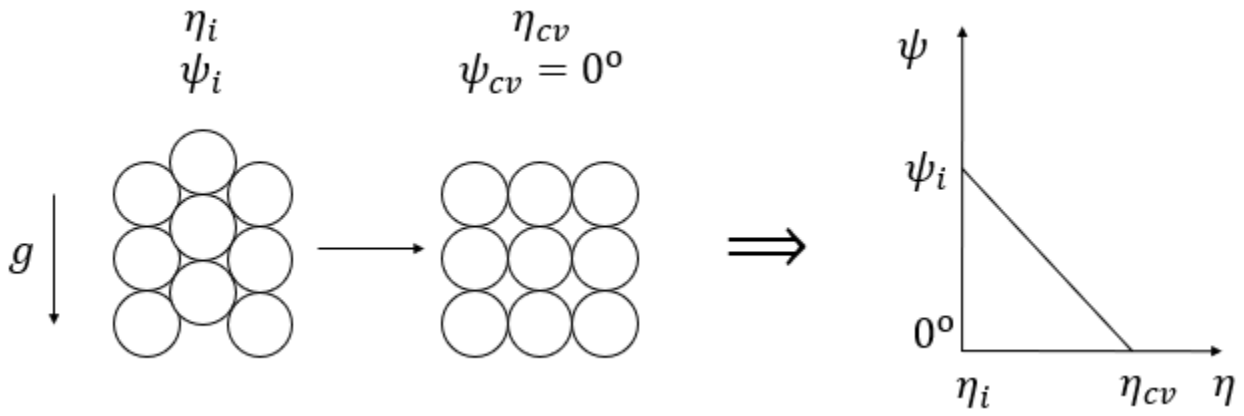

Figure 4.4. Variation of dilation angle (ψ) with solid fraction (η).

For the generic cohesionless particulate material containing spherical particles, the initial and constant-volume solid fraction values are determined based on the assumed particle packing structure. It is assumed that initially densely packed particles have a packing fraction (η_i) of 0.64 (corresponding to random close packing of spheres) and after some deformation the dilation stops when particles rearrange themselves in a cubic lattice formation, which corresponds to a solid fraction (η_{cv}) of $\pi/6$. The critical volumetric strain at which material deforms with a constant volume can be obtained by the logarithmic strain measure,

$$\varepsilon_{vol} = \ln \frac{\eta_i}{\eta_{cv}} \approx 0.2, \tag{4.1}$$

This dependence of dilation angle on material volumetric strain is implemented through use of a field variable and the VUSDFLD subroutine of Abaqus. The dilation angle is varied linearly with respect to the field variable which is set to be equal to the volumetric strain. Table 4.3 gives values of the assigned field variable and corresponding dilation angles. The subroutine determines the volumetric strain in current time step, then interpolates the dilation angle for that volumetric strain. For field variable (volumetric strain) values greater than 0.2, the dilation angle is 0^o.

Table 4.3. Field variable assignment

Dilation angle	Field variable = Volumetric strain
15º	0
0º	0.2

Material dilation is usually associated with softening for cohesionless materials [59]. This material softening can be implemented in a similar way where the internal friction angle is also linearly reduced with respect to the volumetric strain. Such softening is implemented in the chapter 5 when quantitative comparison is made with experimental results, but is ignored in present chapter as the steady state approximate analytical theories are based on the assumption of constant internal friction angle.

4.4 Post Processing

By default, output variables such as velocity and stress can be viewed throughout the simulation domain with respect to the global co-ordinate system in Abaqus. Figure 4.5 shows an example of contour and symbol plots for the velocity output variable.

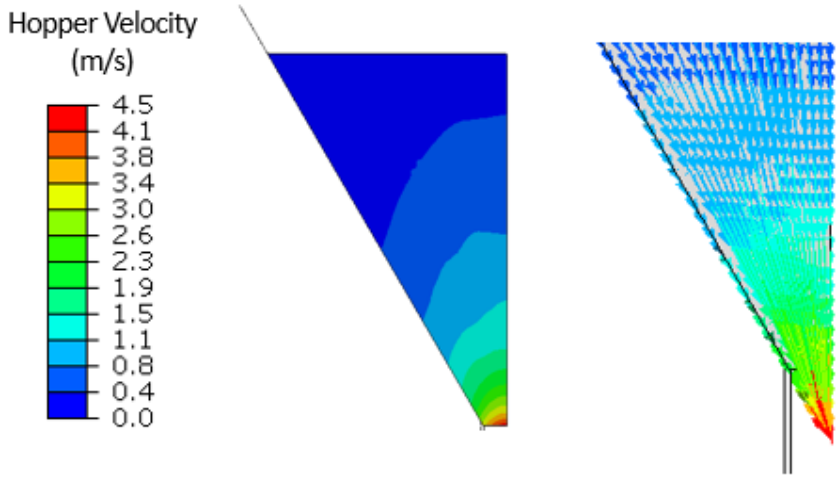

Figure 4.5. Example velocity profile, (a) contour plot and (b) symbol plot.

For comparison with steady state theories, output variables along desired paths are obtained. For example, to visualize the vertical velocity distribution along the hopper outlet, a line path is created from the outlet center to the wall (Figure 4.6) and the velocity component V2 (along the

direction of gravity) is obtained at various points along this path. Similarly, the wall normal stress is obtained on points of the line path drawn near the wall (Figure 4.6) after transforming the stress components from the global co-ordinate system (Global CSYS) to the wall co-ordinate system (Wall CSYS) (Figure 4.6). A Python script is utilized to construct such paths and transform stresses for desired time steps. For calculating mass discharge rate, density data is also obtained for points on the outlet path along with velocity data. The mass discharge rate is then calculated by summing all local mass discharge rates between two sequential points on the outlet path.

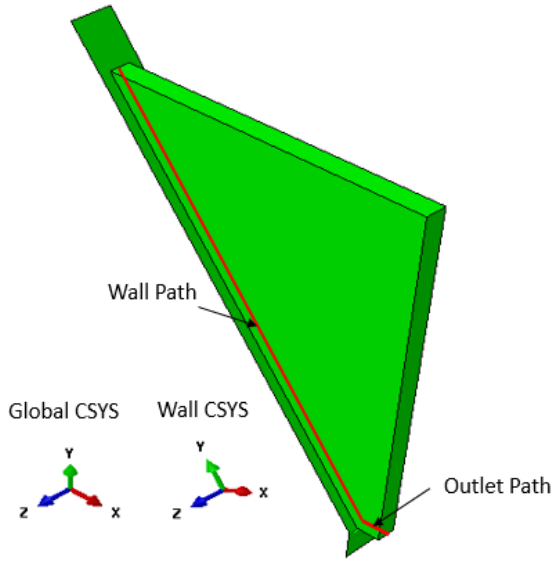

Figure 4.6. Line paths along (a) hopper outlet, (b) hopper wall.

4.5 Results and Discussion

This section starts with mesh convergence analysis and then details various characteristics obtained for a converged simulation. The equivalence between results obtained through the Mohr-Coulomb model and the Drucker-Prager model is demonstrated. Various simulation characteristics are compared with steady state approximate analytical theories. A parametric study is also performed to show how flow characteristics vary with different model parameters.

4.5.1 Convergence Analysis

Mesh and time step convergence is performed in this section. Figure 4.7a shows the velocity distribution across the hopper outlet in steady state. It can be observed that as the number

of elements is increased, the outlet velocity distribution converges. Figure 4.7b shows the convergence of discharging wall normal stress results. Therefore, it is concluded that around 3,000 elements are enough to get converged results for this geometry.

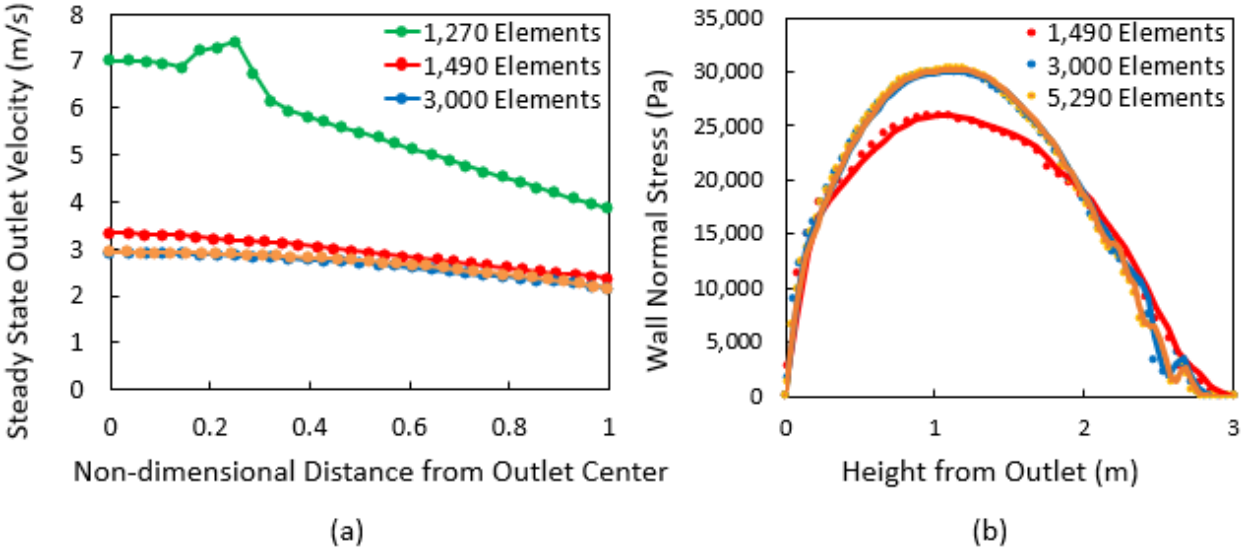

Figure 4.7. Convergence of (a) outlet velocity distribution and (b) wall normal stress.

Similarly, time step convergence analysis is also performed for this geometry as the simulations are based on an explicit time integration scheme. It is concluded that the default time step determined by Abaqus is small enough to get stable converged results. Abaqus uses material elastic properties to determine the stable time increment needed for dynamic analyses. Determination of this time step is based on the time required for a dilatational wave to cross the element of minimum size [49].

$$\Delta t = L_{min}/c_d. \tag{4.2}$$

where,

$$c_d = \sqrt{E\rho\left(\frac{1-\nu}{(1+\nu)(1-2\nu)}\right)}. \tag{4.3}$$

4.5.2 Initial Height Independence

For a hopper geometry with a given outlet width, it has been observed that if the material height is large enough, then a further increase in material height does not affect the hopper velocity

profile significantly. Figure 4.8 shows the variation of outlet center-node velocity with material height. It is decided to fix the hopper material height at which $\frac{\Delta V_{outlet}}{\Delta H} \approx 1\%$.

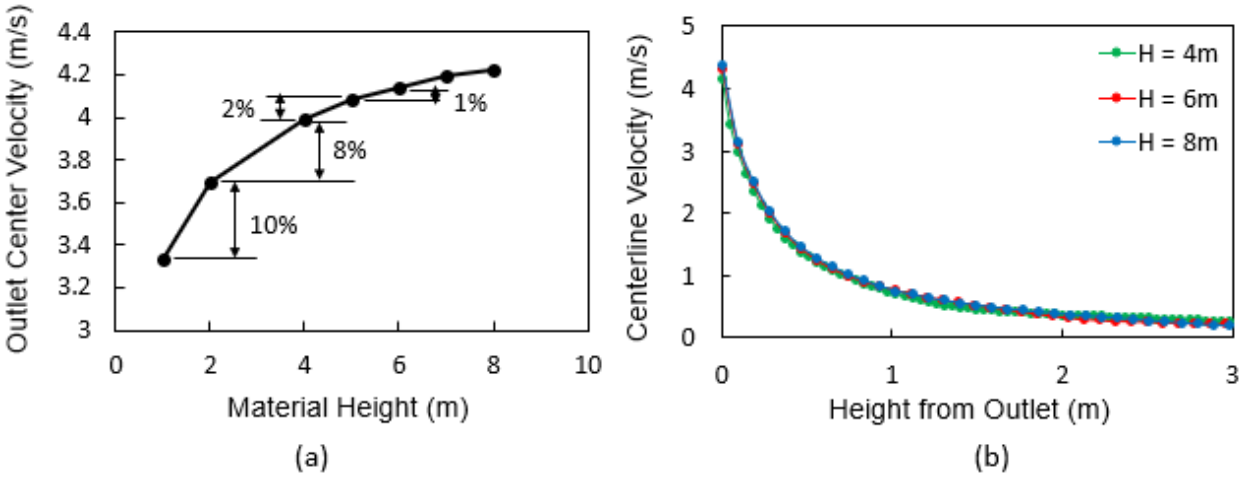

Figure 4.8. Height independence of (a) outlet center node velocity, (b) centerline velocity distribution.

As seen from Figure 4.9a, even if the magnitude of the peak wall normal stress increases with material height, the overall trend remains the same. The normalized stress profiles (normalization with respect to the peak value) collapse onto each other (Figure 4.9b).

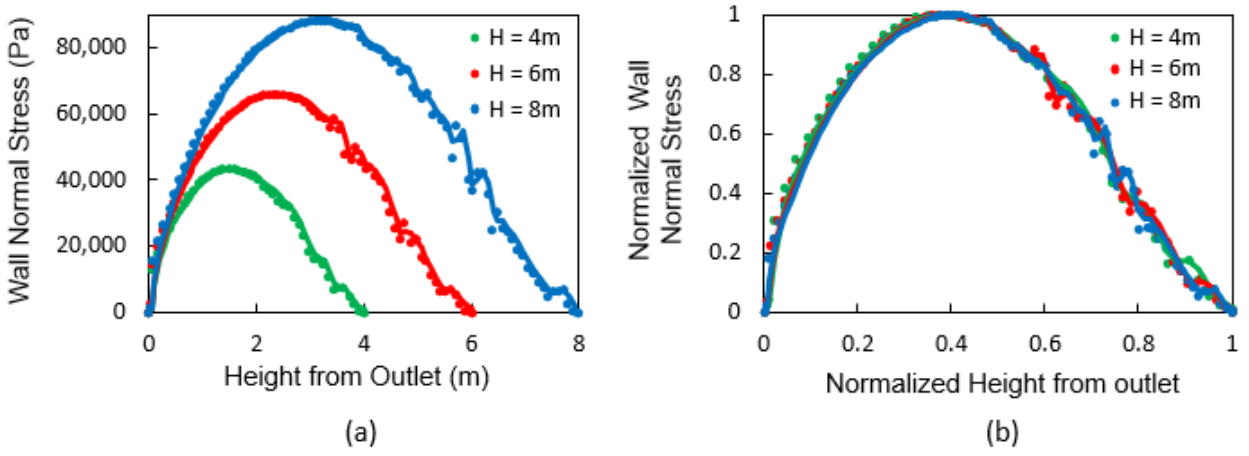

Figure 4.9. (a) Actual and (b) normalized wall normal stress distribution for increasing material height.

4.5.3 Equivalence of the Mohr-Coulomb and Drucker-Prager Model

FEM results are obtained based on the Drucker-Prager model after converting the Mohr-Coulomb parameters using Eq. (3.2). Figure 4.10 shows the equivalence between these two models in terms of the filling and discharging wall normal stresses.

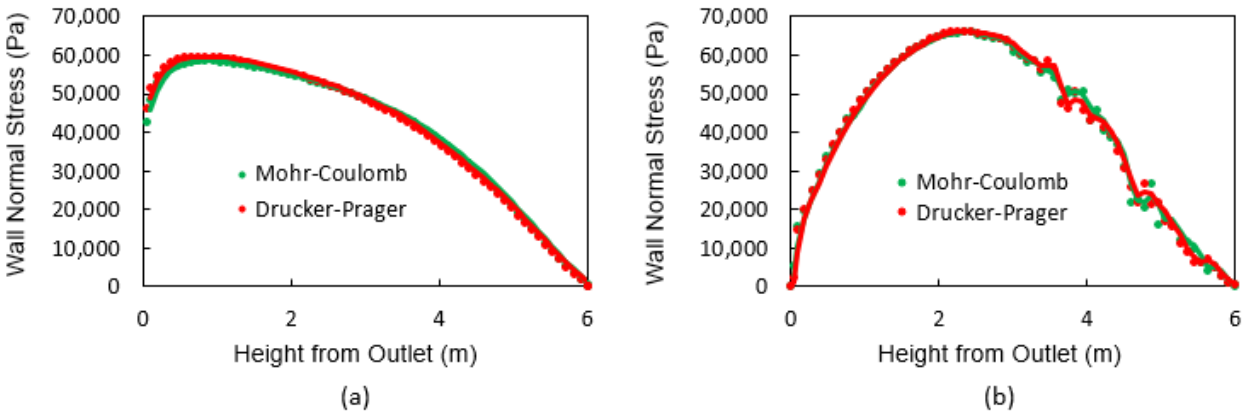

Figure 4.10. Equivalence of the Mohr-Coulomb and Drucker-Prager models in terms of (a) filling and (b) discharging wall normal stress.

Figure 4.11 shows the equivalence in terms of the outlet velocity distribution and the mass discharge rate. Note that in very long simulations, the mass discharge rate predicted from the Mohr-Coulomb model will be smaller than that of the Drucker-Prager model, as the minimum dilation angle allowed in the Mohr-Coulomb model is 0.1^{o}, which causes the bulk density near the hopper outlet to keep reducing with time.

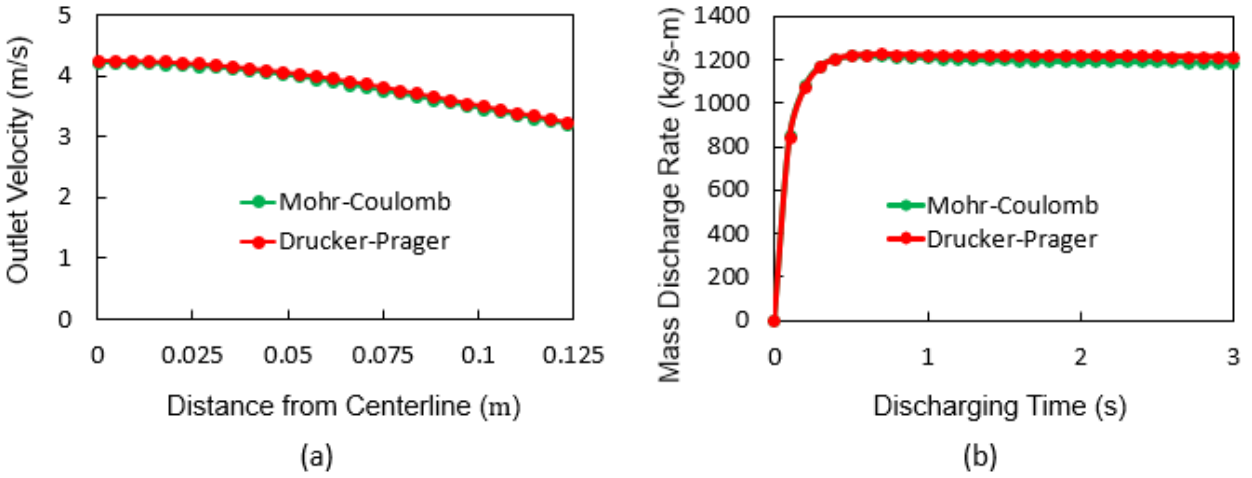

Figure 4.11. Equivalence of the Mohr-Coulomb and Drucker-Prager models in terms of (a) outlet velocity distribution and (b) mass discharge rate variation.

4.5.4 Wall Normal Stress Comparison to Analytical Theory

Since numerous experiments [20,37,46] indicate that experimentally measured wall stresses match closely with the modified Walker's theory, the FEM wall normal stress results are compared with this theory. Figure 4.12 shows the filling and discharging wall normal stress comparison with the modified walker's theory for material properties and hopper geometry in Table 4.2.

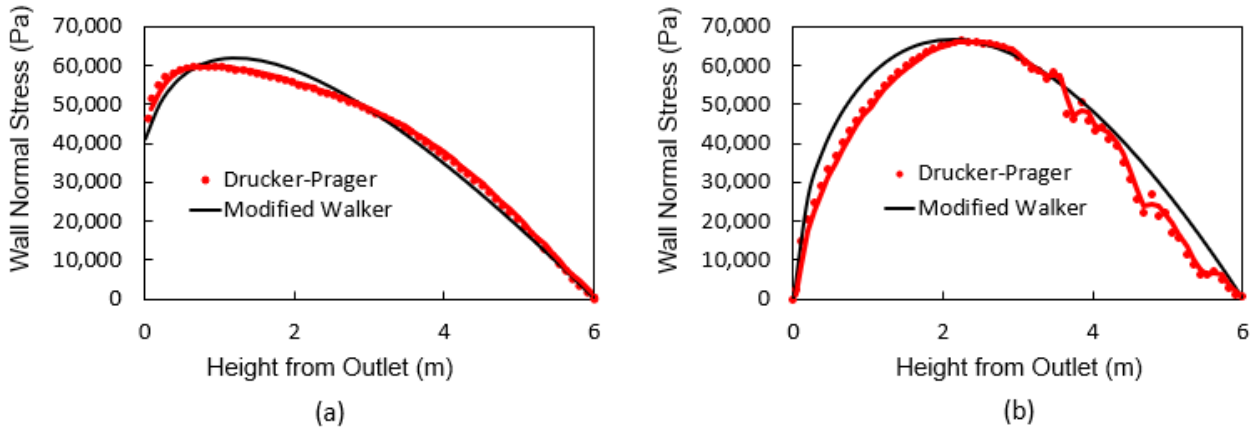

Figure 4.12. (a) Filling and (b) discharging wall normal stress compared to modified Walker's theory.

4.5.5 Velocity Comparison to Kinematic Model

The experimental velocity profile has been found to be qualitatively agree with the profile predicted by a kinematic model for a 2D converging hopper geometry [19,20]. Therefore, the vertical velocity component of the FEM simulations is compared to the kinematic model. This model is presented in chapter 1. The final equation is reproduced here,

$$v(x,y) = v_{\text{centerline}}(y = h)e^{-x^2/4Dy}. \tag{4.4}$$

Figure 4.13 shows the velocity comparison at different heights for the converging hopper geometry of Table 4.2. The FEM velocity profiles compare well to the kinematic model. The magnitude of diffusion length D is observed to increase with height similar to the experimental observations [19].

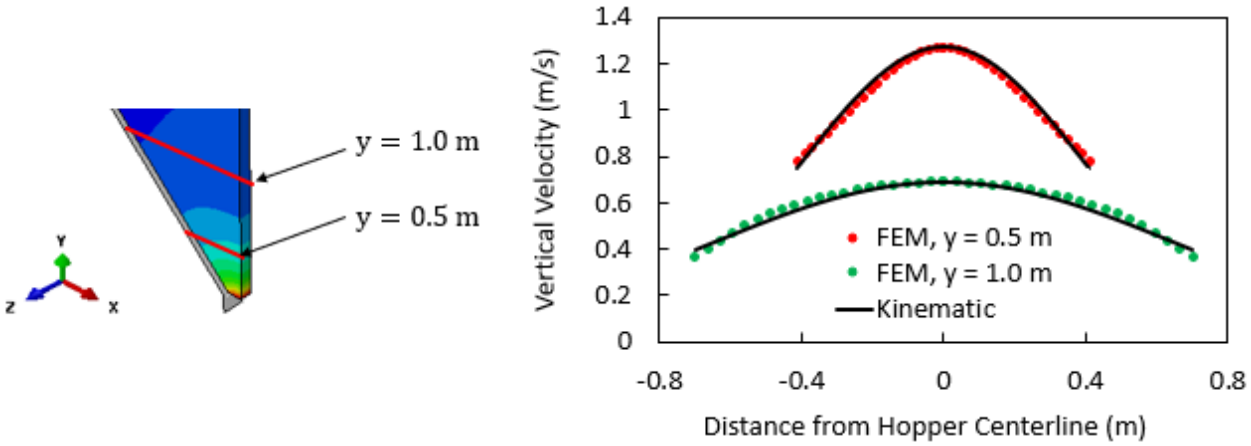

Figure 4.13. Simulation velocity profile comparison with the kinematic model.

4.5.6 Mass Discharge Rate Comparison to Correlations

The dilation angle has been observed to affect the hopper mass discharge rate significantly. Figure 4.14 shows the comparison of the average density at the hopper outlet and mass discharge rate for two cases. Comparison is shown when a constant dilation angle of 10^{o} is used and when a linear reduction in the dilation angle is implemented. Use of constant non-zero dilation angle results in unrealistic continuous reduction of the mass discharge rate. Whereas, linearly reduced dilation angle agrees with experimental observations of steady mass discharge rate during hopper discharge of cohesionless particulate materials.

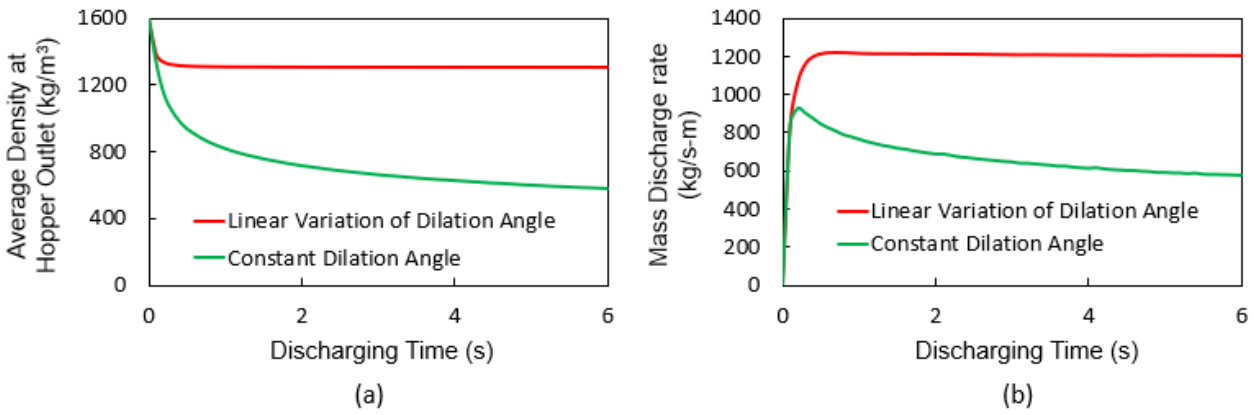

Figure 4.14. Effect of dilation angle on (a) average density at outlet and (b) mass discharge rate.

As mentioned in chapter 1, Beverloo [21] proposed a correlation for steady mass discharge rate (Eq. (1.4)). This empirical correlation was found to agree well with experimental mass discharge rate data for the case of flat-bottomed bin [16]. Rose and Tanaka [22], modified this correlation to include dependence on hopper half angle (Eq. (1.7)). This modified correlation can be represented as,

$$\dot{m}_{Rose\ Tanaka} \propto b^{3/2}(\tan\theta)^{-0.35}. \tag{4.5}$$

It can be observed from Figure 4.15 that FEM mass discharge rate shows similar dependence on hopper outlet width and hopper half angle, thus conforming experimental observations.

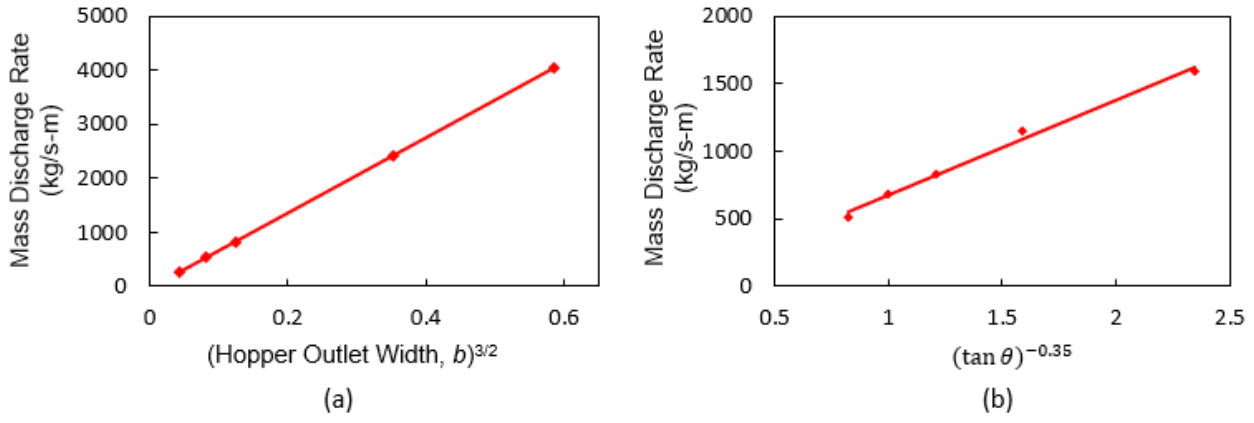

Figure 4.15. FEM hopper mass discharge rate dependence on (a) outlet width and (b) hopper half angle.

4.5.7 Hopper Flow Mode Comparison to Jenike's Chart

Flow of particulate material through the hopper is characterized as a mass flow, if all of the material from the hopper starts discharging simultaneously without any stagnant zones. On the other hand, if there is some stagnant material along the hopper walls and material near hopper centerline discharges much faster than the material near wall, this flow is characterized as funnel flow. Jenike's chart [2] (Figure 4.16) is often used to predict the hopper flow mode. This chart indicates that hopper flow mode can change if either the hopper half angle, material internal friction angle, or wall friction angle is changed. Original Jenike's chart was based on the existence of the radial stress field as a criterion for mass flow mode [16]. Funnel flow occurs if there are no solutions to the governing equations of radial stress theory. Afterwards, this chart was modified based on experimental investigations [3].

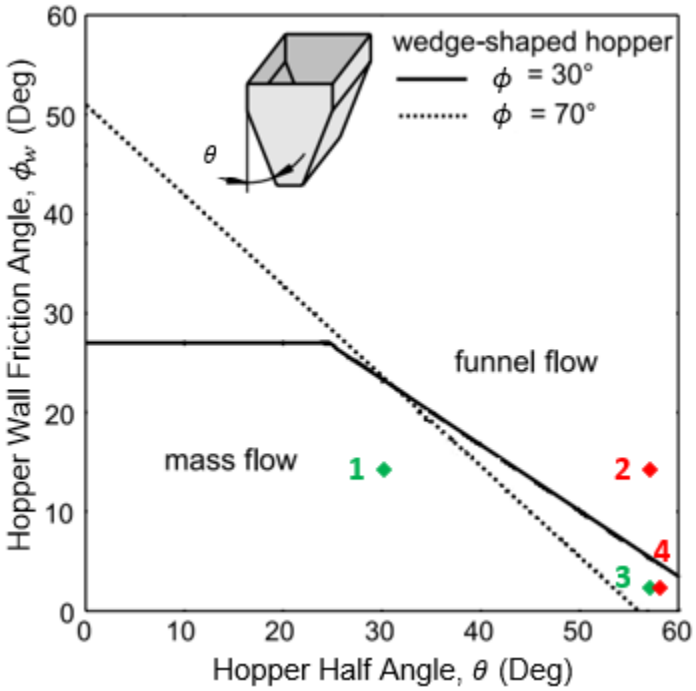

Figure 4.16. Jenike's chart for wedge shaped hopper.

For FEM hopper flow analyzed here, the mass flow index criterion is used to distinguish between hopper flow modes. Mass flow index is a ratio of average material velocity along hopper wall to average material velocity along hopper centerline, $MFI = \frac{\overline{V_{wall}}}{\overline{V_o}}$. If the mass flow index is greater than 0.3, the flow is characterized as mass flow and funnel flow will occur if the mass flow

index is less than 0.3. Ketterhagen et al. [72] used this criterion for DEM based hopper flow simulations and demonstrated good agreement with Jenike's chart. Distinction based on the mass flow index criterion is made for four FEM simulations on Jenike's chart as shown in Figure 4.16. These four points demonstrate the capability of FEM analysis to predict hopper flow mode, as each of the three parameters influencing the hopper flow mode are varied while keeping other two parameters constant. It can be observed from Table 4.4 that FEM flow mode prediction based on the mass flow index criterion agrees well with Jenike's chart.

Table 4.4. Hopper flow mode prediction based on the mass flow index criterion

Point on Chart	MFI	Flow Mode
1	0.556	Mass
2	0.173	Funnel
3	0.613	Mass
4	0.027	Funnel

4.5.8 Parametric Studies

Parametric studies are performed in this section to better understand the effects of elasto-plastic model parameters on the hopper flow characteristics. In total four parameters are examined: material elasticity modulus (E), internal friction angle (ϕ), wall friction angle (ϕ_w), and constant volume solid fraction (η_{cv}). These parameters are varied from a base case for which the internal friction angle (ϕ) is 25^o and wall friction angle (ϕ_w) is 15^o. All other properties are the same as in Table 4.2. The corresponding effects on wall normal stresses, velocity profile, and mass flow rate are investigated.

Effect of Elasticity Modulus

Experiments report a sharp peak in the wall normal stress as material suddenly starts discharging through the hopper system [20,46]. Similar sharp peak is observed in the FEM simulations. Figure 4.17a shows the temporal variation of wall normal stress for a mesh element located in the middle portion of the hopper (Figure 4.17b). This sharp peak and subsequent oscillations are expected in FEM based on the explicit time integration scheme. The force

equilibrium equation is not exactly satisfied in an explicit scheme and therefore the stresses oscillate. For a stable explicit scheme, it is expected that the oscillations damp out and equilibrium is eventually achieved.

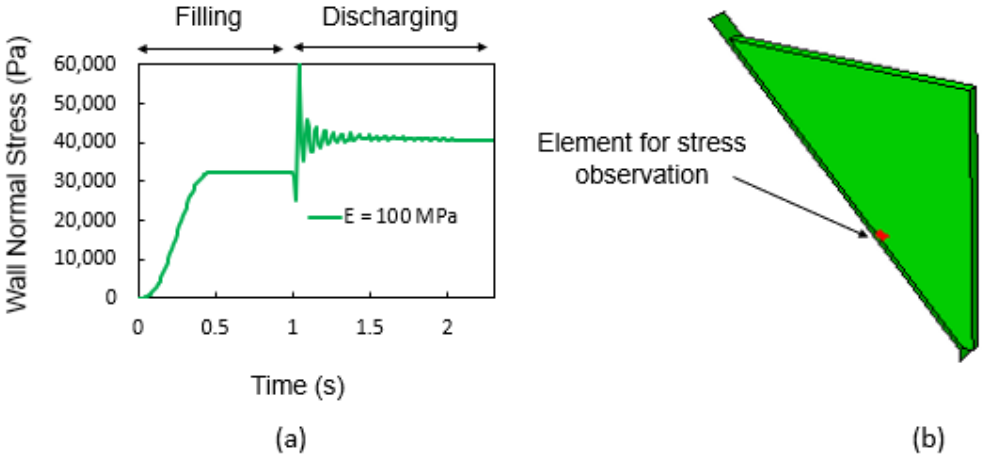

Figure 4.17. Simulation wall normal stress peak.

It should be noted that with decreasing elasticity modulus, the default stable time increment of Abaqus increases and it takes longer for the oscillations to damp out (Figure 4.18). If the elasticity modulus value is too small, required settling time for the material filling stage is longer because the oscillations take longer time to damp out completely (Figure 4.18). Similar oscillations are also observed in experiments, but they damp out rapidly. Ideally, the elasticity modulus value measured from an uniaxial confined loading/unloading experiment on the bulk particulate material should be used [62].

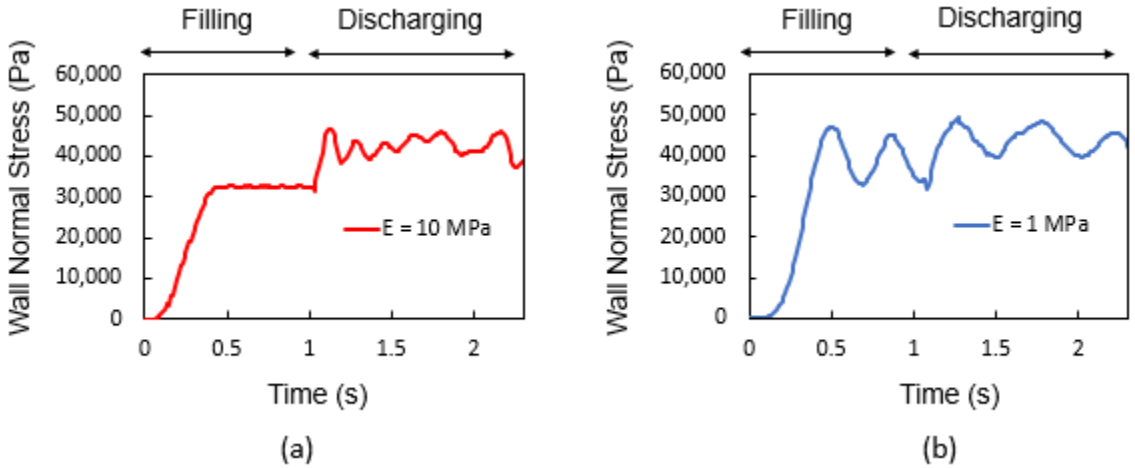

Figure 4.18. Effect of decreasing elasticity modulus.

Effect of Internal Friction Angle

Although the magnitude of the hopper outlet velocity decreases with an increasing internal friction angle, the overall profile remains the same as observed from a comparison of outlet velocity distribution (Figure 4.19a). With increasing internal friction angle, the position of the peak wall normal stress shifts higher up the hopper as seen from simulation results (Figure 4.19b).

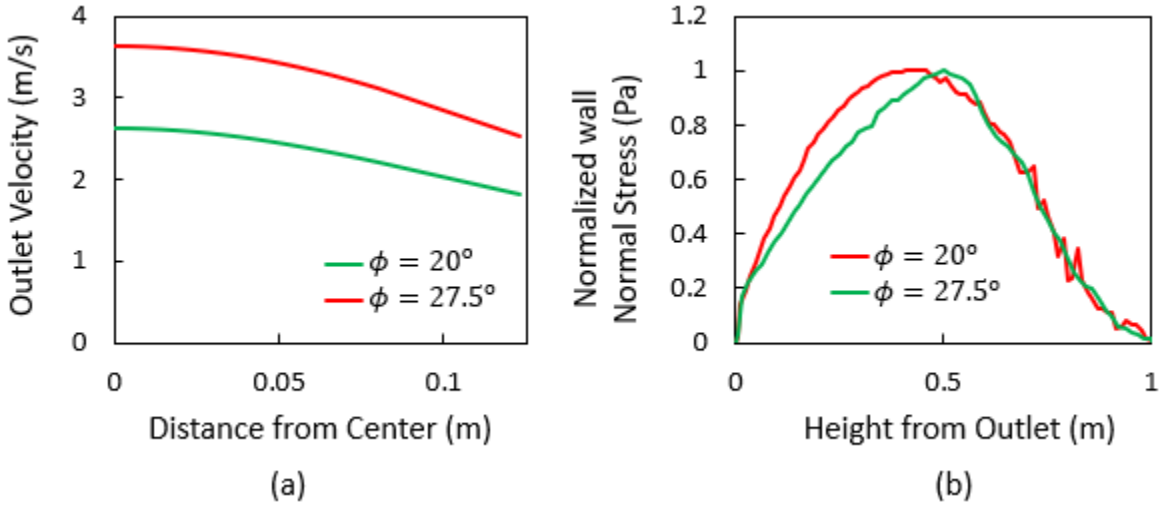

Figure 4.19. Effect of increasing internal friction angle on (a) outlet velocity and (b) normalized wall normal stress.

Since, the solid fraction at which the dilation angle goes to zero does not change, the corresponding bulk density near the hopper outlet is the same as the base case, which causes the steady mass discharge rate to decrease (Figure 4.20).

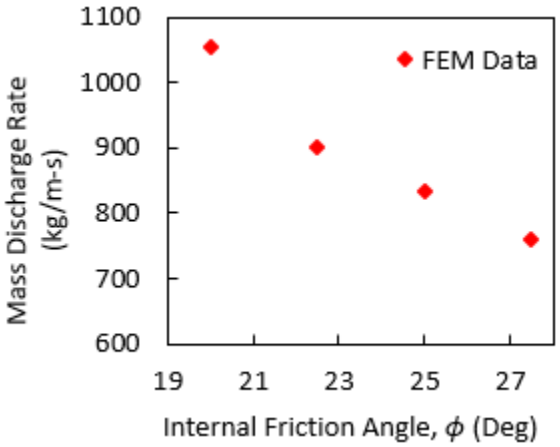

Figure 4.20. Mass discharge rate variation with internal friction angle.

Effect of Wall Friction Angle

It can be observed from Figure 4.21 that with increasing wall friction angle, wall normal stress peak shifts towards the top of the hopper and symmetry around this peak reduces. Increasing wall friction angle causes increase in the wall shear stress which essentially slows the material near it, causing increase in the concavity of velocity profile as observed in Figure 4.22. Increasing concavity in outlet velocity distribution reduces the average outlet velocity thus the mass discharge rate decreases (Figure 4.23).

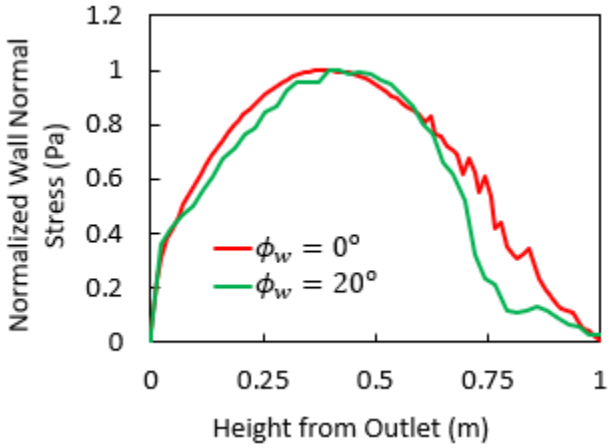

Figure 4.21. Wall normal stress for increasing wall friction angle.

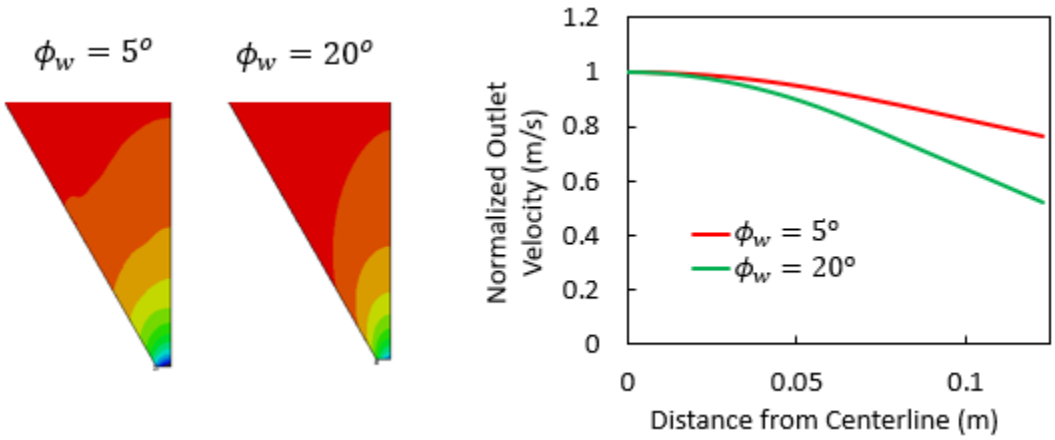

Figure 4.22. Velocity profile for increasing wall friction angle.

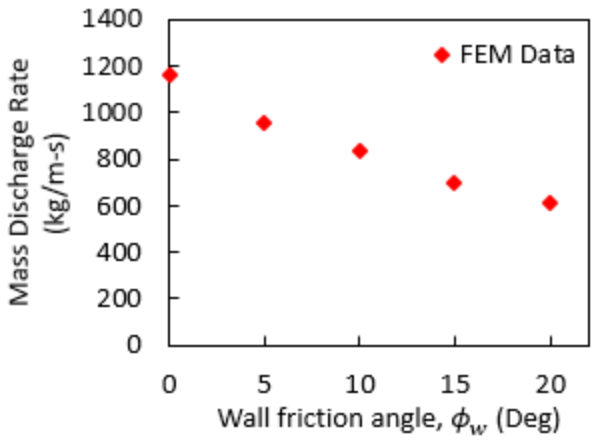

Figure 4.23. Mass discharge rate variation with wall friction angle.

Effect of Constant Volume Solid Fraction

Varying constant volume solid fraction for which the dilation angle reduces to zero, changes the bulk density near the hopper outlet. Increasing constant volume solid fraction has no effect on the outlet velocity distribution but has some effect on the diffusion of velocity through the hopper. If constant volume solid fraction is large, material near the hopper outlet reaches constant volume state quickly and material in upper section of the hopper starts moving. Thus, causing more diffusion of velocity profile. Whereas, for small values of constant volume solid fraction, material near the hopper outlet can dilate for a longer time before material in the upper hopper section starts moving (Figure 4.24).

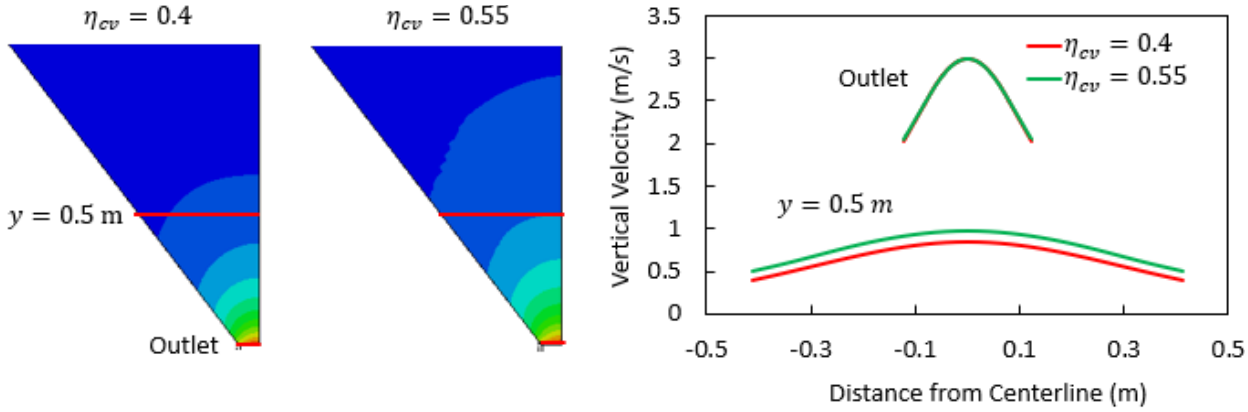

Figure 4.24. Velocity profile for increasing constant volume solid fraction.

5. QUANTITATIVE COMPARISON OF HOPPER FLOW CHARACTERISTICS

Based on the literature review on FEM hopper studies of cohesionless particulate materials presented in chapter 2, it is clear that there is a need to conduct a thorough quantitative validation study of different FEM hopper flow characteristics.

The present work aims to provide a one-to-one quantitative comparison of FEM and experimental flow characteristics for same bin geometry. This work is inspired by the experiments of Maiti et al. [53], where particle image velocimetry (PIV) was used to measure the velocity profiles of sand discharging through quasi two-dimensional, flat-bottomed bins with centered (concentric) and off-center (eccentric) exits. A detailed comparison to Maiti et al.'s work was not possible due to unavailability of some of the model parameters as well as some concern regarding the influence of sand particles sticking to the bin walls. Therefore, PIV experiments on similar laboratory-scale bins were conducted in the present work. After measuring Mohr-Coulomb constitutive law material properties, an Eulerian FEM analysis, implemented in Abaqus/Explicit, was implemented to simulate the complete discharge process. A quantitative comparison of four different hopper flow characteristics: the velocity profiles, the MDR, the duration of steady MDR (T_{SS}), and the free surface profile contours are presented. Comparisons are made for concentric as well as eccentric bins to thoroughly assess the accuracy of the Mohr-Coulomb FEM model.

5.1 Bin Design and Experimental Setup

The present experimental setup is inspired by the work of Maiti et al. [53], but with slight modifications. The geometry consisted of a quasi two-dimensional, flat bottomed-bin with an exit that could be positioned at different locations at the base of the bin (Figure 5.1). In order to reduce the tendency of particles sticking to the hopper walls due to electrostatic effects, which has the potential of interfering with PIV measurements, the bin walls were made of tempered glass. Detailed views and dimensions of the hopper are shown in Figure 5.1b. The size and position of the hopper outlet could be adjusted by changing the position of two bottom sliders. Although the width of the outlet opening could be varied, it was kept fixed at 11.8 mm throughout this work. The exit location was either at the center of the bin (the concentric case) or all the way to one side

(the eccentric case). Figure 5.2 shows the images captured by the high-speed camera at an instant during the discharge process for the concentric (Figure 5.2a) and eccentric (Figure 5.2b) bins.

The particulate material used in the experiment was ASTM C778 standard 20-30 sand with a mean particle diameter ($d_{particle}$) of 710 μm [73,74]. The bulk material properties required for the implemented FEM constitutive model along with the sand-glass wall friction coefficient are discussed in Section 5.3.

A weighing scale was placed directly below the bin outlet to collect the discharged sand and, thus, measure the mass discharge rate (MDR). A high-speed camera (Photron Fastcam) was used to record the discharging flow through the front glass wall of the bin. Details of the camera and PIV settings are provided in Section 5.2. Black curtains were used to remove reflections on the glass walls that could adversely affect the PIV measurements. The velocity and free surface profiles were obtained from the camera recordings and PIV analysis while the MDR and the duration of steady MDR (T_{SS}) were determined based on the weighing-scale data. Unless specified, the term "velocity profile" refers specifically to the vertical component of velocity (v) for the particles near the front bin wall. These velocity profiles were obtained along horizontal paths at various heights from the bin outlet.

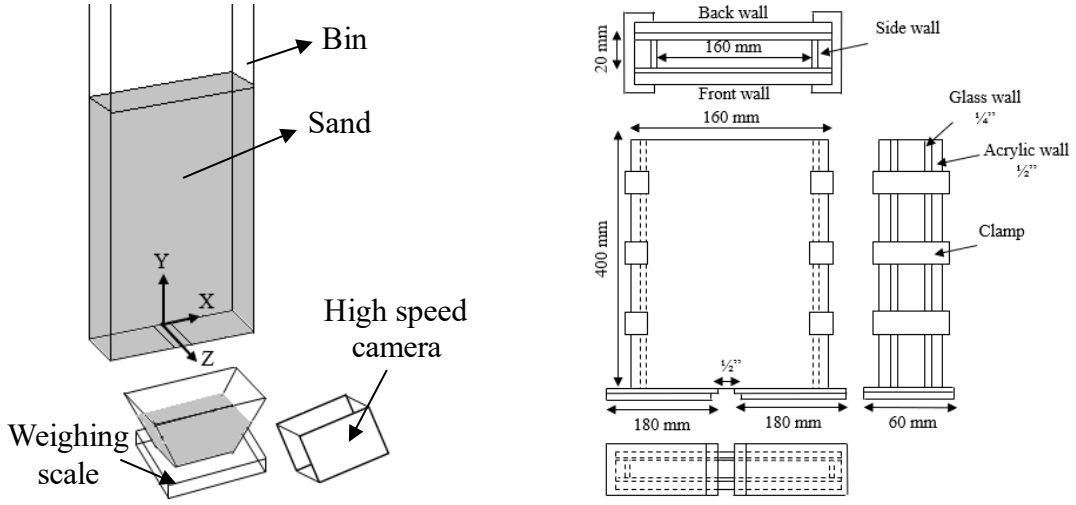

Figure 5.1. (a) Schematics of the experimental setup. (b) Detailed bin views and dimensions (not to scale).

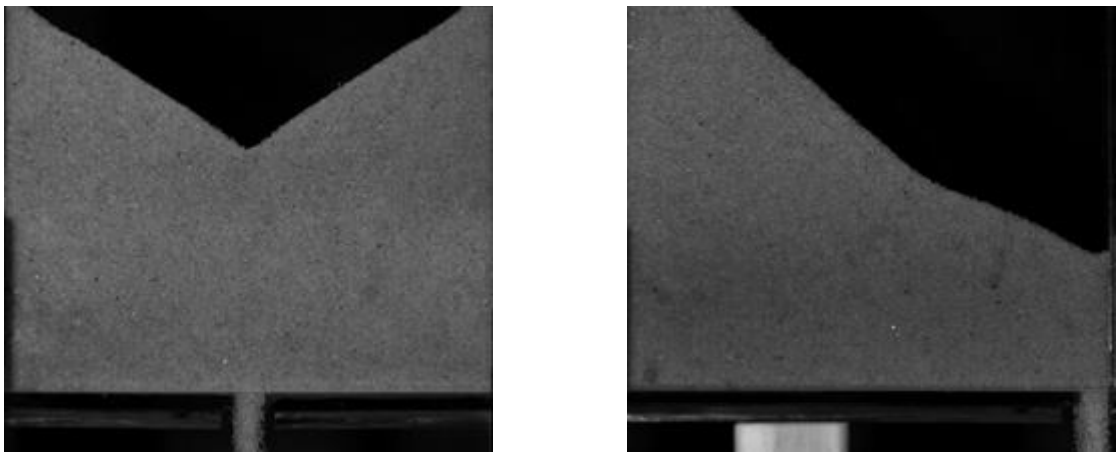

(a) **(b)**

Figure 5.2. Images during discharge for (a) concentric and (b) eccentric bin.

After assembling the bin and closing the outlet, sand was poured into the bin from the top opening through a small funnel. While filling, it was ensured that the material free surface remained approximately horizontal. After achieving a desired initial material height of about 200 mm, both the outlet stopper was removed and the high-speed camera recording was started at approximately the same time. The weighing scale was set to output the weight of its contents at 1 s intervals.

5.2 High Speed Camera and PIV Settings

The high-speed camera was positioned such that the complete bin length was captured by the camera's square field of view with the maximum possible resolution setting of 1024 X 1024 px. Hence, the spatial resolution of the captured images was 0.168 mm/px or 4.3 $\mathrm{px/d_{particle}}$. The camera frame rate was chosen such that the PIV random error observed in extracted velocity profiles was minimized. Table 5.1 shows the frame rates used to obtain the velocity profiles. The camera shutter speed of 1/6000 s was found to be good enough to avoid motion blur. The aperture opening and camera focus was adjusted to capture the 2D flow of sand particles in the vicinity of the front bin wall.

Table 5.1. Camera frame rate used in the experiments

Height from outlet	**Frame rate**	
	Concentric bin	Eccentric bin
≤ 10 mm	250 FPS	500 FPS
> 10 mm	125 FPS	250 FPS

Particle Image Velocimetry (PIV) has been implemented by many researchers to capture the flow of granular materials [19,46,75]. Based on the guidelines provided by Sarno et al. [76] for granular PIV (g-PIV) experiments, the open source MATLAB program PIVLab [77] was used in this work to extract the velocity profiles from the camera recordings. The window deformation technique of PIVLab is useful for capturing the shear deformation of dense granular flows and minimizing gradient bias errors. The multi-pass interrogation window (IW) feature can be used to achieve a desired spatial refinement while avoiding loss-of-pairs errors. For detailed explanation of these PIV techniques, please refer to Sarno et al. [76] and PIVLab [77].

Based on the work of Sarno et al. [78] for the case of a chute flow of Ottawa sand, it was determined that the natural contrast of the sand due to its sub-grain structure was good enough for capturing the velocity profiles through PIV analysis and additional colored particles were unnecessary. Sarno et al. [76] concluded that for g-PIV applications, a nine point window deformation algorithm with bilinear interpolation, 50% overlap of IW, quadruple IW pass technique, and 2 X 3 sub-pixel Gaussian interpolation produces accurate results. A smaller number of IW passes may underestimate the velocity magnitude. The IW size for the first pass was given by,

$$IW_1 \geq Max\ (4d_{particle}, 4u_{max}), \tag{5.1}$$

where u_{max} is the maximum displacement expected during the discharge. The parameter u_{max} for the current work was determined as,

$$u_{max} = (MDR/(\rho_{outlet} A_{outlet}))\Delta t, \tag{5.2}$$

Here, the mass discharge rate was obtained through weighing scale data and ρ_{outlet} was the material bulk density near the outlet, which was assumed to be ~ 1387 kg/m^3 based on the constant-volume cubic lattice packing of spherical particles. The quantity Δt was obtained from the frame rate of the video recording.

According to Sarno et al. [76], the IW size for the last pass should be less than or equal to $d_{particle}$. In the present work, due to low resolution of the obtained images (resulting from the requirement to capture the complete bin length), the size of the fourth IW pass is small in terms of the number of pixels. It was observed that for such a small IW size, PIVLab generates unrealistic non-zero velocities for stagnant material. Therefore, a maximum of three IW passes are used in this work. Table 5.2 shows the IW size of each pass.

Table 5.2. Interrogation window (IW) size for each pass

Interrogation window pass	**Interrogation window size**
First	20 *X* 20 px or 4.5 X 4.5 $d_{particle}$
Second	12 *X* 12 px or 2.7 X 2.7 $d_{particle}$
Third	8 *X* 8 px or 1.6 X 1.6 $d_{particle}$
Fourth*	4 *X* 4 px or 1 X 1 $d_{particle}$

* Fourth pass generates unrealistic velocities due to a small IW size.

It was observed that the velocity profiles obtained through the triple IW pass technique contained significant PIV noise. This noise was due to using an IW size that was too small, in terms of pixels, in the third pass, which increased the random errors associated with the PIV analysis [79]. Hence, the double IW pass technique was used subsequently in this work.

It was observed that at a given height from the outlet, the velocity profile remained steady for some period of time before changing as the free surface approached that height. Figure 5.3 shows the velocity profiles obtained along two horizontal paths at two different heights for both bins at 1 s intervals, the origin of the x-coordinate is located at the outlet center. It can be observed that for the concentric bin, the velocity profile at H = 10 mm remains similar from 1 to 7 s of discharge whereas at H = 70 mm, the velocity profile is similar only for 2 and 3 s. Similarly, for an eccentric bin, the velocity profile remains steady from 1 to 4 s at H = 10 mm but at H = 70 mm, the velocity profile is similar only for 1 and 2 s after the discharge. Therefore, the steady state velocity profiles are calculated by averaging over the observed steady sate period at each height.

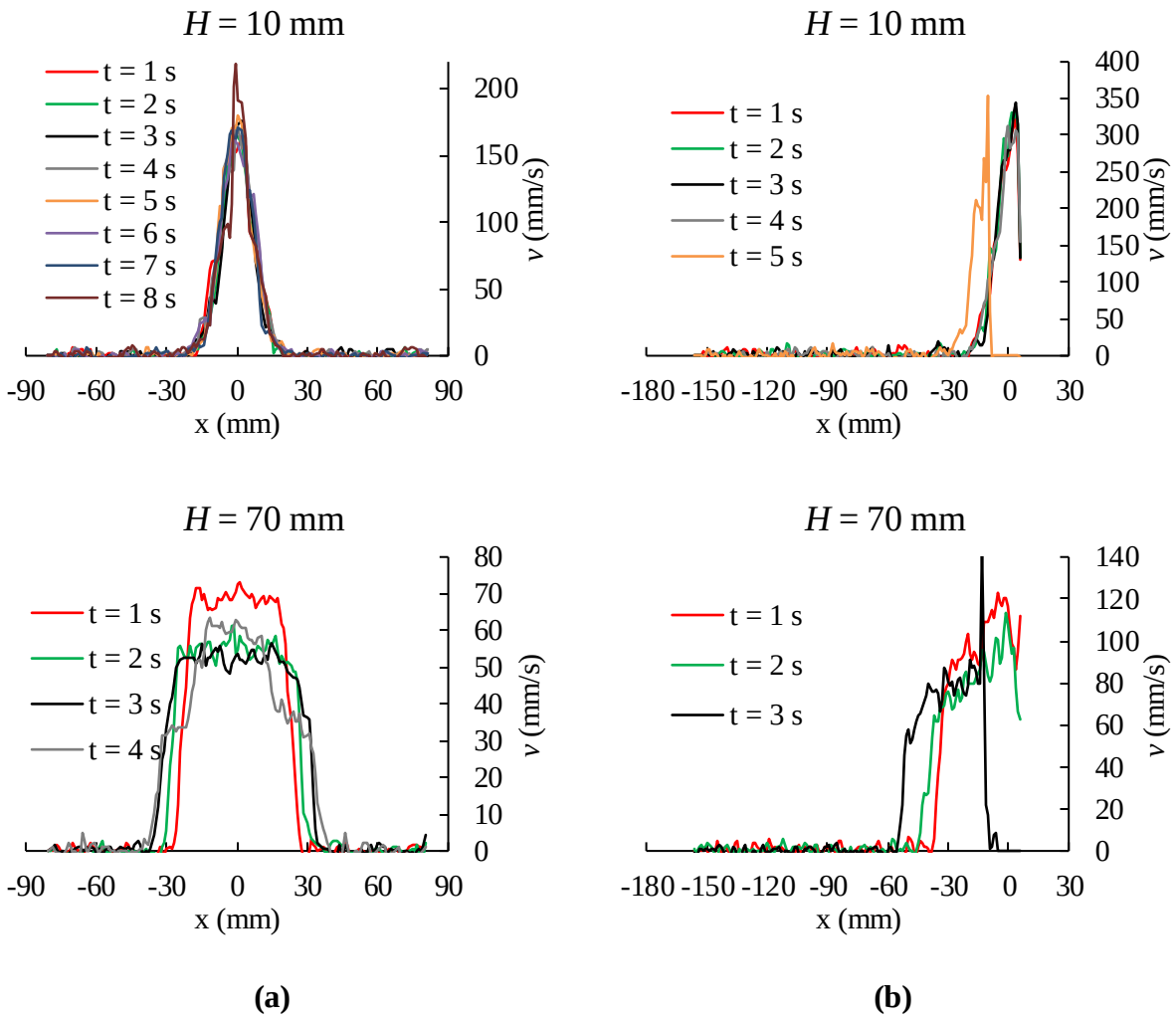

Figure 5.3. Time variation of velocity profiles for (a) concentric and (b) eccentric bins at different heights (H) above the bin outlet.

The accuracy of the obtained steady state PIV velocity profiles was analyzed by calculating the average flowing density at that height by,

$$\rho_{Flow}^{Average} = (\dot{m}/(\Sigma v \Delta x W)), \tag{5.3}$$

where, the summation is done over all the data points along that height and Δx is the uniform spacing between these data points. The parameter W is the hopper width in the z direction (Figure 5.1a). It was observed that $\rho_{Flow}^{Average}$ for all H > 10 mm was less than the initial filling density, as expected. However, at H = 10 mm, $\rho_{Flow}^{Average}$ was larger than the initial filling density, implying that the velocity magnitude at H = 10 mm was underpredicted. To obtain more accurate velocity

profiles at H = 10 mm, experiments were conducted with the camera capturing only half of the bin length to increase the image resolution (0.033 mm/px or 8.6 px/$d_{particle}$). The velocity profiles from these higher resolution images were then obtained by using three IW passes. As seen from Figure 5.4, the velocity profiles produced by the low resolution images are underpredicted at H = 10 mm, but are reasonably accurate at larger heights for the concentric bin. In contrast, the low resolution images produced accurate velocity profiles even at H = 10 mm for the eccentric bin, mostly due to the larger frame rate used to record the eccentric bin discharge.

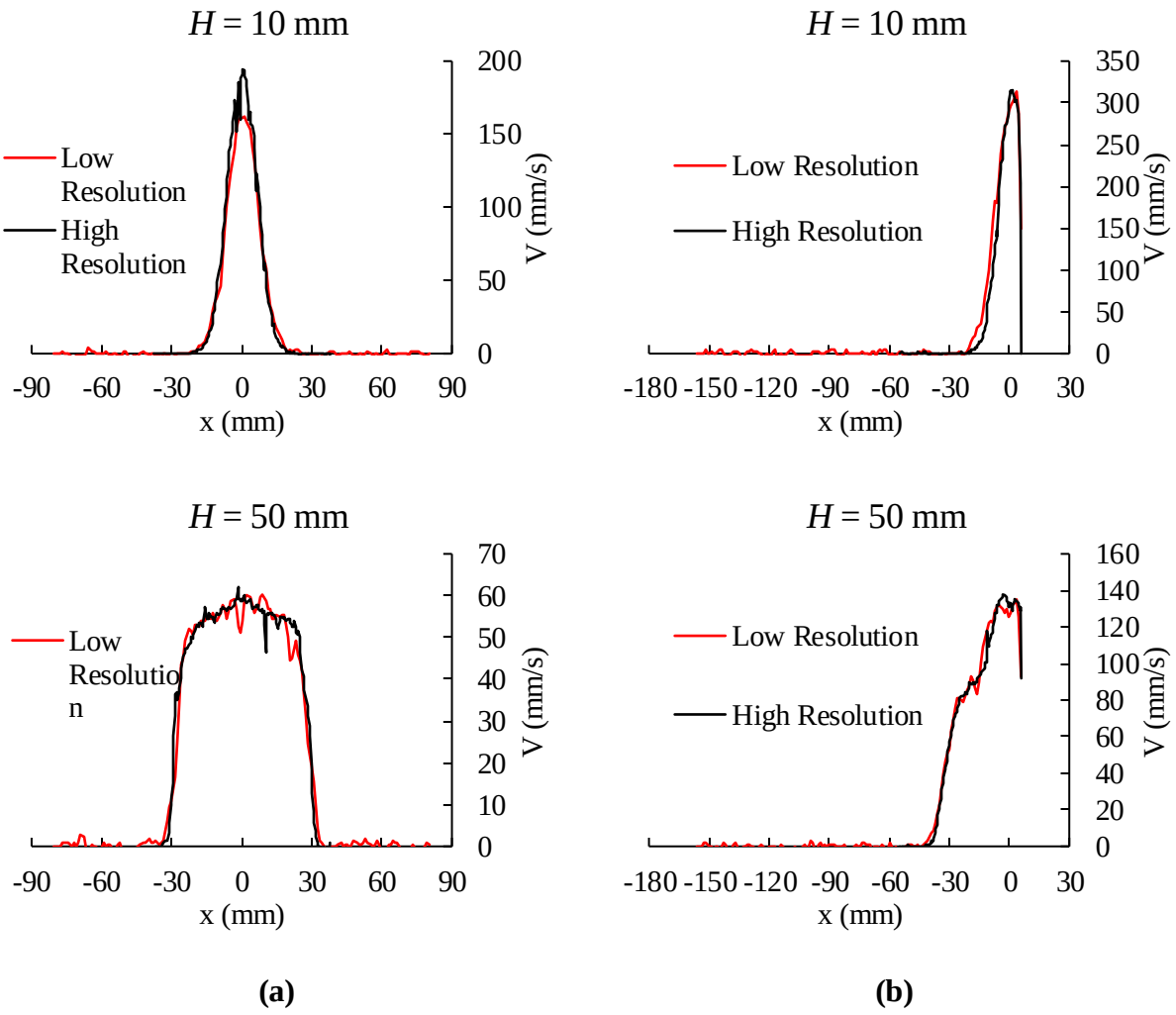

Figure 5.4. Effect of image resolution on the velocity profiles for (a) concentric and (b) eccentric bins.

5.3 FEM Simulation Setup

Similar to previous FEM hopper studies [38,39,41], this work implemented the Eulerian analysis technique of Abaqus/6.14-6 [49] to avoid excessive distortion of mesh elements during the discharge process. Figure 5.5 shows the simulation setup using a coarse mesh for concentric (Figure 5.5a) and eccentric bins (Figure 5.5b). An Eulerian material outflow boundary condition at the bin outlet and a void inflow boundary condition at the bin top surface ensured that material discharged freely through the outlet and no new material entered the simulation domain. Only one-quarter of the concentric bin was simulated by assigning appropriate symmetry boundary conditions as shown in Figure 5.5a. Half of the eccentric bin was simulated as shown in Figure 5.5b. The bin side and front walls were modeled as rigid bodies and a Coulomb frictional interaction exists between the Eulerian material and the wall surfaces. Dimensions of the FEM bin and initial material height were the same as the experimental trials.

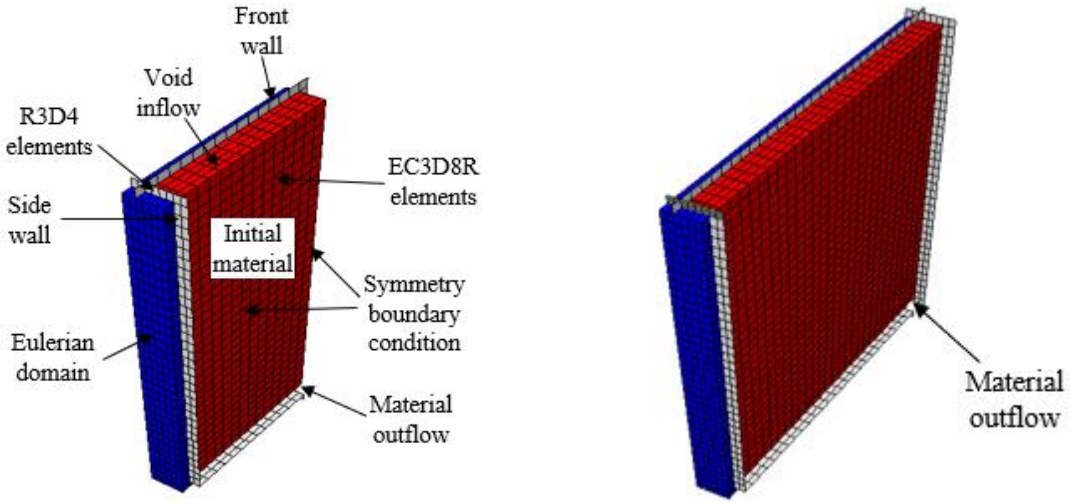

Figure 5.5. Eulerian FEM simulation setup for (a) concentric and (b) eccentric bins.

The Eulerian simulation domain is meshed with eight node 3D hexahedral Eulerian elements (EC3D8R) with reduced integration technique and hour glass control to avoid volumetric locking [49]. The side and front bin walls are discretized with four node rigid quadrilateral (R3D4) mesh elements.

The material is modeled using the Mohr-Coulomb elasto-plastic constitutive model without regularization techniques. The usefulness of simple elasto-plastic constitutive models such as the

Mohr-Coulomb and the linear Drucker-Prager model in predicting hopper discharge flow characteristics has been demonstrated in previous FEM hopper studies [37–39,41] and chapter 4. The Mohr-Coulomb model was implemented in the present work to assess the applicability of such a simple constitutive model by performing one-to-one quantitative comparisons of different hopper flow characteristics.

The initial bulk density (ρ_i) of the material after filling was calculated by pouring a known mass of sand into the assembled hopper and measuring the filled material height. Based on 15 different trials, the mean ρ_i and corresponding 95% confidence interval was 1806.4 ± 8.5 kg/m^3. Therefore, in the FEM simulations, a ρ_i of 1800 kg/m^3 was assumed as shown in Table 5.3. The resulting initial packing fraction (η_i) of 0.68 was larger than the 0.64 value usually associated with the random close packing of hard spheres. This larger filled bulk density is thought to be due to the pouring procedure and the slight polydispersity of the sand particles.

The value of Poisson's ratio was assumed to be 0.3 based on properties reported for similar sand material [80]. The elasticity modulus was measured based on the initial unloading behavior of the bulk sand material measured through a uniaxial confined loading and unloading test. This procedure has been employed previously for bulk particulate materials [62]. It has been previously demonstrated that these elasticity properties have a negligible effect on FEM flow simulations [41].

Table 5.3. Parameter values used in the FEM simulations. The "NDNS" case refers to a no dilation, no softening model and the "DS" case refers to a model with dilation and softening.

	Parameter	**FEM NDNS**	**FEM DS**
Experimentally measured properties	Initial bulk density, ρ_i	1800 kg/m^3	
	Elasticity modulus, E	8 MPa	
	Constant-volume internal friction angle, ϕ_{cv}	34°	
	Wall friction angle, ϕ_w	7°	
Assumed properties	Poisson's ratio, υ	0.3	
	Maximum dilation angle, ψ_{max}	0°	15°
	Peak internal friction angle, ϕ_{peak}	–	46°
	Constant volume bulk density, ρ_{cv}	–	1387 kg/m^3

The constant-volume internal friction angle (ϕ_{cv}) and wall friction angle (ϕ_w) were measured using a Schulze annular ring shear test. The measured constant-volume internal friction

angle (ϕ_{cv}) value is consistent with values reported elsewhere in the literature for cohesionless sand [81–84].

It is well known that during shearing, a dense sample of cohesionless sand goes through a peak shear strength before eventually reaching the critical shear strength for a given normal stress. This critical strength of the sand is represented by the constant-volume internal friction angle (ϕ_{cv}). According to Bolton [59], the ϕ_{cv} value is independent of the stress level or initial density of the sample and, therefore, is constant for a given sand. However, the peak shear strength (ϕ_{peak}) is dependent on the maximum rate of dilation represented by, ψ_{max} during shearing. The ψ_{max} value varies based on how dense a given sample is. For Ottawa sand, it can be as large as 15^{o} [85].

For sand filled inside the bin, the stress varies with height. Hence, it can be speculated that the initial packing fraction, and therefore ψ_{max}, is also a function of height. As it is difficult to quantify the initial packing fraction of the filled sand, two extreme cases: a no dilation/no softening (NDNS) case and a with dilation and softening (DS) case, are considered in the present work. In the former case, the filled sand is assumed to already be in the constant-volume state with $\psi_{max} = 0^{o}$. For this unrealistic case of no dilation, there is no change in the bulk density. There is no material softening and the internal friction angle remains constant throughout the discharge.

In the DS case, the filled sand is assumed to be in a dense state and has $\psi_{max} = 15^{o}$. This dilation causes material softening, where the internal friction angle reduces from an initial peak value (ϕ_{peak}) to a constant-volume value (ϕ_{cv}). The peak internal friction angle is determined based on the empirical equation of Bolton [59] for quartz sand,

$$\phi_{peak} = \phi_{cv} + 0.8 * \psi_{max} = 46^{o}, \tag{5.4}$$

Although this equation is strictly valid for a plane strain system, it is a reasonable estimate for sand filled inside the present bin geometry due to the small wall friction and predominantly 2D flow observed in the camera recordings.

During discharge, this dense sand will dilate to a constant volume bulk density (ρ_{cv}), which is function of the discharging stress magnitude. Since this constant volume bulk density (ρ_{cv}) is difficult to measure for the near-zero stresses expected near the bin outlet and the free surface, an assumption is made based on the loose cubic lattice packing structure of flowing particles, resulting in $\rho_{cv} \approx 1387$ kg/m^3. It is expected that the experimental flow characteristics will lie between

these two extreme cases, depending on the magnitude of experimental dilation (ρ_{cv}^{Exp}) and corresponding softening.

The material dilation and softening for the DS case is implemented through a user-defined field variable that is set to be equal to the volumetric strain (Figure 5.6). Both the internal friction angle and dilation angle were assumed to decrease linearly with the volumetric strain from their initial peak values to the constant-volume values. The critical volumetric strain for which the material is assumed to reach a constant-volume state is calculated through Eq. (4.1) based on initial (η_i) and constant-volume (η_{cv}) solid fractions.

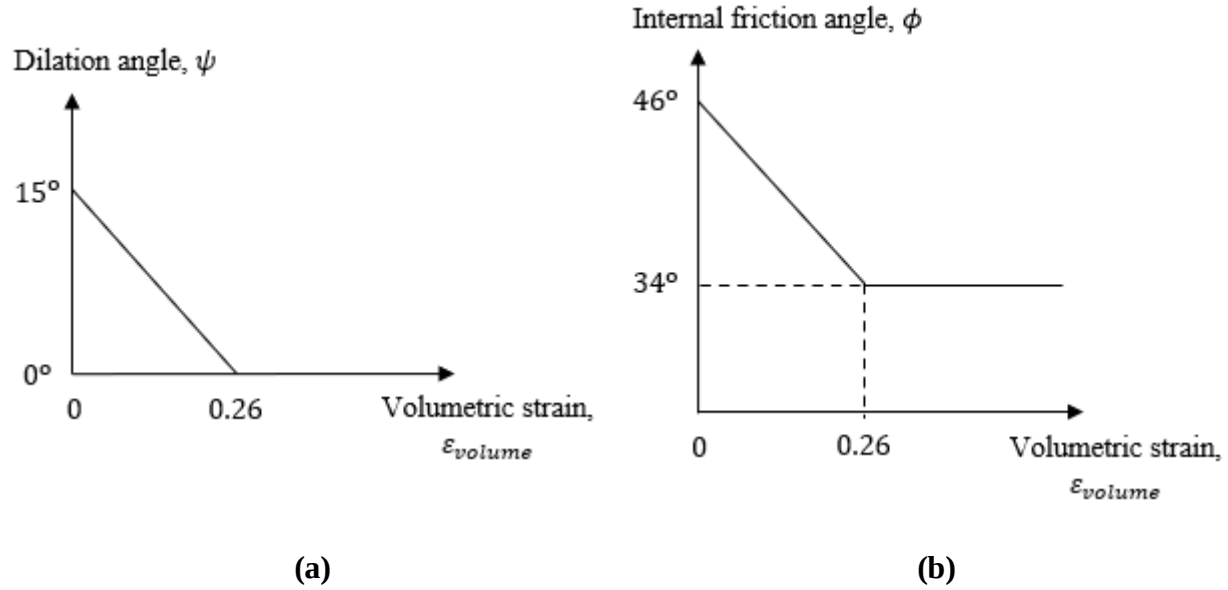

(a) **(b)**

Figure 5.6. Material dilation and softening through a linear reduction of (a) dilation angle and (b) internal friction angle with respect to the volumetric strain.

This linear reduction in the dilation and internal friction angles is an approximation to the actual nonlinear material softening observed in triaxial test experiments [66]. Similar linear material softening with respect to the shear strain was used previously by Anastasopoulos et al. [86] for finite element analysis of fault rupture propagation through sand.

Two dynamic simulation steps with explicit time integration scheme were used to simulate filling and discharging of the bin. During the filling step, a gravity body force was applied smoothly to the material. The material had a constant bulk density of 1800 kg/m^3 at the end of the filling step. In the second step, the outlet was opened and material was allowed to flow out of

the Eulerian domain. During this discharge, the dense material dilated and softened until the critical volumetric strain was reached.

5.4 Mesh Convergence Analysis

The effect of mesh density on the velocity profiles was investigated for each FEM simulation. An example of the mesh convergence analysis is shown in Figure 5.7a for the FEM NDNS case. It was concluded that a mesh density based on 10 cubical elements along the bin outlet (resulting in a total of approximately 150,000 elements for the eccentric bin) produced converged velocity profiles for both bins. The region of yielding mesh elements at a given time step for an eccentric bin is also shown in Figure 5.7b for different mesh densities. It can be observed that this region is dependent on the mesh density due to the absence of a regularization technique. However, the effect on the velocity profile is negligible.

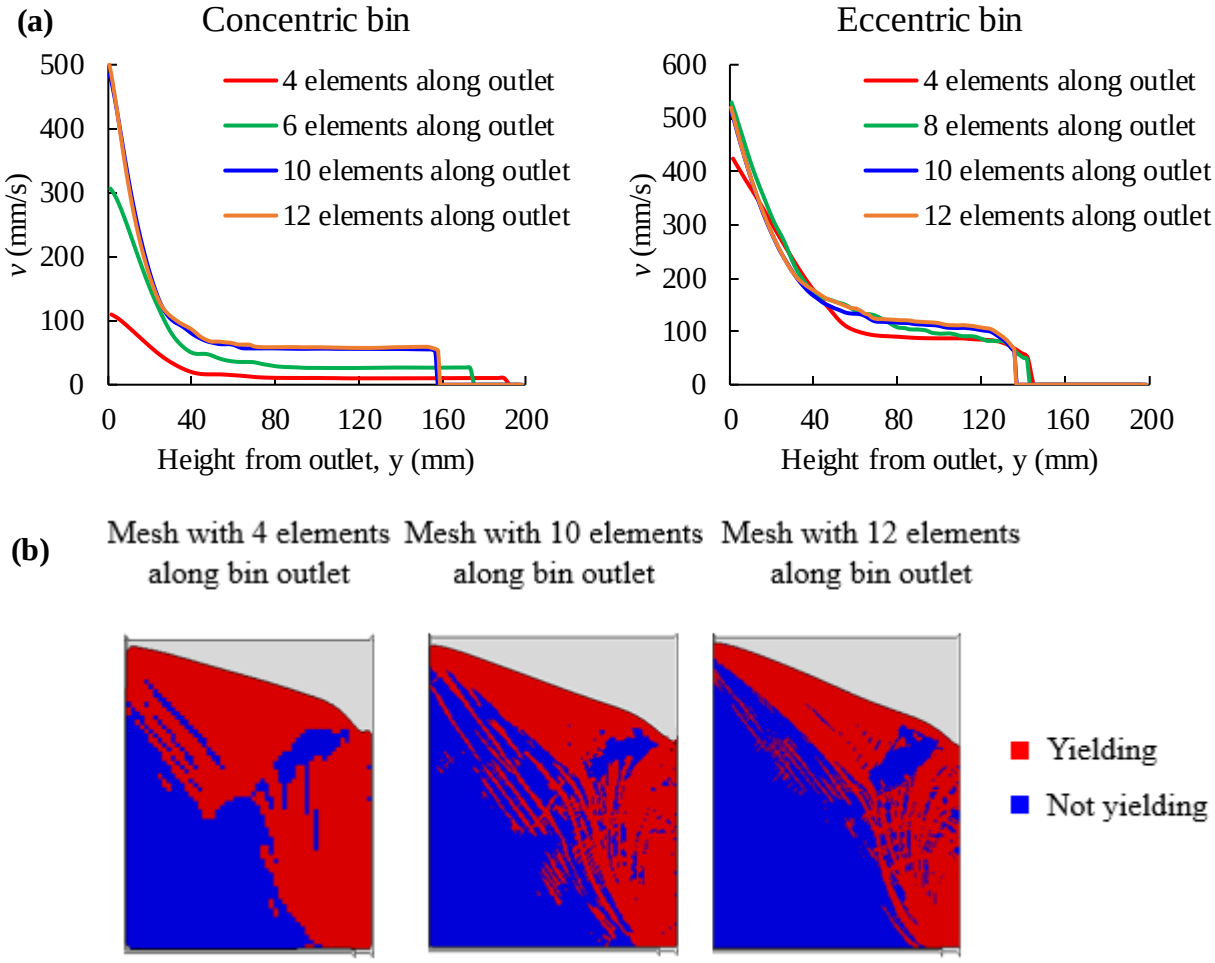

Figure 5.7. Effect of mesh density on (a) velocity profile obtained along a vertical path through the outlet center and (b) the region of yielding mesh elements at 1 s after opening the outlet.

5.5 Quantitative Comparison of Flow Characteristics

Discharge flow characteristics obtained from the experiments are compared with the converged FEM DS and NDNS simulations. Specifically, the steady state velocity profiles, the MDR and T_{SS}, and the free surface profiles during discharge are compared for both bins. At least three experimental trials were performed with approximately the same initial material fill height of 200 mm to demonstrate the reproducibility of the experimental data.

5.5.1 Velocity Profiles

Similar to Maiti et al.'s [81] work, the velocity profile comparisons are made for the vertical component of velocity obtained along a horizontal path at a given height from the bin outlet. Time averaging similar to the experimental velocity profiles is also performed for the FEM simulations. It should be noted that the FEM velocity profiles are obtained from mesh elements in the vicinity of the front wall, since the 2D PIV analysis conducted in this work reports velocities of particles in contact with the front wall.

Figure 5.8 shows a quantitative comparison of the steady state velocity profiles. It can be observed that for both bins the differences between FEM NDNS and DS velocity profiles are negligible, especially at H = 10 mm. The peak velocity magnitude of these two cases is similar, while some difference is observed in the spread of the velocity profiles (length of the flowing region at given height). A larger spread is observed for the NDNS case due to a larger region of yielding mesh elements, while a smaller spread is observed for the DS case due to narrower region of yielding mesh elements. This narrow region of yielding mesh elements is a direct consequence of the implemented material softening.

As demonstrated previously, for the low resolution images the experimental peak velocity magnitude is slightly underpredicted at H = 10 mm for the concentric bin. Regardless, the FEM simulations for both NDNS and DS overpredict the velocity profile near the outlet resulting in a larger volumetric flow rate through the outlet, $\dot{Q}^{FEM} > \dot{Q}^{Exp}$.

Overall, the velocity profiles from both FEM cases exhibit similar trends as that of the experimental velocity profiles in terms of the decreasing magnitude of the peak velocity and increasing spread observed with increasing height from the outlet. These observations along with the overprediction of velocity near the bin outlet are consistent with results from the hypoplastic model simulations of Böhrnsen et al. [46]. The current model agreement is better at larger heights from the outlet, implying that the FEM peak velocity magnitude reduces at a faster rate with increasing distance from the outlet.

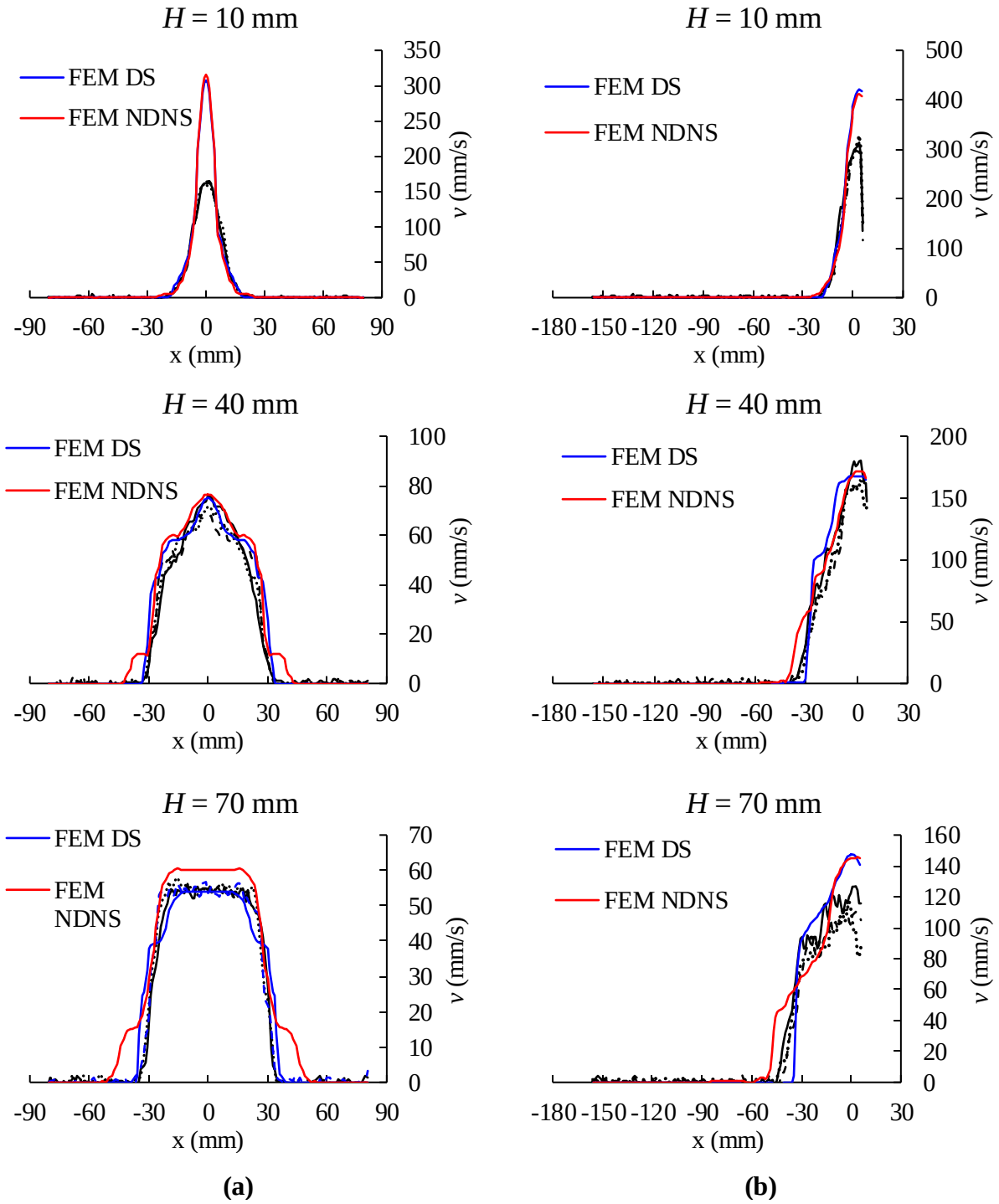

Figure 5.8. Comparison of steady state velocity profiles for (a) concentric and (b) eccentric bins at different heights (H) from the outlet. Black solid, dotted, and dashed lines denote three different experimental trials.

5.5.2 Mass Discharger Rate (MDR) and Duration of Steady MDR (T_{SS})

Figure 5.9a and b show the data obtained from the weighing scale placed directly below the bin outlet. It can be observed that the variation of cumulative mass with respect to time shows the same linear trend in all trials.

To determine the experimental MDR and the duration of steady MDR (T_{SS}), the average cumulative mass from the three trials was calculated at each time instance. Based on this average cumulative mass variation, the instantaneous MDR was calculated from 1 s onwards. A sudden change (greater than 10%) in the instantaneous MDR was observed at the beginning of the plateau region (refer to Figure 5.9). The time instance just before this sudden change was used to determine the T_{SS} value. The experimental MDR was then determined by performing a linear regression on the data points from all three trials up to the T_{SS} time instance.

Similar to the observations reported by Maiti et al. [54], the MDR through eccentric bin is larger than the concentric bin. One of the reasons for this MDR difference could be due to the fact that while discharging through the eccentric bin, particles interact with the right side wall in Figure 5.2b, which has a wall friction angle of 7^o. However, for a concentric bin, particles on the left and right side of the bin centerline interact with each other, with an internal friction angle of 34^o. Due to the smaller resistance faced by particles sliding against the right-side wall in the eccentric bin, the eccentric MDR is larger than the concentric one. An eccentric bin simulation was performed in which the right-side wall had a wall friction angle of 34^o and, indeed, the mass discharge rate decreased significantly when compared to the 7^o wall friction angle case.

Figure 5.9c and d show the comparison of the FEM MDRs to those from the experiments. The FEM MDR is calculated based on the product of the vertical component of velocity, the bulk density, and the cross-sectional area of the mesh elements in the vicinity of the outlet. The FEM MDR reaches a steady value rapidly after opening the outlet and remains steady for some time. Unlike the velocity profiles, there is a significant difference in the NDNS and DS MDRs due to significantly different bulk densities near the outlet.

It should be noted that the initial bulk density value has a major impact on the MDR of the FEM NDNS case. Although not shown here, if the initial bulk density of 1600 kg/m^3 reported by the Schulze ring shear cell is used, the MDR predicted by the FEM NDNS case is smaller; however, it is still larger than the experimental MDR. The MDR of the FEM DS case is independent of the

initial bulk density as the flowing bulk density near the bin outlet depends on the assumed particle arrangement in the constant volume state, which is independent of the initial bulk density.

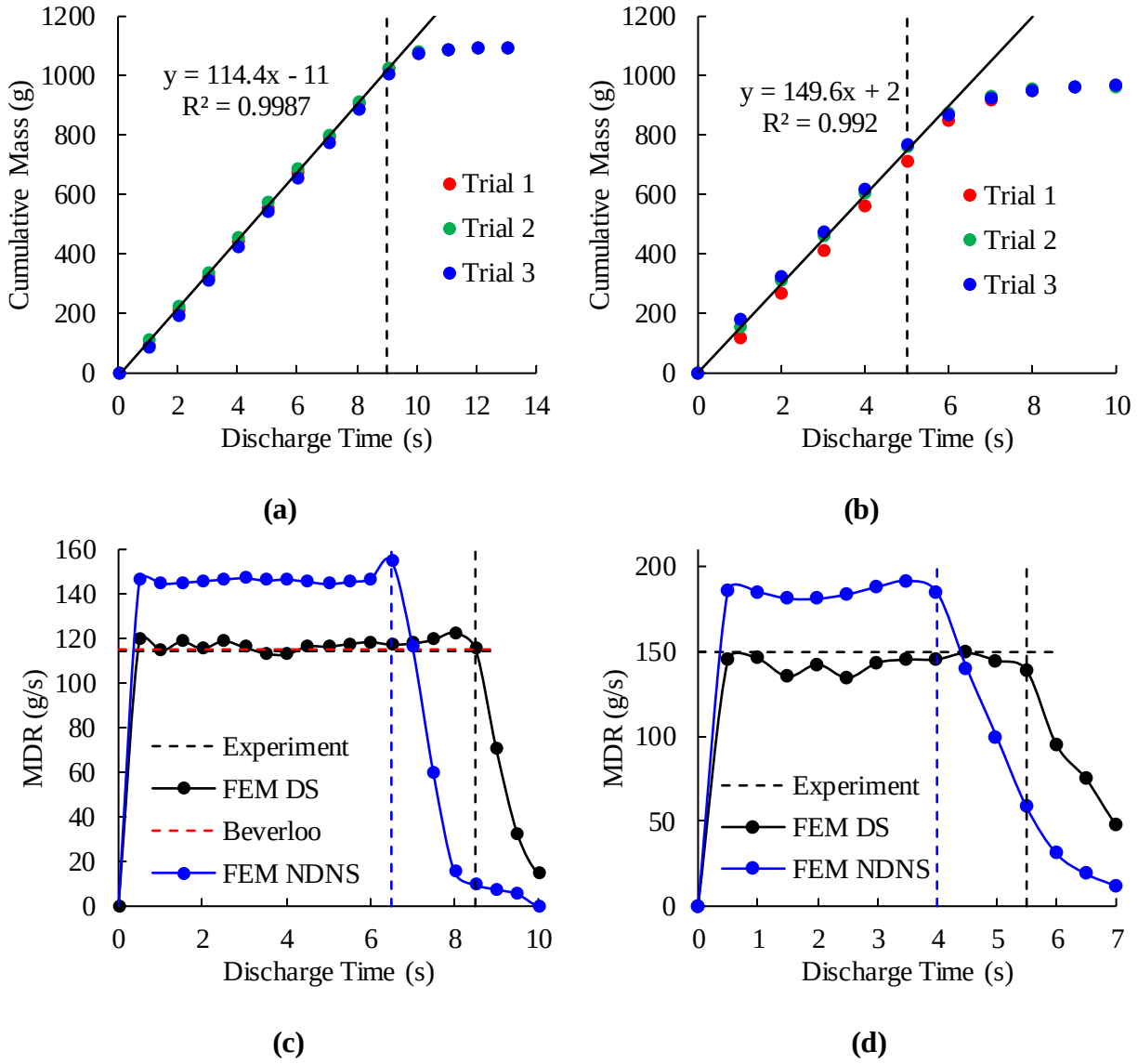

Figure 5.9. Weighing scale data from the experiments (cumulative mass collected on the scale as a function of time) for (a) concentric and (b) eccentric bins. Mass discharge rate comparisons for (c) concentric (the Beverloo MDR overlaps experimental MDR) and (d) eccentric bins.

For both bins, the FEM DS MDR is closer to the experimental MDR. This observation combined with the previous observation that $\dot{Q}^{FEM\ DS} > \dot{Q}^{Exp}$ implies that $\rho_{Outlet}^{FEM\ DS} < \rho_{Outlet}^{Exp}$. Thus, the magnitude of the experimental dilation is smaller than the one assumed in the FEM DS case ($\rho_{cv}^{Exp} > \rho_{cv}^{FEM\ DS}$).

For the concentric bin, comparison is also made to the MDR given by Beverloo's correlation presented in chapter 1, Eq. (1.4) to Eq. (1.6).

According to Nedderman [16], the coefficient C in Eq. (1.4) can take values between 0.58 to 0.64. It was observed that good agreement is obtained when $C = 0.64$. The larger value of C implies that the magnitude of experimental dilation is small.

The T_{SS} for the FEM cases was obtained by locating the sudden change in the instantaneous MDR obtained at 0.5 s intervals, as was discussed previously. The comparisons of the T_{SS} values follow the same trend as those of the MDR comparisons, as shown in Table 5.4. For both bins, the T_{SS} of DS simulations are closer to the experimental measurements.

Table 5.4. Comparison of T_{SS} values.

Bin	Experiment	FEM DS	FEM NDNS
Concentric	~9 s	~8.5 s	~6.5 s
Eccentric	~5 s	~5.5 s	~4 s

5.5.3 Free Surface Profiles

The FEM free surface profile depends significantly on the material dilation and corresponding softening as shown in Figure 5.10. There are two features associated with the FEM free surface profile evolution. The first is the contour of the free surface. For the FEM NDNS case the free surface is convex while for the DS case the free surface is linear or slightly concave. This shape is a consequence of a having a smaller region of yielding mesh elements for the FEM DS case than for the NDNS case.

The second free surface feature is the height of the free surface at a given time instance, which is observed to be governed by the material dilation. For the FEM DS case, the free surface height is larger since the material in the upper bin region moves only after the material near the outlet has reached its critical volumetric strain. Due to dilation of the material near the outlet, there is some delay in the movement of the material in the upper bin region. In contrast, for the FEM NDNS case the material in the upper bin region starts to deform at the same time as the material near the outlet.

The FEM free surface profiles shown in Figure 5.10 are observed to remain similar until the end of the discharge. The significant difference in the free surface profiles highlights the importance of material dilation and associated softening.

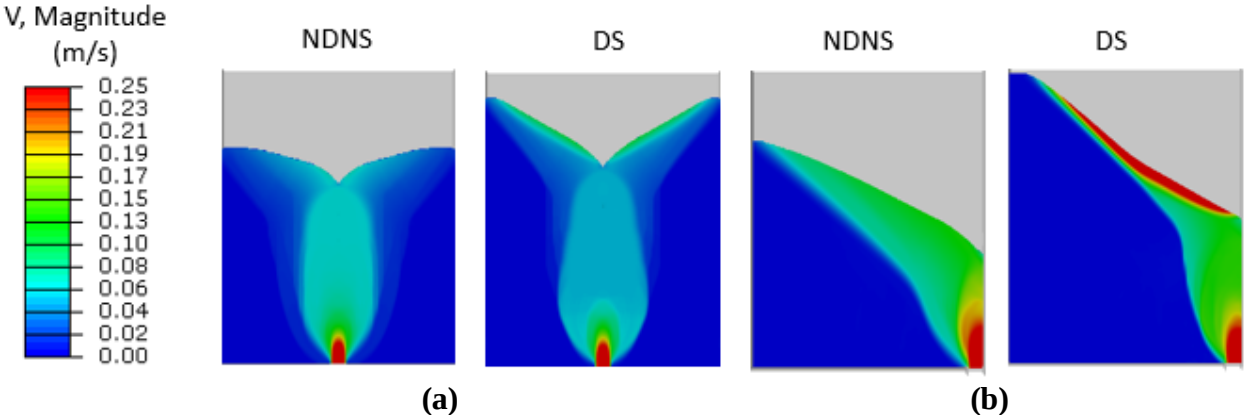

Figure 5.10. FEM free surface and velocity profiles for (a) concentric and (b) eccentric bins t = 2.5 s after opening the outlet.

Images extracted from the experiments' camera recordings (similar to the images shown in Figure 5.2) were processed in MATLAB to obtain the free surface profile evolution during the discharge process. These images were first converted to binary images and the height of the free surface along the length of the bin was calculated through image analysis. Due to the camera's limited field of view, only part of the free surface profiles were captured during the early portion of the discharge process.

The experimental and FEM free surface profiles are compared at different time instances during the discharging process as shown in Figure 5.11. As expected, the free surface height given by the FEM DS simulations is larger than the height given by the NDNS simulations for both bins. The shape of the free surface predicted by the FEM DS simulations agree well with the experimental free surface.

Similar to the conclusions derived from the MDR comparisons, it can be concluded that the actual material dilation must be smaller than the one assumed in the FEM DS case, i.e., $\rho_{cv}^{Exp} > \rho_{cv}^{FEM\ DS}$. It should be noted that another source of the mismatch in free surface height includes a slight delay from opening of the bin outlet and starting the camera recording.

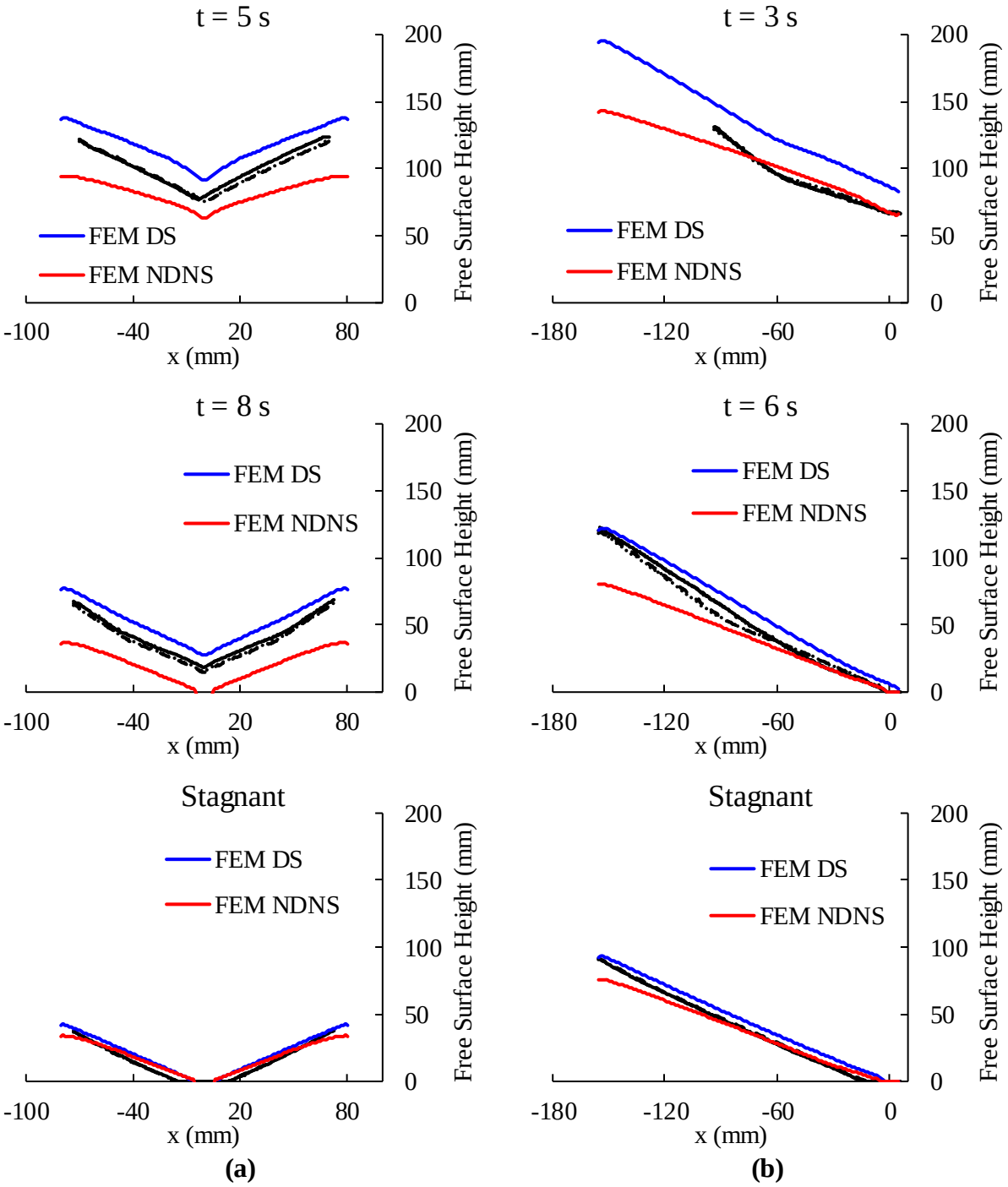

Figure 5.11. Free surface profile comparisons at various discharge stages for (a) concentric and (b) eccentric bins. Black solid, dotted, and dashed lines indicate three experimental trials. These three black lines overlap in many of the plots.

The free surface profile of the eccentric bin experiment features two distinct linear segments in left and right parts of the bin, with the left part exhibiting a larger slope than the right part as shown in Figure 5.11b (3 s and 6 s). This two-segment free surface profile can also be seen in Figure 5.2b as well as in the images reported by Maiti et al. [81]. Approximate calculations of these two linear segments showed that the left part had a slope close to 45^{o} (close to the peak internal friction angle) while the right part had a slope of 34^{o} (close to the constant-volume internal friction angle), supporting the fact that the material strength is dependent on the degree of deformation. Material softens as it flows down from the left to the right part of the eccentric bin. A similar two-segment free surface profile was observed in the concentric bin experiments near the end of the discharge process, albeit to a smaller extent.

The comparison of the free surface shape for both bins indicate that the FEM DS simulations are more accurate than the NDNS simulations. The apparent mismatch between the DS predictions and the experiments is thought to be due to a smaller dilation in the real material than what is assumed in FEM DS case.

6. HOPPER FLOW OF COHESIVE PARTICULATE MATERIALS

This chapter aims to demonstrate effectiveness of FEM in modeling cohesive particulate materials. An approach to predict the critical outlet width of wedge-shaped hopper is presented using FEM and the Mohr-Coulomb elasto-plastic model. This approach incorporates dynamic discharge of the stored material under gravity and a variable material unconfined yield strength (f_c) based on the consolidation stresses (σ_1). A clear flow/no-flow boundary is observed, which is compared with the theories of Jenike and Enstad as well as McLean's correlation. The influence of different simulation parameters on the predicted critical outlet width and agreement between FEM and these theories are also investigated. Finally, the validity of the FEM results is shown through comparisons with the experimental results reported by Eckhoff and Leversen [15,24].

6.1 Theoretical Critical Outlet Opening

Jenike [2] provided an analysis for determining the stress profiles developed inside a hopper. His approach assumes that for a particulate material in a passive stress state, the mean stresses (σ) inside the hopper are proportional to the radial distance from the hopper apex (r). During steady flow of cohesive materials, the stresses are assumed to lie on the effective yield locus (EYL) of the material as opposed to the incipient yield locus (IYL). The EYL passes through the shear stress-normal stress origin and is tangent to the Mohr's circles passing through the end points of all the IYL (Figure 6.1). The radial stress assumption is assumed valid inside the converging hopper section and these radial stresses are independent of stresses applied by material in the silo portion of the hopper, which has vertical walls.

To determine the critical outlet width, Jenike assumed that once the steady flow of a cohesive material is stopped, the material consolidates under stresses determined from the radial stress theory. The unconfined yield strength (f_c) of the material under these consolidation stresses can be determined from the material's flow function. Although the flow function of a real material may exhibit some curvature at low stresses, the flow function in the present work is assumed to be a linear function of the consolidation stress, σ_1, similar to the Enstad's theory,

$$f_c = f_{c0} + k\sigma_1. \tag{6.1}$$

Here k is the flow function slope and f_{c0} is the unconfined yield strength at zero consolidation stress. Linear flow functions are exhibited by many pharmaceutical powders at high consolidation stresses [87]. It is often observed that for many materials, the internal friction angle (ϕ) does not change significantly with consolidation stress [62,87]. Therefore, it is assumed to be constant in the present work. Enstad demonstrated that under the assumption of a constant internal friction angle (ϕ) and linear flow function, the EYL passing through the origin cannot have a fixed effective angle of internal friction (δ). Enstad proposed a modified EYL that does not pass through origin, but still has a fixed effective angle of internal friction (δ_{mod}) as shown in Figure 6.1. Furthermore, the modified effective angle of internal friction (δ_{mod}) can be determined from values of the internal friction angle (ϕ) and flow function slope (k),

$$sin\ \delta_{mod} = \frac{2\ sin\ \phi + k(1 - sin\ \phi)}{2 - k(1 - sin\ \phi)}. \tag{6.2}$$

If an arch forms after opening the outlet, the material is now in an incipient failure state and stresses are given by the IYL. In Jenike's theory, the critical outlet width can be found using the unconfined yield strength (f_c) of the material in the vicinity of the hopper outlet and a force balance in the vertical direction. Neglecting the stresses applied by the material above a thin layer near the outlet, Jenike obtains the major principal stress due to the weight of the material, $\overline{\sigma_1}$,

$$\overline{\sigma_1} = \rho g B / \sin(2\beta), \tag{6.3}$$

where B is the outlet width, β is the angle between the major principal stress direction and the normal to the wall, ρ is the material bulk density at the outlet, and g is the acceleration due to gravity. The angle β depends on the wall friction angle (ϕ_w) and hopper half angle from the vertical (θ) [16]. The flow/no-flow criterion is determined through a comparison of $\overline{\sigma_1}$ and the corresponding unconfined yield strength (f_c). The critical outlet width is then given by,

$$B_{critical} = \frac{f_c \sin(2\beta)}{\rho g}. \tag{6.4}$$

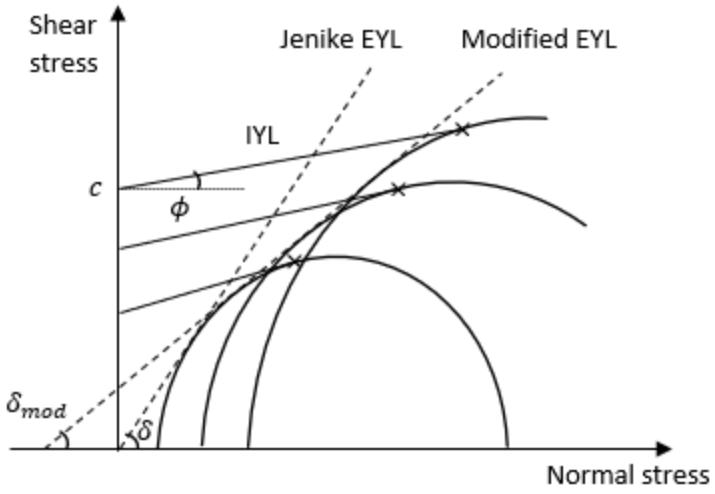

Figure 6.1. Jenike's effective yield locus and Enstad's modified EYL. Also shown in the figure are the incipient yield locus (IYL), the internal friction angle (ϕ), the effective angle of internal friction (δ), the modified effective angle of internal friction (δ_{mod}), and cohesion (c).

Based on Jenike's work, McLean [23] generated a correlation for the critical outlet width,

$$B_{critical} = f_c(1 + 0.005\theta)/\rho g, \tag{6.5}$$

where θ (the hopper half angle measured from the vertical) is in degrees. This correlation is often used as an alternative to the design charts provided by Jenike [16]. Since both Eq. (6.4) and Eq. (6.5) are based on Jenike's work, distinction between these two equations is made by terming Eq. (6.4) as "Jenike" and Eq. (6.5) as "McLean" in subsequent sections.

It should be kept in mind that the basis of Jenike's flow/no-flow criterion is comparing the unconfined yield strength (f_c) to the major principal stresses produced due to the weight of the material inside a thin material layer ($\overline{\sigma_1}$) near the hopper outlet. Since the stresses applied by the material above this thin layer are neglected, the critical outlet width calculated through this criterion does not depend on the material height above the outlet. The conservative nature of the critical outlet width estimate obtained from the Jenike's theory is now evident.

Enstad [15] proposed another theory to reduce the conservative nature of Jenike's critical outlet width estimate. His theory assumes that a cohesive arch has a circular arc shape with its center-point lying on the hopper centerline. The angle made by this circular arc with the wall normal depends the wall friction angle (ϕ_w) and the hopper half angle (θ). Furthermore, it is assumed that inside the converging hopper section, the major principal stresses act tangentially to such circular arcs and are of constant magnitude. Through a vertical force balance on a differential

element enclosed by two circular arcs at a radial distance r from hopper apex, Enstad arrived at the following differential equation in terms of the minor principal stress for the material under incipient failure ($\overline{\sigma_2}$),

$$r\frac{d\overline{\sigma_2}}{dr} - X_b\overline{\sigma_2} = -\rho g Y_b r + Z_b\left(\frac{r}{R}\right)^X + Z_0, \tag{6.6}$$

where X_b, Y_b, Z_b, X and Z_0 depend on the material properties and hopper geometry. For the complete expressions of these variables, refer to Enstad [15]. The parameter R is the radial distance from hopper apex to the material's upper free surface.

Using the minor stress boundary condition at the top surface ($\overline{\sigma_2}(r = R)$), the solution to this differential equation is,

$$\overline{\sigma_2}(r) = a\left(\frac{r}{R}\right)^X + b\left(\frac{r}{R}\right)^{X_b} + c\left(\frac{r}{R}\right) + d. \tag{6.7}$$

Here, variables a, b, c, and d are functions of the variables defined previously [15].

To obtain the critical outlet width $B_{critical}$, an iterative procedure can be used to find r_{outlet} such that the minor stress at the outlet is zero. Unlike Jenike's theory, the critical outlet width now depends on the material height through the parameter R. The unconfined yield strength (f_c) is obtained similarly, assuming that the material consolidates under a passive state of stresses. Based on the modified EYL, these consolidation stresses are given by,

$$\sigma(r) = \frac{\rho g Y r}{X-1} + \left(\sigma_R - \frac{\rho g Y R}{X-1}\right)\left(\frac{r}{R}\right)^X. \tag{6.8}$$

The major difference in Jenike's and Enstad's theories is in the dependence of the critical outlet width on the material height. Figure 6.2 shows the variation of the critical outlet width with material height for the two theories and McLean's correlation for the parameters listed in Table 6.1. The material top surface is assumed to be a free surface ($\sigma_2(r = R) = 0$). The modified effective angle of internal friction (δ_{mod}) is obtained from Eq. (6.2). The cohesion (c) is related to the unconfined yield strength (f_c) by,

$$f_c = 2c\cos\phi/(1-\sin\phi). \tag{6.9}$$

The cohesion at zero consolidation stress (c_0) is reported in Table 6.1. Case A parameters represent a pharmaceutical powder [87], whereas Case B represents a hypothetical material with smaller internal friction angle (ϕ) (corresponding to clay material), larger cohesion, and ideal

frictionless walls. These cases are chosen for comparison because they show negligible and significant deviations between the theories, respectively. The dependence on material height in the Enstad's critical outlet width estimate is negligible for Case A, but is significant for Case B. It was observed that for other reasonable values of parameters, the height dependence of Enstad's estimate lies in between these two extreme cases.

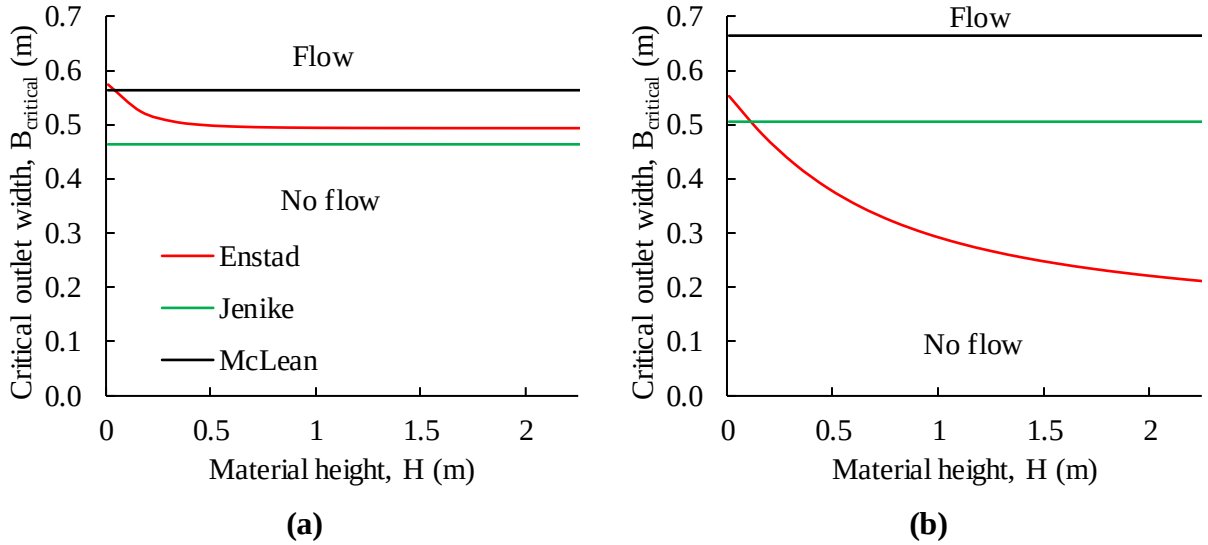

Figure 6.2. Comparison of critical outlet widths. (a) Using the parameters listed for Case A in Table 6.1. (b) Using the parameters listed for Case B in Table 6.1. If the outlet width is smaller than the predicted critical outlet width, then no flow occurs. If the outlet width is larger than the predicted critical value, then flow does occur.

For Case B, both Enstad's and Jenike's theories predict that the material will flow for an outlet width of 60 cm, but the McLean correlation predicts no flow. For a hopper with an outlet width of 30 cm, Jenike's theory and the McLean correlation predict no flow while Enstad's theory predicts flow as long as the material height is greater than about 1 m.

Table 6.1. Parameters for two cases exhibiting, respectively, negligible and significant dependence of critical outlet width on material height.

Parameter	Case A	Case B
Bulk density, ρ	400 kg/m^3	
Hopper half angle from the vertical, θ	30°	
Internal friction angle, ϕ	40°	20°
Wall friction angle, ϕ_w	20°	0°
Slope of the flow function, k	0.2	0
Cohesion at zero consolidation stress, c_0	350 Pa	800 Pa

Although not explored here, other theories [14,88,89] follow a similar approach as that of Enstad, but the assumed shape of the arch differs (circular, parabolic [14,88], folded plate [89]). It is expected that the results from these theories would show a similar dependence on the material height as that predicted by Enstad's theory.

Certainly, the analytical work of Jenike, Enstad, and others has been instrumental in the design of hopper systems; however, the models have limitations. To make the models tractable for simple calculations, simplifying assumptions must be made, such as two-dimensional hopper geometries, constant material properties, and ignoring the effect of the material above the hopper outlet. Continuum-based computational models of hopper systems, as described in the following section, can be used to predict performance in situations not amenable to analytical calculation.

6.2 FEM Simulation Setup

The finite element simulations developed here use the Lagrangian approach in the commercial Abaqus/6.14-6 software [49]. A symmetric wedge-shaped hopper is modeled using a 2D plane strain assumption in order to compare against the Jenike and Enstad theories and the McLean correlation. According to Jenike [71], a plane strain assumption can be made for hoppers with outlet length greater than three times the outlet width. The initial simulation domain is shown in Figure 6.3a. The geometry consists of a converging hopper section, but no silo part with vertical walls. It is assumed that any arch formed will have a circular arc profile with its center at the hopper apex. This pre-defined arch shape is necessary in the current FEM implementation since fracture of the continuum material does not occur and, thus, natural evolution of the arch, if it

exists, cannot occur. After opening the outlet, if material flow does occur, elements near the outlet will deform extensively. If no flow occurs, only small element deformations appear. The FEM model also cannot be used to determine if an arch forms after some period of discharge, again due to the lack of a fracture model in the current simulations. The use of a pre-defined arch shape is also used in the analyses by Jenike and Enstad.

Note that this arch profile differs from the arch profile assumed in Enstad's theory where the arch center-point does not coincide the hopper apex but instead depends on the hopper wall angle and the major principal stress direction. The impact of the center location is discussed in more detail in the Section 6.5. To improve computational speed, only half of the hopper is modeled, and a symmetry boundary condition is used along the centerline. Four node plane strain quadrilateral elements (CPE4R) are used to discretize the bulk material and the hopper wall is represented as a rigid body. The use of reduced integration elements with one integration point and hour glass control prevent locking in plane strain elements. The default element settings of Abaqus are sufficient to avoid volume or shear locking [49]. A rigid plate having circular shape similar to the hopper outlet is also used to simulate closing and opening of the outlet.

The particulate powder is modeled using Abaqus's Mohr-Coulomb elasto-plastic model. Previous researchers [37,38,41] have demonstrated the effectiveness of the Mohr-Coulomb model for hopper systems. For detailed information on implementation of this model, please refer to Abaqus [49], and Liu et al. [41]. Other material constitutive models could also be implemented in FEM, such as the Drucker-Prager Cap [61,62], Cam Clay [48], non-local hypoplastic models [31], or non-local granular rheology models [90]; however, the Mohr Coulomb model is used here, in part, because the widely-used Jenike design guidelines and Enstad's theory are based on this model. As is demonstrated in the Section 6.5, the Mohr-Coulomb model produces good outlet width predictions when compared against experimental results.

Three dynamic simulation steps with explicit time integration are used. In the first step the hopper outlet is closed by assigning a contact interaction between the rigid outlet plate and material nodes near the outlet. Gravity is then applied with a smooth step function. A smooth application of gravity ensures that transients associated with material settling are negligible. Similar to the layer-by-layer filling method used in previous FEM studies [37,40], this approach generates an active state of stress where the major principal stresses are oriented vertically at the hopper centerline. In Jenike's or Enstad's theories, it is assumed that the material consolidates in a passive

state during filling, where the major principal stress is oriented horizontally at the hopper centerline. Nedderman [16] reports that inside the converging hopper section, a passive state of stresses prevails as material gets compressed circumferentially and expands radially. This assumption is reasonable because in experiments the material often slides along the hopper wall during filling and gets compressed with the addition of more material above it. As demonstrated by Guo et al. [56], a passive state of filling also prevails during application of a surcharge pressure on the top surface of the material.

To achieve a passive state during filling in FEM, the material was allowed to slide down the hopper wall a small distance before opening the outlet. This state was achieved by sliding the rigid outlet plate radially towards the hopper apex by a small distance. A comparison of the resulting stress fields showed that the final stresses remain similar irrespective of the sliding distance as long as the sliding process is performed slowly. In the third step, the hopper outlet is opened by deactivating the contact interaction between the material and the outlet plate and the flow/no-flow condition of the material is observed.

The material does not dilate in the present work since it is assumed that the material has reached its constant-volume/residual state under the passive state of consolidation stresses, which occurs when the outlet is closed after initial partial discharge of the material. Hence, the residual values of the internal friction angle and wall friction angle are used. The dependence of mobilized parameters on the initial void ratio or initial bulk density is neglected as the corresponding peak values are a function of initial void ratio, but the residual values remain almost constant [62,91]. Incorporating the parameter dependence on plastic strain may be necessary, however, for the prediction of critical outlet width under an active state of consolidation stresses in which the material near the hopper outlet has not yet reached its constant-volume/residual state.

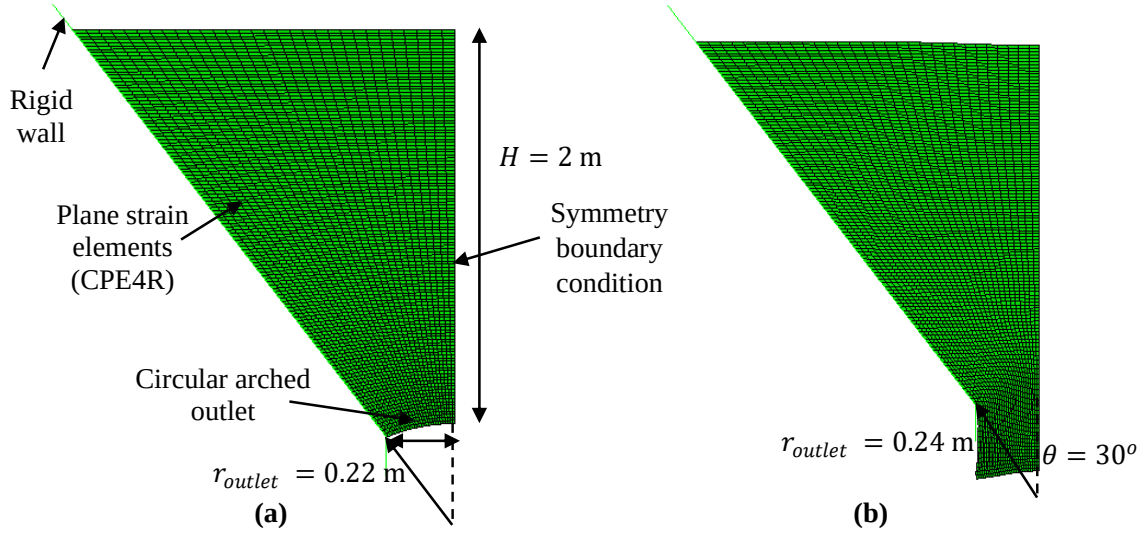

Figure 6.3. (a) FEM computational domain and (b) Lagrangian mesh deformation indicating flow.

It should be noted that the concept of the EYL is not needed for the FEM model. The material consolidates under stresses developed during the sliding step prior to opening of the hopper outlet. The material's unconfined yield strength (f_c) is determined through the use of a subroutine that interpolates the cohesion parameter (c) of the Mohr-Coulomb constitutive model based on the major principal stress developed at the end of the sliding step for each mesh element. The cohesion parameter (c) is dependent on the consolidation stresses until the sliding step only. After opening the outlet, the material is in an incipient state of failure. Any further softening of the material that may occur during steady discharging flow is irrelevant for determining the critical outlet width.

As mentioned previously, the internal friction angle (ϕ) of the material is assumed to be constant, but this assumption could be relaxed in the model so that the internal friction angle (ϕ) is a function of the consolidation stresses (σ_1), but as reported previously, only slight variations are usually observed in the residual internal friction angle values [62,91]. Although the elasticity modulus (E) and Poisson's ratio (υ) do not affect the critical outlet width significantly (Section 6.4), values representing a generic pharmaceutical powder are used with $E = 10$ MPa and $\upsilon = 0.2$ [38,62,92]. Abaqus has the capability of varying all of the material properties and wall friction angle based on the consolidation stresses, which would likely improve the accuracy of the model.

The model parameter values can be dependent on various factors such as the particle size distribution, particle shape, and moisture content. Therefore, characterization of the material under the same conditions found in the hopper system is essential for accurate predictions.

The hopper has a small radius of the outlet (r_{outlet}) initially. If the material is observed to not flow when the contact interaction with the outlet plate is removed, the radius of the outlet is then increased by 2 cm in a new simulation. Thus the critical outlet radius is determined to within 2 cm in current work, implying that the critical outlet width ($B_{critical}$) is determined to within $(4\text{ cm})\sin\theta$ (refer to Figure 6.3a). One example of flow and no-flow mesh deformations is shown in Figure 6.3. Using the parameters of Case B in Table 6.1, it is observed that for an outlet radius of 22 cm the mesh structure remains similar to the initial computational domain after the outlet plate is removed. However, for the outlet radius of 24 cm, material flows as soon as the outlet is opened. The abrupt change in mesh deformation gives the flow/no-flow boundary for this case. The critical outlet width is expected to lie in between these adjacent flow and no flow outlet widths. In all cases it is observed that for the smaller value of the flow/no-flow outlet width interval, the material completely stops moving within 1 s after opening the outlet width. Whatever sliding that may have occurred in this 1 s period is less than one half of the mesh element length. Comparing this small sliding with the large continuous deformation observed for the outlet width given by the larger value of the flow/no-flow interval, it can be safely concluded that the critical outlet width lies somewhere within this interval.

For each case, FEM can provide two estimates corresponding to the active (no sliding of the outlet plate) and passive (sliding of the outlet plate) states of filling stresses. These two estimates are the same for $k = 0$ as in Case B, but the difference between them increases as k increases. Only the passive state estimate is reported in the present work since in most experiments material slides along the hopper walls during filling, thus consolidating under a passive state of stress.

6.3 Mesh Convergence Analysis

Mesh convergence analysis is performed for each case to ensure that the adjacent flow and no flow outlet widths do not change significantly Figure 6.4 shows the mesh convergence analysis for Case B parameters and a material height of 2 m. As mentioned before, the radius of the outlet was increased in steps of 2 cm to observe the flow/no-flow boundary and the corresponding outlet width intervals are reported in the figure. It can be observed that the outlet width interval remains

the same for more than 30 elements along the hopper outlet width. Therefore, 30 mesh elements along the outlet of circular arc shape (total of ~7000 elements to model all of the material) are chosen for this particular case. Similar convergence analyses were performed for each case. Time step analysis demonstrated that the default time step determined by Abaqus produces converged critical outlet width results.

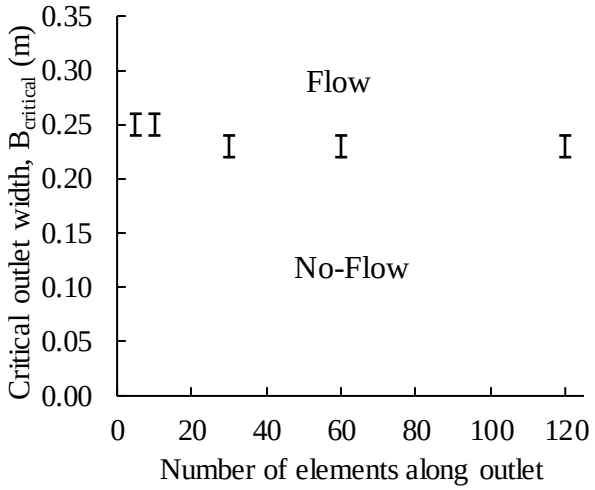

Figure 6.4. Mesh convergence analysis for parameters corresponding to Case B in Table 6.1 and a material height of 2 m.

It is interesting to note that, although refining of the mesh increases the oscillations observed in the stress profiles, the effect on the FEM predicted flow/no-flow interval is negligible. It is observed that with mesh refinement the thickness of the shear zones decreases significantly as shown in Figure 6.5.

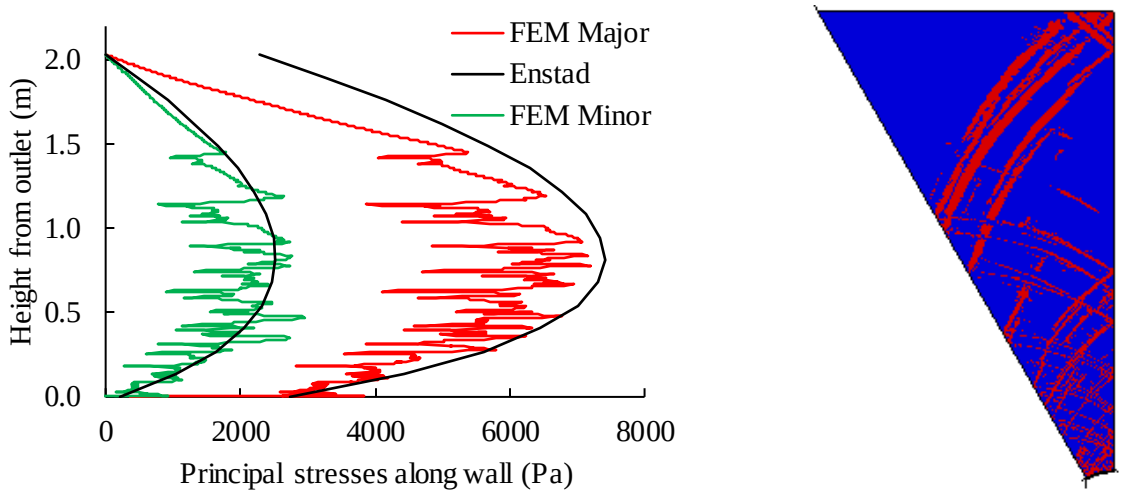

Figure 6.5. (a) Stress profile and (b) shear zones using a very fine mesh (120 elements along the outlet). Parameters for Case B are used in these simulations. These results should be compared to those of Figure 6.7a.

6.4 Elastic Property Independence

The elastic properties of particulate materials have little effect on the critical outlet width estimate as observed in Figure 6.6. The elastic modulus and Poisson's ratio are varied while the other parameters use the values for Case A of Table 6.1. It is observed that both the elastic modulus and Poisson's ratio have negligible impact on the FEM predicted flow/no-flow outlet width interval.

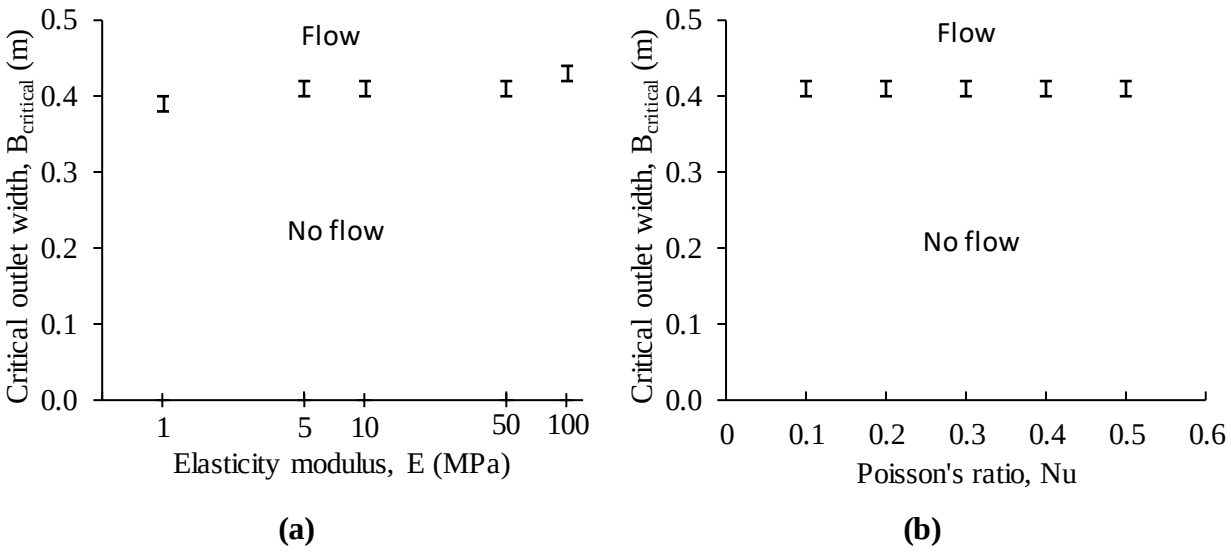

Figure 6.6. Effect of (a) Elastic modulus and (b) Poisson's ratio on the FEM predicted flow/no-flow interval.

6.5 Results and Discussion

6.5.1 Comparison of Stress Profile

Verification of the stresses developed when the material is in incipient failure is provided in Figure 6.7a for a material height of 2 m. Parameters corresponding to Case B are used for this stress comparison. Immediately after opening the outlet for an outlet width of 24 cm, the stresses along elements close to the wall are obtained. For this outlet width the material flows. The stresses from Enstad's theory are obtained using the same parameters used in the FEM simulation. A good match is observed for both the major and minor principal stresses near the hopper outlet. The major principal stresses from the FEM model deviate from Enstad's theory near the top surface as the material does not yield in this region (the blue region in Figure 6.7b). The oscillations observed in the FEM stress profile are due to yielding (red in Figure 6.7b) and non-yielding (blue in Figure 6.7b) consecutive elements along the plotted path. Although not shown here, a similar comparison of stresses along the elements near the hopper centerline showed excellent agreement between the FEM results and Enstad's theory.

In current analysis, a regularization technique to control the thickness of shear zones (zones of yielding mesh elements) is not used; hence, the thickness of the shear zones observed depends

on the mesh density. This phenomenon affects the oscillations observed in the stress profile, but its effect on the FEM predicted flow/no-flow interval is negligible as presented in section 6.3. Direct comparison to experimental stress profiles was not possible mostly due to the unavailability of such stress profiles along with complete material characterization data. However, widely-used silo design standards are based on the approximate analytical theories (Walker, Enstad, Jenike). Therefore, the comparison is made against stress profile predicted by Enstad's theory.

It is observed that for Case A, Jenike's radial stress assumption matches the Enstad and FEM predictions near the hopper outlet, but increasingly deviate as the upper material free surface is approached. This deviation reflects the fact that Jenike's approach neglects the upper free surface. This particular limitation of the radial stress theory is also acknowledged by Jenike. For Case B, due to the small value of the internal friction angle (ϕ) and ideal frictionless wall, the influence of the upper material free surface is significant as is apparent from the value of the exponent 'X' in second term of Eq. (6.8) ($X \approx 7$ for Case A and $X \approx 1$ for Case B). The smaller value of X in Case B results in much smaller consolidation stresses predicted through the Enstad's theory and FEM predictions than Jenike's radial stress theory, even near the hopper outlet.

It is observed that the stress comparison between the FEM model and Enstad's theory worsens with increasing wall friction because the theoretical assumption used by Enstad of constant principal stresses along the circular arcs throughout the converging hopper section becomes increasingly inaccurate, as the distance from the outlet increases. In the FEM simulations, mesh elements are observed to yield in localized, smaller regions resulting in significant variation of the principal stresses along the circular arcs of Enstad's theory. Additionally, the number of yielding mesh elements are also observed to decrease with increasing wall friction along the hopper wall. Stress comparisons for a case of 20^{o} wall friction angle with corresponding shear zones are shown in Figure 6.7c and Figure 6.7d. Note that the outlet width is approximately 58 cm for this case. Due to the lack of experimental data in the literature (with corresponding material characterization), it is unclear which stress profile is more accurate.

This comparison demonstrates that the FEM simulations using a Mohr-Coulomb elasto-plasticity model compares favorably to Enstad's theory for predicting the internal stress state of a cohesive bulk solid. The FEM model also shows where the Enstad and Jenike assumptions become inaccurate.

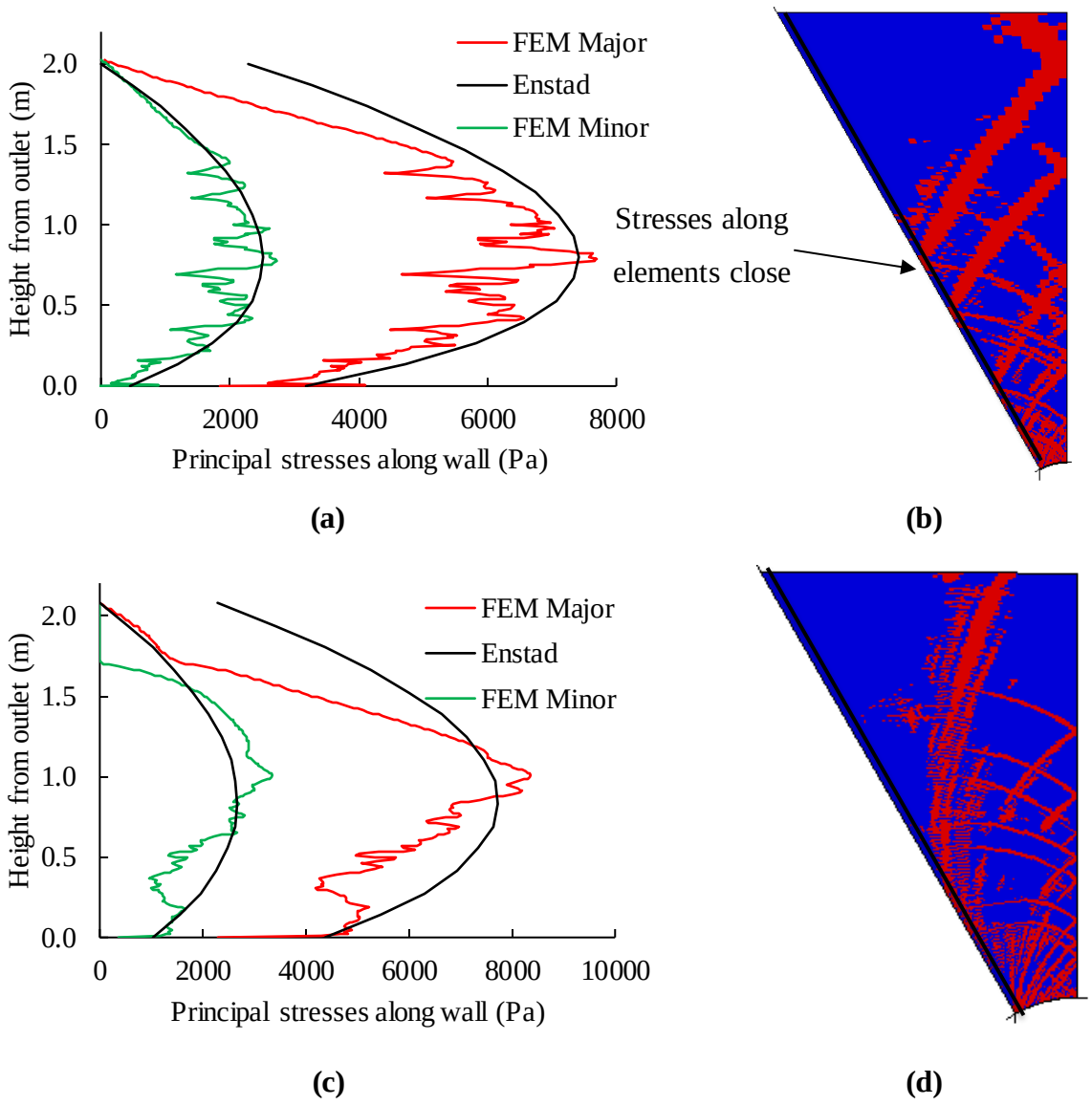

Figure 6.7. (a) Comparison of FEM principal stresses to Enstad's theory for Case B. (b) Corresponding yielding (red) and non-yielding (blue) elements in the FEM model. (c) Stress comparison for a wall friction angle of 20^{o} and (d) Corresponding yielding and non-yielding elements.

6.5.2 Comparison of Critical Outlet Width

Figure 6.8 shows the comparison of the critical outlet width predicted by the FEM model to the Jenike and Enstad theories and the McLean correlation. Recall that because the radius of the outlet (r_{outlet}) is increased in increments of 2 cm in the FEM model, the critical outlet width ($B_{critical}$) is only known to within a $(4\text{ cm})\sin\theta$ range. Similar to the theories, the FEM results show insignificant dependence on the material height for Case A. However, for Case B the FEM

results demonstrate significant material height dependence similar to the Enstad's theory. Additionally, the FEM results are closer to the Enstad's theory than Jenike's theory for this case.

An important ramification of this observed dependence on material height for Case B is that, if the outlet width is not large enough, some material can flow through the hopper before the flow stops because the critical outlet width increases with decreasing material height. To ensure that the material is discharging continuously for a given outlet width, a continuous material inflow would need to be ensured at the top surface of the hopper. Alternately, to ensure that all of the material discharges from a hopper with no in-flow, the largest critical outlet width prediction for any material height should be used. The prediction from McLean would provide the most conservative estimate, followed by Enstad, Jenike, and then the FEM prediction for the present analysis. Obviously, the choice of which prediction to use depends on the application and risk assessment.

For Case A, the FEM results show deviations from Enstad's theory mainly due to three reasons. The first reason for the mismatch is the difference in shape of the assumed material arch. As mentioned previously, in the FEM approach, the center-point of the material arch lies at the hopper apex while the center-point of Enstad's outlet does not lie on the hopper apex. A set of FEM simulations were also performed using the arch profile given by Enstad as shown in Figure 6.8a. Some difference is expected in the predicted critical outlet widths due to different arch shapes as the consolidation stresses near the outlet change. As expected, using Enstad's arch shape in the FEM model results in increased critical outlet widths that are much closer to Enstad's theory. Enstad's theory also assumes that all of the material inside the hopper is yielding and the principal stresses along the circular arcs are of constant magnitude throughout the hopper. The FEM results show deviations from both of these assumptions. As a result of localized yielding of mesh elements, the principal stresses do not follow the Enstad trend as the distance from the outlet increases. One conclusion from this analysis is that the critical outlet width can be a strong function of the material arch shape.

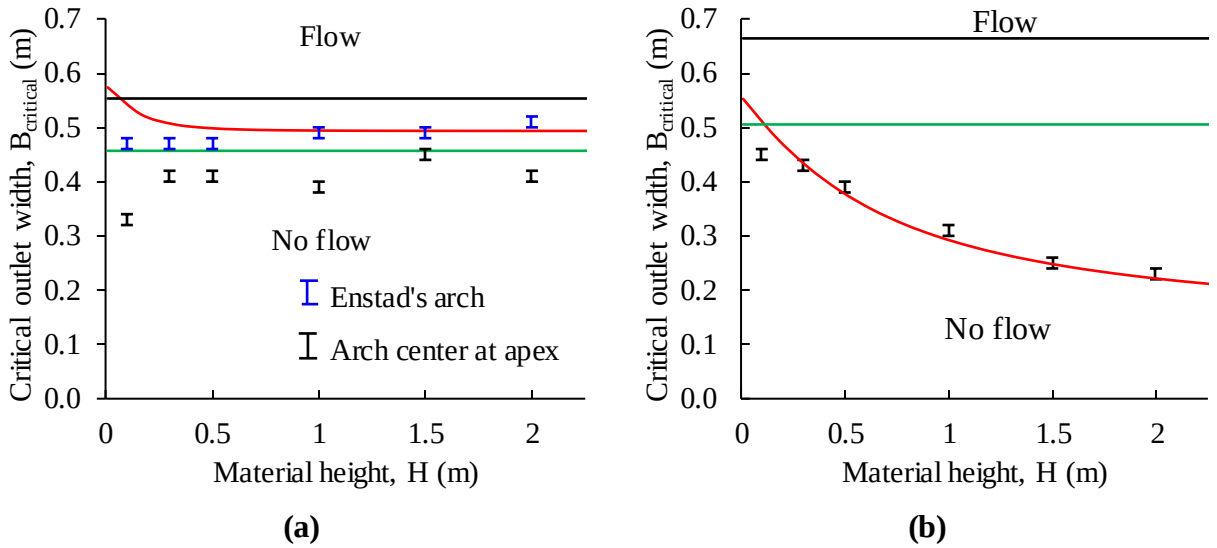

Figure 6.8. Comparison of critical outlet widths (a) using parameters of Case A in Table 6.1 and (b) using parameters of Case B in Table 6.1. The green line denotes the Jenike estimate, the red line denotes the Enstad estimate, and the black line denotes the McLean estimate. The black and the blue data points are from FEM simulations corresponding to locating the arch center at the apex (black) and using the same arch as Enstad (blue).

6.5.3 Parametric Study

To understand how each parameter affects the critical outlet width and the agreement between FEM and theoretical estimates, a parametric study is performed by varying one parameter of Case A, while keeping the other parameters constant for a material height of 2 m (Figure 6.9). Instead of using the radial stress theory to obtain the consolidation stresses for the Jenike and McLean estimates, the first radial term of Eq. (6.8) was used. It was observed that the Jenike radial factor does not vary significantly from Enstad's radial factor.

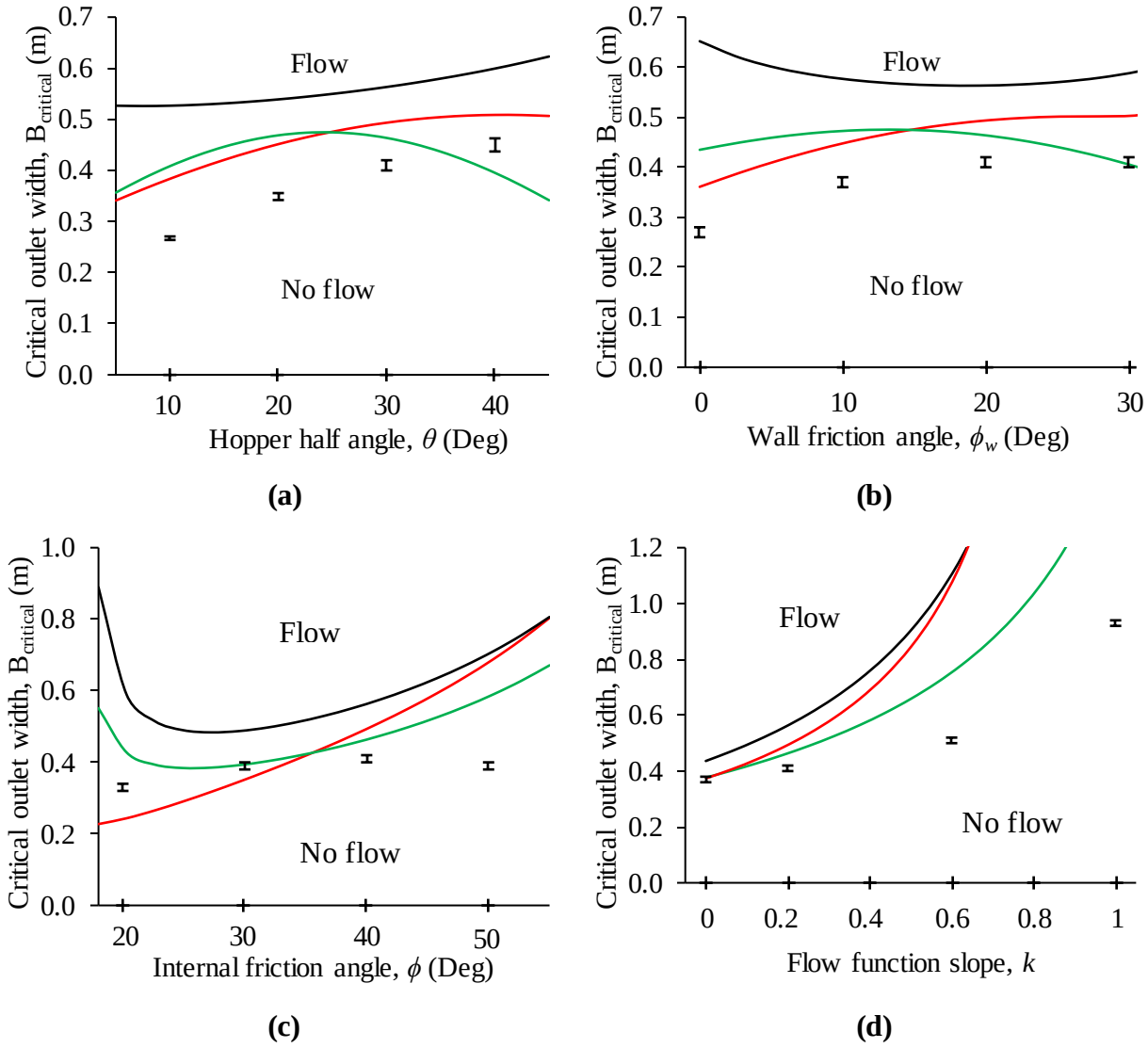

Figure 6.9. Effects of (a) hopper half angle from the vertical, (b) wall friction angle, (c) internal friction angle, and (d) slope of the linearized flow function on the critical outlet width. Only one of the parameters is varied while keeping others constant, with the baseline parameters given in Table 6.1 for Case A. The green line denotes the Jenike estimate, the red line denotes the Enstad estimate, and the black line denotes the McLean estimate. The FEM predictions are given by the data points.

To analyze the effect of the hopper half angle from the vertical (θ) on the critical outlet width, the height of the material along the centerline was kept the same for different values of the angle. As seen in Figure 6.9a, the critical outlet width increases with increasing hopper half angle similar to Enstad's theory. This trend is expected since the lift forces from the hopper walls increase with increasing hopper half angle according to the Enstad theory. The variation of critical outlet width shows a sinusoidal trend as expected. The Jenike and McLean estimates differ

significantly from the Enstad and FEM results. This is because the Jenike and McLean estimates are appropriate for mass flow hoppers (where the radial stress field assumption is valid), with increasing hopper half angle the flow mode transitions towards funnel flow.

Increasing the wall friction angle (ϕ_w) increases the lift forces from the hopper walls, thus increasing the critical outlet width (Figure 6.9b). For both FEM and Enstad's theory, the critical outlet width remains similar from $\phi_w = 20^o$ to 30^o. Enstad assumed that the angle made by the arch abutments with the normal to the hopper wall is such that the arch gets the maximum lift from the walls. In Jenike's theory no such assumption was made and, therefore, the critical outlet width decreases after a certain value of the wall friction angle. The observed FEM results support the assumption of maximum lift made in Enstad's theory.

According to the Enstad and Jenike theories, the critical outlet width should increase as the internal friction angle (ϕ) increases. This behavior is expected since the unconfined yield strength (f_c) increases with increasing internal friction angle (ϕ) for fixed cohesion (c). As observed from Figure 6.9c, the FEM results follow this trend for $\phi < 40^o$, but the FEM critical outlet width decreases for internal friction angles approximately greater than $\phi = 40^o$. The primary reason behind this deviation from Enstad's theory is thought to be due to localized yielding of mesh elements in FEM. This localization separates a region of non-yielding material near the upper corner of the hopper from the material near hopper outlet, resulting in a large principal stress variation along the circular arcs, especially away from the hopper outlet, which is different from Enstad's assumption.

As the slope of the flow function (k) increases, the material's unconfined yield strength (f_c) increases for similar consolidation stresses, as expected (Figure 6.9d). Therefore, a larger outlet width is needed to overcome this increased unconfined yield strength. The FEM critical outlet width follows the non-linear increasing trend similar to the theories, but large deviations occur at larger values of the flow function slope (k) with the FEM estimates being smaller than the theoretical ones. Although not explored here, an increasing critical outlet width can be expected with increasing cohesion at zero consolidation stress (c_0).

6.5.4 Comparison to Experiments of Eckhoff and Leversen

The critical outlet widths predicted by the previously presented theories and the FEM model are compared against the wedge-shaped hopper experiments performed by Eckhoff and

Leversen [24]. The experimental hopper setup (Figure 6.10a) had an adjustable hopper half angle and outlet width. Two experiments were conducted for fine polymer powder and fine SiC powder. The measured material properties are given in Table 6.2. For the original experimental measurements of the powder properties, refer to Eckhoff and Leversen [24] and Eckhoff et al. [93]. These properties are also reported by Enstad [15]. Elastic properties were not mentioned in Eckhoff and Leversen's work, but since their effect on the critical outlet width is negligible (based on parametric study results not presented here; similar findings of elasticity modulus and Poisson's ratio having negligible effect on material segregation have been reported by Liu et al. [41])., arbitrary but reasonable properties were chosen.

Table 6.2. Experimental parameters measured by Eckhoff and Leversen [24].

Parameter	**Polymer Powder**	**SiC Powder**
Hopper half angle from vertical, θ	14.5^o	16^o
Internal friction angle, ϕ	34^o	28.6^o
Wall friction angle, ϕ_w	26^o	33.3^o
Slope of the flow function, k	0.62	0.47
Cohesion at zero consolidation stress, c_0	519 Pa	175 Pa
Bulk density, ρ	440 kg/m^3	900 kg/m^3
Elasticity modulus, E*	10 MPa	
Poisson's ratio, ν*	0.2	

* Not reported by Eckhoff and Leversen. Reasonable, but arbitrary values are assumed.

FEM simulations were performed on the 2D computational domains shown in Figure 6.10b and Figure 6.10c. According to the FEM simulations, for the case of the fine polymer powder, the material flows for an outlet width of 18.5 cm and does not flow for an outlet width of 18 cm. For the fine SiC powder, the material flows for an outlet width of 9.4 cm and does not flow for an outlet width of 8.8 cm. Table 6.3 compares the critical outlet width estimates from the Jenike and Enstad theories, McLean's correlation, and the FEM model. The theoretical estimates differ from similar ones reported by Enstad [15] as the modified EYL is used in the present work as opposed to the conventional EYL used by Enstad. It is most likely that the experimental observation was

made for a passive state of filling as the hopper walls were slid upwards to observe flow/no-flow of the material.

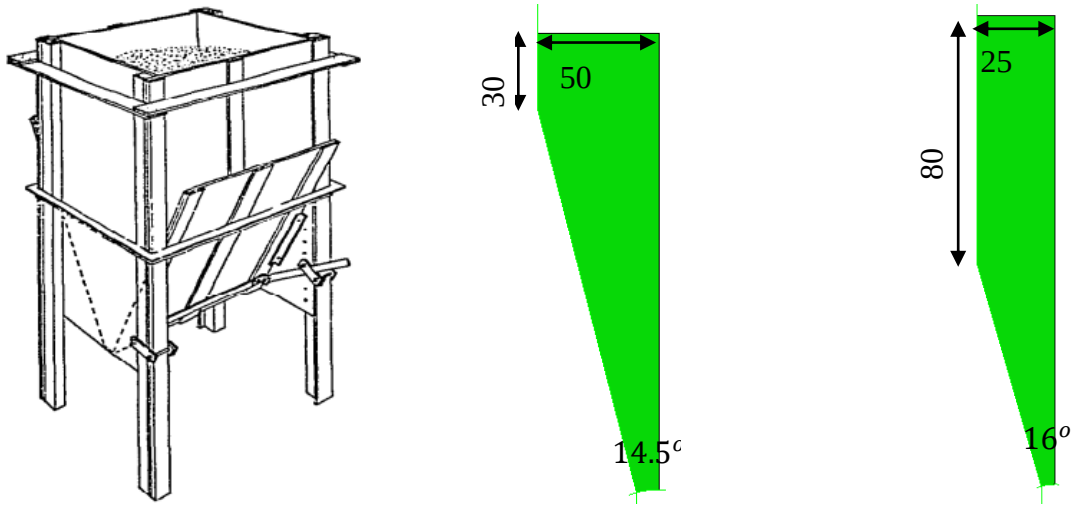

Figure 6.10. (a) Experimental setup of Eckhoff and Leversen [24]. FEM computational domains for (b) fine polymer particles and (c) SiC powder. The hopper width was not reported in [24].

The FEM model gives an excellent prediction for the fine polymer powder whereas the error is relatively large for the fine SiC powder. Based on Enstad's discussion, this over-prediction of the critical outlet width for fine SiC powder is thought to be due to the linear extrapolation of the material's flow function near the low stress region. Small unconfined yield strengths at low stresses are observed by Schulze and Wittmaier [94] for highly dispersed dry powder, by Johanson [95] for plastic pellets, and by Swize et al. [96] for pharmaceutical powders. To investigate if this is the cause behind the over-prediction, an arbitrary bilinear flow function, shown in Figure 6.11, is implemented in the FEM model. This simple modification is a simple approximation to account for the non-linearity in the flow function at small consolidation stresses since the actual flow function data is unavailable. This bilinear flow function has half the unconfined yield strength at zero consolidation stress compared to the original linear flow function ($f_{c0}^{Bilinear} = 0.5 f_{c0}^{Linear}$). The bilinear flow function merges with the linear flow function at the intersection point of $f_c = \sigma_1$ line and the linear flow function. It should be noted that this bilinear flow function reduces the unconfined yield strength of the material near the hopper outlet where the consolidation stresses are smaller than ~1000 Pa, but material above and near the hopper transition remains unaffected. The reduced unconfined yield strength of the material near the hopper outlet results in a much

better prediction of the critical outlet width as seen in Table 6.3. Depending on the availability of flow function measurements at small stresses, a more accurate non-linear flow function could also be implemented in FEM. A prediction of the critical outlet width based on a non-linear flow function would not be possible for the analytical models presented here, giving added advantage to the FEM approach.

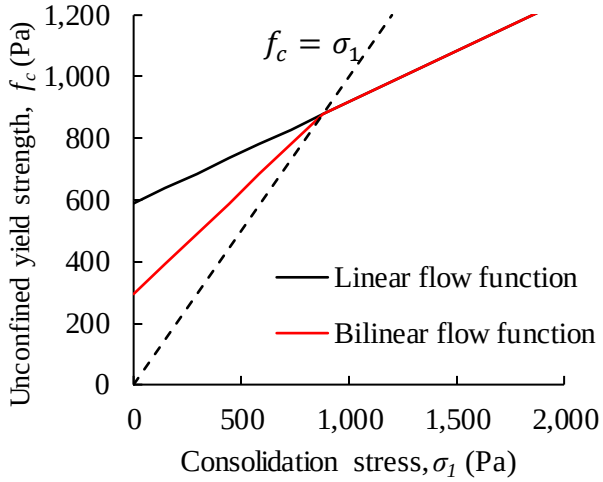

Figure 6.11. Modified flow function for the fine SiC powder.

The improved critical outlet width prediction based on the bilinear flow function emphasizes the importance of detailed material characterization, especially at the small consolidation stresses observed near the hopper outlet.

The FEM model provides the least error in the critical outlet width, by a considerable margin, when compared to the theoretical estimates for both experiments. These results demonstrate that the FEM/Mohr-Coulomb material model provides better predictions of the critical hopper outlet width than the commonly-used theories. One downside of the FEM model is that it takes approximately 30 min to set up a simulation and approximately 30 min to run a single case on a desktop PC. Predictions using the theoretical approaches can be made in a fraction of a second.

Comparisons to additional published experimental data has proved difficult due to the lack of material Mohr-Coulomb characterization data along with critical outlet width measurements. An attempt was made to predict the critical outlet width measured by Guo et al. [56]; however, the predictions were found to be inaccurate, particularly at large surcharge stresses, due to the inability

of the Mohr-Coulomb model to capture the densification of the compressible iron ore material used in Guo et al.'s experiments. Thus, the model presented in the current work is more appropriate for use with materials that may be reasonably approximated as incompressible.

Table 6.3. Comparisons of the critical outlet width predictions to the experiment.

		Experiment	McLean	Jenike	Enstad	FEM (Linear flow function)	FEM (Bilinear flow function)
Fine Polymer	$B_{critical}$ (cm)	20	35	28	30	[18.5, 18]	
	% deviation		75.6	37.6	49.8	[-7.4, -9.9]	
SiC powder	$B_{critical}$ (cm)	5	12	10.2	10.4	[9.4, 8.8]	[6.1, 5.5]
	% deviation		139.5	104.4	120.2	[87.4, 76.4]	[21.3, 10.3]

7. CONCLUSIONS

The objectives set in chapter 2 have been achieved in chapter 4, 5, and 6. Conclusions drawn from these three chapters, hopper flow of cohesionless materials, quantitative comparison of hopper flow characteristics with experiments, and hopper flow of cohesive particulate materials are compiled here.

7.1 Summary of Results

In chapter 4, FEM based on elasto-plastic constitutive model is implemented to predict various flow characteristics of plane strain converging hopper system. Three different elasto-plastic models of Abaqus, the Mohr-Coulomb, Drucker-Prager, and Drucker-Prager Cap model are compared. It is concluded that the Drucker-Prager Cap model produces excessive dilation under low stresses encountered near the material free surface due to its elliptic plastic potential surface. Therefore, this model is incapable of providing realistic hopper flow behavior of cohesionless particulate materials.

After converting the Mohr-Coulomb material parameters through conversion equations appropriate for plane strain system, the linear Drucker-Prager model produced equivalent results in terms of the filling and discharging wall normal stress, outlet velocity profile, and mass discharge rate.

Following conclusions are drawn from comparison to the analytical theories and to the mass discharge rate (MDR) correlations, and from the parametric studies:

- Both filling and discharging wall normal stresses of FEM simulations agree well with modified Walker's theory.
- For properly chosen value of ‘diffusion length’ FEM velocity profile agrees with prediction of the kinematic model. Earlier observations [19] about increase in the value of diffusion length with hopper height are confirmed from FEM observations.
- The dilation angle significantly affects the FEM mass discharge rate. Fixed non-zero dilation angle results in continuously decreasing MDR, while linear reduction in the dilation angle produces steady MDR.

- FEM mass discharge rate results confirm the dependence on hopper outlet width ($b^{3/2}$) as well as hopper half angle ($(\tan\theta)^{0.35}$) suggested by the empirical mass discharge rate correlation of Rose and Tanaka [22].
- Hopper flow mode prediction based on the application of mass flow index criterion agrees well with Jenike's chart [2].
- FEM simulations demonstrate experimentally observed 'stress peak' as material suddenly starts discharging. It is observed that oscillations created by such stress peak damp out quickly for large values of elasticity modulus, whereas, for decreasing values of elasticity modulus, it takes longer for the oscillations to damp out due to larger value of the stable time increment.
- It is observed that with increasing internal friction angle as well as the wall friction angle, the peak wall normal stress shifts higher up the hopper and the mass discharge rate decreases.
- Constant volume solid fraction does not affect the outlet velocity distribution but has a small effect on diffusion of velocity through the hopper.
- All of the above observations suggest that FEM analysis is capable of predicting some hopper flow characteristics such as wall normal stress, velocity profile, mass discharge rate, and hopper flow mode. In addition, such analysis can provide particulate material behavior under situations where continuum analytical theories fail short. For example, FEM analysis can be used for simulations of transient systems with complex geometry, where continuum theories are bound to fail.

Good agreement obtained between the FEM simulations and continuum analytical theories increase the confidence in capability of FEM. To analyze if the FEM flow characteristics quantitatively agree with experimental results, comparison is made with particle image velocimetry (PIV) experiments conducted on Ottawa 20-30 sand discharging through a laboratory-scale bin in chapter 5.

The velocity profiles, mass discharge rate, duration of steady MDR (T_{SS}), and free surface profiles predicted by FEM simulations with and without material softening and dilation are compared with experiments. To assess the flexibility of the FEM, both concentric and eccentric bins are simulated, and corresponding one-to-one comparison is performed. Two FEM cases are

investigated, with material dilation and associated softening (FEM DS) and without material dilation or softening (FEM NDNS).

Following conclusions are drawn from this comparison:

- There is a negligible difference in the velocity profiles obtained from 'FEM DS' and 'FEM NDNS' simulations.
- Both cases produce velocity profiles with peak velocity magnitude larger than the experimental one at a height of 10 mm from the outlet. Implying that the FEM volumetric flow rate through the outlet is larger than the experimental one ($\dot{Q}_{Outlet}^{FEM} > \dot{Q}_{Outlet}^{Exp}$).
- Velocity profile agreement is better at larger heights from the outlet, for e.g. at H = 40 mm and H = 70 mm. Implying that the FEM velocity magnitude decreases at a faster rate with increasing height when compared to the experimental velocity profiles.
- FEM velocity profiles exhibit similar trends as experiments in terms of decreasing peak velocity magnitude and increasing 'spread' (width of flowing zone) with increasing height.
- There is a large difference in the mass discharge rate of FEM DS and FEM NDNS case as expected due to the difference in the material bulk density near the outlet. FEM DS mass discharge rate is smaller than FEM NDNS and is closer to the experimental data for both concentric and eccentric bins. Implying that the experimental bulk density near outlet is larger than the one assumed in FEM DS case ($\rho_{Outlet}^{Exp} > \rho_{Outlet}^{FEM\ DS}$).
- The duration of steady MDR (T_{SS}) follows trends similar to the MDR comparison with T_{SS} of FEM DS being closer to the experiment than the T_{SS} of FEM NDNS.
- The shape of the experimental free surface is linear in concentric bin and is bi-linear for eccentric bin.
- The two features of the free surface profile, the shape and height are significantly different between FEM DS and FEM NDNS cases.
- The FEM NDNS case produces convex free surface profiles for both bins, while FEM DS case is capable of reproducing the linear free surface observed in concentric bin and the bi-linear concave profile observed in the eccentric bin.
- The height of the free surface predicted by the FEM NDNS case is smaller than the experimental free surface due to the absence of material dilation. The height of the FEM

DS case is larger than the experimental free surface due to larger dilation than the experimental one ($\rho_{cv}^{Exp} > \rho_{cv}^{FEM\ DS}$).

- Overall, FEM DS case is more realistic but experimental dilation is smaller than the one assumed in this case. Consistent results obtained for concentric and eccentric bins demonstrate the flexibility of FEM modeling.

In chapter 6, hopper flow of cohesive particulate materials is simulated through FEM modeling using the Mohr-Coulomb constitutive model. FEM based on the Lagrangian analysis technique is capable of predicting the critical outlet width (COW) for cohesive bridging. Comparison of FEM predicted COW is made with theoretical estimates of Jenike and Enstad as well as empirical correlation of McLean. Parametric study is performed to understand the effect of material properties and hopper geometry on the COW. Comparison to experimental results available in literature is also done to assess accuracy of FEM predicted COW.

Following conclusions are drawn from the FEM modeling of cohesive particulate materials:

- Jenike's COW estimate and McLean's empirical correlation do not take into account the effect of initial material height. FEM COW does depend on the initial material height and is observed to agree well with Enstad's theoretical COW.
- The initial material height dependence is significant for material like cohesive clay stored in a hopper with idealized frictionless wall. But the COW for cohesive pharmaceutical powders stored in the hopper exhibit negligible dependence on initial material height.
- Parametric studies show that the FEM results follow trends similar to that of Enstad's theory, but significant deviations occur at large values of the internal friction angle and the flow function slope, where Enstad's assumptions become increasingly inaccurate. These deviations are due to yielding of the mesh elements in localized regions that result in significant variation in the principal stresses along the circular arcs of Enstad's theory.
- The FEM and Enstad predictions can also differ due to differences in the assumed shape of the material arch. In most cases the COW predicted with the FEM model is smaller than the theoretical estimates of Enstad and Jenike.
- Comparisons to the two experiments of Eckhoff and Leversen demonstrate that the FEM model provides a much better estimate of the COW than the theoretical predictions. The

FEM model provides an accurate prediction (between 7 to 10%) for the fine polymer powder used by Eckhoff and Leversen.

- For the SiC powder there is a significant error (error between 76 to 87%). The cause for this large discrepancy is thought to be due to the linearized extrapolation of the flow function at small consolidation stresses.
- Using a modified bilinear flow function results in much better prediction with an error between 10 and 21%. The more accurate prediction using a bilinear flow function for SiC powder highlights the importance of obtaining material characterization data at small consolidation stresses observed near the hopper outlet. The FEM predictions are better than the theoretical models, which have errors greater than 104%.
- The FEM based on the Mohr-Coulomb model is unable to accurately predict the COW of compressible iron ore material at large surcharge loads in the experiments by Guo et al. [56]. The poor predictions are presumed to be due to the inability of the Mohr-Coulomb model to capture material densification.

7.2 Thesis Contributions

The analysis and quantitative comparison presented in this thesis serves to demonstrate the effectiveness of FEM based on simple elasto-plastic model to predict hopper flow of particulate materials. The major advantages of FEM are the smaller computational times, applicability to large-scale industrial hopper systems, and requirement of only the bulk material properties for the constitutive model implementation. FEM based simulations of granular materials can be used to simulate complex hopper systems or other processing equipment. The accuracy of these simulations depends on a detailed material characterization and corresponding implementation in Abaqus.

Some work presented in this thesis is indeed inspired from similar studies available in the literature, but there are a few significant contributions that serve as filling the gaps in the literature and further improving the FEM modeling approach.

Most of the work presented in chapter 4 is similar to the analysis presented by Zheng and Yu [38] for the case of conical hopper. An important improvement is made in terms of the effect of dilation angle on hopper mass discharge rate. The linear reduction in the dilation angle based on the assumption of particle packing structure during filling and discharging does affect the mass

discharge rate significantly. This dilation angle variation results in steady mass discharge rate similar to the experimental observations.

The one-to-one quantitative comparison presented in chapter 5 is unique and provides a thorough investigation of the hopper flow characteristics predicted through FEM based on a simple Mohr-Coulomb model. The effect of the material dilation and associated softening on the mass discharge rate and free surface profile highlights the necessity to modify the in-built constitutive models of Abaqus to obtain realistic hopper flow characteristics.

The FEM modeling of cohesive particulate materials provided in chapter 6 is different from prior FEM hopper modeling studies, as the current model incorporates dynamic discharge of the stored material under gravity and a variable material unconfined yield strength based on the consolidation stresses. Using this approach, a clear flow/no-flow boundary is observed when the outlet width is changed by a small magnitude. The good agreement obtained between FEM COW and experiments of Eckhoff and Leversen show the capability of FEM approach and also the need to modify the linear flow function to non-linear one for some materials.

The contributions of this thesis can be summarized in terms of the one-to-one quantitative comparison presented for cohesionless materials by conducting experiments on laboratory-scale hoppers. Demonstrated flexibility of the Eulerian FEM analysis technique in modeling concentric and eccentric hopper. Development of a novel approach based on the Lagrangian FEM analysis to predict the critical hopper outlet width for cohesive particulate materials. An important contribution is also made in terms of the necessary modification in the simple elasto-plastic models to obtain realistic hopper flow characteristics.

It is important to note the drawbacks associated with such simple constitutive model which include inability to model the material compression during filling that significantly affects the FEM predicted mass discharge rate, inability of capturing localization of shear zones and therefore a slight mesh dependence of flow characteristics. These limitations and few ideas to improve the FEM approach are presented in the next chapter.

8. RECOMMENDATIONS FOR FUTURE WORK

Although FEM modeling presented in this work is useful in predicting some of the hopper flow characteristics of particulate materials, there are still some challenges. These challenges and recommendations for future work based on them are presented next.

In terms of elasto-plastic models, one limitation of the Mohr-Coulomb model of Abaqus is that the minimum value allowed for the dilation angle is 0.1^o. This does not make a significant difference for short term simulations, but for long term simulations, such as rotating drum, this non-zero dilation angle causes continuous reduction in the material bulk density. It is worthwhile to investigate if this issue can be resolved and exact 0^o dilation angle can be achieved.

In both Mohr-Coulomb and linear Drucker-Prager models, the material can dilate but it cannot compress, implying that the bulk density of the material can only decrease. This limitation is important in case of compressible particulate materials. It is expected that the bulk density of the material will be distributed when it is filled inside the hopper. Assuming active filling, the material near the closed outlet will have a larger bulk density which will then reduce with height as the free surface is approached. Although the Drucker Prager Cap model can simulate compression of the particulate material, its elliptic plastic potential causes unrealistic dilation at low stresses observed near the free surface.

One way to better represent the density distribution after filling step is to start with an initial condition where the bulk density is already distributed, then model the material dilation during discharge with Mohr-Coulomb or linear Drucker Prager models. For this approach to work, the experimental bulk density distribution of the filled material needs to be known a priori.

Another way to model both the compression during filling and dilation during discharge is to simulate the filling procedure with the Drucker Prager Cap model and import all of the state variables into a new simulation which is based on Mohr Coulomb or linear Drucker Prager model. An attempt made in this direction showed that importing most of the state variables is possible when linear Drucker Prager model is implemented in second simulation. It is worthwhile to further investigate this approach.

Quantitative comparison of flat-bottomed concentric and eccentric hopper is made in this thesis. Similar comparison for converging concentric and eccentric hoppers where the hopper angle is varied can also be made to further assess the FEM approach. It is observed that the FEM

approach overpredicts the velocity magnitude near the hopper outlet and the velocity reduces at a faster rate with height compared to the experimental velocity profile. The cause behind this phenomenon and corresponding improvement in the FEM modeling can be further investigated.

The FEM model presented for cohesive particulate materials in chapter 6 was based on the assumption of passive state of filling stresses. It is worthwhile to further explore applicability of similar approach for active state of filling stresses and for complex hoppers. Experiments can be done on complex hoppers to obtain the critical outlet opening for different cohesive particulate materials.

A limitation of this approach is that it cannot predict the material arch shape, which can be irregularly-shaped and dependent on the filling method, or examine phenomena such as the intermittent breakage and formation of arches in the initial stages of outlet opening or the protrusion of material before arch collapse [55,56]. One possible way of simulating the natural formation of a cohesive arch is to delete excessively deforming elements, as originally proposed by Keppler [30]. This technique should be further explored.

It is observed that the stress profile of cohesive particulate materials depends significantly on the mesh density. With mesh refinement, more oscillations are observed in the stress profile. These oscillations are due to thinner shear zones. Improvements could be made to control the thickness of these shear zones with a regularization technique.

Lastly, it is important to emphasize the need for published experimental hopper performance results with corresponding material characterization data in order to test the validity of computational models. The experiments can be performed on large-sale and complex industrial hopper systems.

REFERENCES

[1] B.J. Ennis, J. Green, R. Davies, The legacy of neglect in the United-States, Chem. Eng. Prog. 90 (1994) 32–43.

[2] A.A.W. Jenike, Gravity Flow of Bulk Solids, Utah Engineering Station, 1961.

[3] D. Schulze, Powders and Bulk Solids Behavior : Characterization, Storage and Flow, Springer, 2007.

[4] E.W. Merrow, Estimating startup times for solids-processing plants, Chem. Eng. (1988).

[5] P.A. Cundall, O.D.L. Strack, A discrete numerical model for granular assemblies, Géotechnique. 29 (1979) 47–65. doi:10.1680/geot.1979.29.1.47.

[6] C.J. Coetzee, Review: Calibration of the discrete element method, Powder Technol. 310 (2017) 104–142. doi:10.1016/j.powtec.2017.01.015.

[7] T. Li, Y. Peng, Z. Zhu, S. Zou, Z. Yin, Discrete element method simulations of the inter-particle contact parameters for the mono-sized iron ore particles, Materials (Basel). 10 (2017) 19–21. doi:10.3390/ma10050520.

[8] A. Lisjak, G. Grasselli, A review of discrete modeling techniques for fracturing processes in discontinuous rock masses, J. Rock Mech. Geotech. Eng. 6 (2014) 301–314. doi:10.1016/j.jrmge.2013.12.007.

[9] L. Jing, O. Stephansson, Fundamentals of Discrete Element Methods for Rock Engineering: Theory and Applications, Elsevier, Amsterdam/Oxford, 2007.

[10] R. Bharadwaj, W.R. Ketterhagen, B.C. Hancock, Discrete element simulation study of a Freeman powder rheometer, Chem. Eng. Sci. 65 (2010) 5747–5756. doi:10.1016/j.ces.2010.04.002.

[11] Z. Asaf, D. Rubinstein, I. Shmulevich, Determination of discrete element model parameters required for soil tillage, Soil Tillage Res. 92 (2007) 227–242. doi:10.1016/j.still.2006.03.006.

[12] Y.-C. Chung, J.Y. Ooi, A study of influence of gravity on bulk behaviour of particulate solid, Particuology. 6 (2008) 467–474. doi:10.1016/j.partic.2008.07.017.

[13] H. Janssen, Versuche über getreidedruck in silozellen, Ztg. Ver. Dt. Ing. 39 (1895) 1045–1049.

[14] D. Walker, An approximate theory for pressures and arching in hoppers, Chem. Eng. Sci. 21 (1966) 975–997.

[15] G. Enstad, A Novel Theory on the Arching and Doming in Mass Flow Hoppers, Bergen, 1981.

[16] R.M. Nedderman, Statics and Kinetics of Granular Materials, Cambridge University Press, New York, 1992.

[17] C. Coulomb, Mémoires de mathématiques et de physique présentés à l'Académie royale des sciences par divers savants, Lus sans Ses Assem. 7 (1776) 343–382.

[18] K. Walters, A theoretical analysis of stresses in axially-symmetric hoppers and bunkers, Chem. Eng. Sci. 28 (1973) 779–789.

[19] J. Choi, A. Kudrolli, M.Z. Bazant, Velocity profile of granular flows inside silos and hoppers, J. Phys. Condens. Matter. 17 (2005) 2533–2548. doi:10.1088/0953-8984/17/24/011.

[20] R. Balevičius, I. Sielamowicz, Z. Mróz, R. Kačianauskas, Investigation of wall stress and outflow rate in a flat-bottomed bin: A comparison of the DEM model results with the experimental measurements, Powder Technol. 214 (2011) 322–336. doi:10.1016/j.powtec.2011.08.042.

[21] W. Beverloo, H. Leniger, J. De Velde, The flow of granular solids through orifices, Chem. Eng. Sci. 15 (1961) 260.

[22] H. Rose, T. Tanaka, Rate of discharge of granular materials from bins and hoppers, Engineer. 208 (1956) 465.

[23] A. McLean, Empirical critical flow factor equations, Bulk Solids Handl. 6 (1986) 779–782.

[24] R.K. Eckhoff, P.G. Leversen, A further contribution to the evaluation of the Jenike method for design of mass flow hoppers, Powder Technol. 10 (1974) 51–58.

[25] V. Vidyapati, S. Subramaniam, Granular flow in silo discharge: Discrete element method simulations and model assessment, Ind. Eng. Chem. Res. 52 (2013) 13171–13182. doi:10.1021/ie303598e.

[26] R. de Borst, M.A. Crisfield, J.J.C. Remmers, C. V. Verhoosel, Non-linear finite element analysis of solids and structures, John Wiley Sons Ltd. 25 (2012) 1682–1690. doi:10.1007/s13398-014-0173-7.2.

[27] W.F. Chen, G.Y. Baladi, Soil Plasticity : Theory and Implementation, ELSEVIER, 1985. doi:10.1016/B978-0-444-42548-5.50002-7.

[28] R. Link, A. Elwi, Incipient flow in silo - hopper configurations, J. Eng. Mech. 116 (1990) 172–188.

[29] M.A. Diez, L.A. Godoy, Viscoplastic incompressible flow of frictional-cohesive solids, Int. J. Mech. Sci. 34 (1992) 395–408. doi:10.1016/0020-7403(92)90026-D.

[30] I. Keppler, Arching in Granular Materials, Szent Istvan University, Godollo, 2006.

[31] M. Wojcik, J. Tejchman, Numerical simulations of granular material flow in silos with and without insert, Arch. Civ. Eng. 53 (2007) 293–322.

[32] M. Wójcik, J. Tejchman, Modeling of shear localization during confined granular flow in silos within non-local hypoplasticity, Powder Technol. 192 (2009) 298–310. doi:10.1016/j.powtec.2009.01.021.

[33] A.J. Sadowski, J.M. Rotter, Study of buckling in steel silos under eccentric discharge flows of stored solids, J. Eng. Mech. 136 (2010) 769–776. doi:10.13140/RG.2.1.3069.5761.

[34] A.J. Sadowski, J.M. Rotter, Membrane theory treatment of eccentric flows in concentric hoppers, Thin-Walled Struct. 49 (2011) 902–912. doi:10.1016/j.tws.2011.02.016.

[35] A.J. Sadowski, J.M. Rotter, Buckling of very slender metal silos under eccentric discharge, Eng. Struct. 33 (2011) 1187–1194. doi:10.1016/j.engstruct.2010.12.040.

[36] Y.Z. Zhu, S.P. Meng, W.W. Sun, Lateral pressure in squat silos under eccentric discharge, Int. J. Civil, Environ. Structual, Constr. Archit. Eng. 6 (2012) 536–544. doi:10.4028/www.scientific.net/AMM.226-228.1420.

[37] Y. Wang, Y. Lu, J.Y. Ooi, Numerical modelling of dynamic pressure and flow in hopper discharge using the Arbitrary Lagrangian-Eulerian formulation, Eng. Struct. 56 (2013) 1308–1320. doi:10.1016/j.engstruct.2013.07.006.

[38] Q.J. Zheng, A.B. Yu, Finite element investigation of the flow and stress patterns in conical hopper during discharge, Chem. Eng. Sci. 129 (2015) 49–57. doi:10.1016/j.ces.2015.02.022.

[39] Q.J. Zheng, B.S. Xia, R.H. Pan, A.B. Yu, Prediction of mass discharge rate in conical hoppers using elastoplastic model, Powder Technol. 307 (2017) 63–72. doi:10.1016/j.powtec.2016.11.037.

[40] S. Kamath, V.M. Puri, Finite element model development and validation for incipient flow analysis of cohesive powders from hopper bins, Powder Technol. 102 (1999) 184–193.

[41] Y. Liu, M. Gonzalez, C. Wassgren, Modeling granular material segregation using a combined finite element method and advection–diffusion–segregation equation model, Powder Technol. 346 (2019) 38–48. doi:10.1016/j.powtec.2019.01.086.

[42] F. Ayuga, M. Guaita, P. Aguado, A. Couto, Discharge and the eccentricity of the hopper influence on the silo wall pressures, Eng. Mech. 127 (2001) 1067–1074.

[43] M. Guaita, A. Couto, F. Ayuga, Numerical simulation of wall pressure during discharge of granular material from cylindrical silos with eccentric hoppers, Biosyst. Eng. 85 (2003) 101–109. doi:10.1016/S1537-5110(03)00037-0.

[44] S. Ding, M. Wójcik, M. Jecmenica, S.R. de Silva, Loads on walls and inserts in mass-flow silos, 2003.

[45] M. Wojcik, G.G. Enstad, M. Jecmenica, Numerical calculations of wall pressures and stresses in steel cylindrical silos with concentric and eccentric hoppers, Part. Sci. Technol. 21 (2003) 247–258. doi:10.1080/02726350307486.

[46] J. Böhrnsen, H. Antes, M. Ostendorf, J. Schwedes, Silo discharge: Measurement and simulation of dynamic behavior in bulk solids, Chem. Eng. Technol. 27 (2004) 71–76. doi:10.1002/ceat.200401913.

[47] O. Saada, Finite element analysis for incipient flow of bulk solid in a diamondback hopper, J. Vis. Lang. Comput. 11 (2005) 287–301.

[48] J. Ooi, J. Rotter, S. Wang, Arching propensity in coal bunkers with non-symmetric geometries, 2005.

[49] Abaqus 6.14, Analysis User Manual, Dassault Syst. Simulia Corp. (2014).

[50] J.A.S. Cleaver, R.M. Nedderman, Measurement of velocity profiles in conical hoppers, Chem. Eng. Sci. 48 (1993) 3703–3712. doi:10.1016/0009-2509(93)81027-S.

[51] I. Sielamowicz, M. Czech, T.A. Kowalewski, Empirical analysis of eccentric flow registered by the DPIV technique inside a silo model, Powder Technol. 212 (2011) 38–56. doi:10.1016/j.powtec.2011.04.022.

[52] I. Sielamowicz, M. Czech, T.A. Kowalewski, Empirical description of flow parameters in eccentric flow inside a silo model, Powder Technol. 198 (2010) 381–394. doi:10.1016/j.powtec.2009.12.003.

[53] R. Maiti, G. Das, P.K. Das, Experiments on eccentric granular discharge from a quasi-two-dimensional silo, Powder Technol. 301 (2016) 1054–1066.

[54] R. Maiti, G. Das, P.K. Das, Granular drainage from a quasi-2D rectangular silo through two orifices symmetrically and asymmetrically placed at the bottom, Phys. Fluids. 29 (2017) 1–17. doi:10.1063/1.4996262.

[55] R.J. Berry, A.H. Birks, M.S.A. Bradley, Arching behaviour of cohesive powders in a pilot-scale plane-flow silo, Task Q. 7 (2003) 479–498. https://task.gda.pl/files/quart/TQ2003/04/TQ407A-E.PDF.

[56] J. Guo, A.W. Roberts, J.D. Prigge, Experimental investigation of wall pressure and arching behavior under surcharge pressure in mass-flow hoppers, Powder Technol. 258 (2014) 272–284. doi:10.1016/j.powtec.2014.03.048.

[57] U. Contreras, G. Li, C.D. Foster, A.A. Shabana, P. Jayakumar, M.D. Letherwood, Soil models and vehicle system dynamics, Appl. Mech. Rev. 65 (2013) 041001. doi:10.1115/1.4024759.

[58] E.A. de Souza Neto, D. Peri, D.R.J. Owen, Computational Methods for Plasticity, 2008. doi:10.1002/9780470694626.

[59] M.D. Bolton, The strength and dilatancy of sands, Géotechnique. 36 (1986) 65–78. doi:10.1680/geot.1986.36.1.65.

[60] D. Drucker, W. Prager, Soil mechanics and plastic analysis or limit design, Q. Appl. Math. 10 (1952) 157–164.

[61] L.H. Han, J.A. Elliott, A.C. Bentham, A. Mills, G.E. Amidon, B.C. Hancock, A modified Drucker-Prager Cap model for die compaction simulation of pharmaceutical powders, Int. J. Solids Struct. 45 (2008) 3088–3106. doi:10.1016/j.ijsolstr.2008.01.024.

[62] S. Swaminathan, J. Hilden, B. Ramey, C. Wassgren, Modeling the formation of debossed features on a pharmaceutical tablet, J. Pharm. Innov. 11 (2016) 214–230.

[63] D. Drucker, R. Gibson, D. Henkel, Soil mechanics and work hardening theories of plasticity, Trans. ASCE. 122 (1957) 338–346.

[64] I.C. Sinka, J.C. Cunningham, A. Zavaliangos, Analysis of tablet compaction II: Finite element analysis of density distributions in convex tablets, J. Pharm. Sci. 93 (2004) 2040–2053.

[65] J. Rice, Continuum Mechanics and Thermodynamics of Plasticity in Relation to Microscale Deformation Mechanisms, in: A. Argon (Ed.), Const. Equations Plast., MIT Press, Cambridge, Massachusetts, 1975.

[66] P.A. Vermeer, R. de Borst, Non-associated plasticity for soils, concrete and rock, HERON. 29 (1984) 1–64.

[67] G.W. Baxter, R.P. Behringer, T. Fagert, G.A. Johnson, Pattern formation in flowing sand, Phys. Rev. Lett. 62 (1989) 2825–2828. doi:10.1103/PhysRevLett.62.2825.

[68] H. Mühlhaus, Application of Cosserat theory in numerical solutions of limit load problems., Ing. Arch. 59 (1989) 124–137.

[69] J. Bobiński, J. Tejchman, Numerical simulations of localization of deformation in quasi-brittle materials within non-local softening plasticity, Comput. Concr. 4 (2004) 433–455.

[70] J. Tejchman, W. Wu, Numerical study on shear band patterning in a Cosserat continuum, Acta Mech. 99 (1993) 61–74.

[71] A.W. Jenike, Storage and flow of solids, Bull. Univ. Utah. 53 (1964). doi:10.2172/5240257.

[72] W.R. Ketterhagen, J.S. Curtis, C.R. Wassgren, B.C. Hancock, Predicting the flow mode from hoppers using the discrete element method, Powder Technol. 195 (2009) 1–10. doi:10.1016/j.powtec.2009.05.002.

[73] C 778 - 06 : Standard specification for standard sand, 2006. http://www.who.int/csr/don/03-june-2016-oropouche-peru/en/.

[74] C. Polito, R.A. Green, E. Dillon, C. Sohn, Effect of load shape on relationship between dissipated energy and residual excess pore pressure generation in cyclic triaxial tests, Can. Geotech. J. 50 (2013) 1118–1128. doi:10.1139/cgj-2012-0379.

[75] R.M. Lueptow, A. Akonur, T. Shinbrot, PIV for granular flows, Exp. Fluids. 28 (2000) 183–186. doi:10.1007/s003480050023.

[76] L. Sarno, A. Carravetta, Y.C. Tai, R. Martino, M.N. Papa, C.Y. Kuo, Measuring the velocity fields of granular flows – Employment of a multi-pass two-dimensional particle image velocimetry (2D-PIV) approach, Adv. Powder Technol. 29 (2018) 3107–3123. doi:10.1016/j.apt.2018.08.014.

[77] W. Thielicke, E.J. Stamhuis, PIVlab – Towards user-friendly, affordable and accurate digital particle image velocimetry in MATLAB, J. Open Res. Softw. 2 (2014). doi:10.5334/jors.bl.

[78] L. Sarno, M. Papa, Y. Tai, A. Carravetta, R. Martino, A reliable PIV approach for measuring velocity profiles of highly sheared granular flows, Latest Trends Eng. Mech. Struct. Eng. Geol. (2014) 134–141.

[79] L. Sarno, Y.-C. Tai, A. Carravetta, R. Martino, M. Nicolina Papa, C.-Y. Kuo, Challenges and improvements in applying a particle image velocimetry (PIV) approach to granular flows, J. Phys. Conf. Ser. 1249 (2019) 012011. doi:10.1088/1742-6596/1249/1/012011.

[80] J.E. Bowles, Foundation Analysis and Design, Fifth edit, 1997. doi:10.1016/0013-7952(84)90010-3.

[81] R. Maiti, S. Meena, P.K. Das, Flow field during eccentric discharge from quasi-two-dimensional silos – extension of the kinematic model with validation, AIChE J. 62 (2016) 1439–1453. doi:10.1002/aic.

[82] A. Simoni, G.T. Houlsby, The direct shear strength and dilatancy of sand-gravel mixtures, Geotech. Geol. Eng. 24 (2006) 523–549. doi:10.1007/s10706-004-5832-6.

[83] Z. Szypcio, Stress-dilatancy for soils. Part III: Experimental validation for the biaxial condition, Stud. Geotech. Mech. 39 (2017) 73–80. doi:10.1515/sgem-2017-0007.

[84] T.B. Edil, C.H. Benson, C.A. Bareither, Determination of shear strength values for granular backfill material, Wisconsin Highw. Res. Progr. 92 (2008) 150.

[85] P. Guo, X. Su, Shear strength, interparticle locking, and dilatancy of granular materials, Can. Geotech. J. 44 (2007) 579–591. doi:10.1139/T07-010.

[86] I. Anastasopoulos, G. Gazetas, M.F. Bransby, M.C.R. Davies, A. El Nahas, Fault rupture propagation through sand: Finite-element analysis and validation through centrifuge experiments, J. Geotech. Geoenvironmental Eng. ASCE. 133 (2007) 943–958. doi:10.1061/(ASCE)1090-0241(2007)133:8(943).

[87] L.Y. Leung, C. Mao, I. Srivastava, P. Du, C.Y. Yang, Flow function of pharmaceutical powders is predominantly governed by cohesion, not by friction coefficients, J. Pharm. Sci. 106 (2017) 1865–1873. doi:10.1016/j.xphs.2017.04.012.

[88] E. Benink, Flow and stress analysis in cohesionless bulk materials in silos, Enschede, The Netherlands, 1989.

[89] Z. Mroz, C. Szymanski, Gravity flow of granular material in converging channel, Arch. Mech. 23 (1971) 897–917.

[90] D.L. Henann, K. Kamrin, A finite element implementation of the nonlocal granular rheology, Int. J. Numer. Methods Eng. (2012) 273–302. doi:10.1002/nme.

[91] D. Negussey, W.K.D. Wijewckreme, Y.P. Vaid, Constant-volume friction angle of granular materials, Can. Geotech. J. 25 (1988) 50–55.

[92] V. Mazel, V. Busignies, H. Diarra, P. Tchoreloff, Measurements of elastic moduli of pharmaceutical compacts: A new methodology using double compaction on a compaction simulator, J. Pharm. Sci. 101 (2012) 2220–2228. doi:10.1002/jps.23122.

[93] R.K. Eckhoff, G.G. Enstad, P.G. Leversen, A further contribution to the design of mass flow hoppers for powder silos, in: Int. Scand. Congr. Chem. Eng., Copenhagen, 1974: pp. 28–30.

[94] D. Schulze, A. Wittmaier, Flow properties of highly dispersed powders at very small consolidation stresses, Chem. Eng. Technol. 26 (2003) 133–137.

[95] K. Johanson, Effect of particle shape on unconfined yield strength, Powder Technol. 194 (2009) 246–251. doi:10.1016/j.powtec.2009.05.004.

[96] T. Swize, F. Osei-yeboah, M.L. Peterson, P. Boulas, Impact of shear history on powder flow characterization using a ring shear tester, J. Pharm. Sci. 108 (2019) 750–754. doi:10.1016/j.xphs.2018.07.003.

VITA

Kunal Sanjay Pardikar graduated from Indian Institute of Technology, Bombay (IITB) in 2015. He earned his dual degree (Bachelor's + Master's) in Energy Science and Engineering. He started the PhD program at school of Mechanical Engineering, Purdue University in Spring 2016. He worked in the center of particulate products and processes (cp3) group under the guidance of Prof. Carl Wassgren. His dissertation is focused on Finite Element Method (FEM) modeling of hopper flow. He received financial support from the Idaho National Laboratory (Idaho Falls, ID), Genentech, Inc. (San Francisco, CA) and school of Mechanical Engineering during his PhD. He did two summer internships at the Idaho National Laboratory during his PhD, where he worked on FEM modeling of biomass material.

PUBLICATIONS

K. Pardikar, C. Wassgren, Predicting the critical outlet width of a hopper using a continuum finite element method model, Powder Technol. 356 (2019) 649–660. doi:10.1016/j.powtec.2019.08.111.

K. Pardikar, S. Zahid, and C. Wassgren, Quantitative comparison of experimental and Mohr-Coulomb finite element method simulation flow characteristics from quasi two-dimensional flat-bottomed bins, Powder Technology. 367 (2020) 689-702. doi:10.1016/j.powtec.2020.04.036.